NORTHWESTERN UNIVERSITY

Polymeric Material Self Assembly for Biological Applications

A DISSERTATION

SUBMITTED TO THE GRADUATE SCHOOL
IN PARTIAL FULFILLMENT OF THE REQUIREMENTS

for the degree

DOCTOR OF PHILOSOPHY

Field of Chemical and Biological Engineering

By

Yang Li

EVANSTON, ILLINOIS

September 2024

ABSTRACT

Polymeric materials are well-recognized for their ability to self-assemble into various superstructures. By meticulously adjusting the conditions of the self-assembly process—such as polymer characteristics, solvent properties, and environmental factors including temperature and pressure—superstructures with distinct morphologies and properties can be synthesized. These distinctive properties of polymeric materials have been extensively leveraged across numerous fields. In recent decades, polymeric materials have seen significant application in biology and biomedicine. A prominent example is the implementation of lipid nanoparticle (LNP) drug delivery systems in the SARS-CoV-2 mRNA vaccines. Lipid molecules self-assemble into nanoparticles, encapsulating mRNA and thereby playing a critical role in protecting it from degradation within biological environments and enhancing cellular uptake. Additional notable applications of polymer self-assembly include plastic bioelectronics, biological scaffolds, and bioadhesives. This dissertation elaborates on two major projects with a focus on self-assembled polymeric materials designed for biological applications. Chapter 2 introduces a novel peptide amphiphile system tailored for biomacromolecule purification. The mechanisms driving the co-assembly of peptide amphiphiles are discussed. Chapter 3 presents the emerging polymer Poly(propylene sulfone), an amphiphilic homopolymer capable of capturing biomacromolecules without compromising their structural integrity or function. The binding mechanism of Poly(propylene sulfone), along with its potential applications, is thoroughly examined. Collectively, these studies contribute to the broader understanding of polymer self-assembly and its potential to advance the fields of biology and biomedicine.

ACKNOWLEDGEMENTS

I wish to express my deepest gratitude to those who have been a steadfast support throughout my PhD journey. First and foremost, I extend my heartfelt thanks to my advisor, Dr. Monica Olvera de la Cruz. She embodies the essence of a true scientist, relentlessly pursuing truth with unwavering dedication. Dr. Olvera de la Cruz conveyed not only knowledge and wisdom but also a keen insight into the unknown and an enduring enthusiasm for challenges. I am also profoundly grateful to my co-advisor, Dr. Evan A. Scott, who exemplifies a model of relentless pursuit towards his goals. He has shown how imagination can weave discrete pieces of knowledge into a coherent whole, and how this integrity can be used to explore infinite possibilities. Special thanks are due to Dr. Baofu Qiao, who opened the door to my scientific career. His mentorship extended beyond teaching specific techniques or knowledge in certain fields; he also helped shape my perspective on my PhD journey. These remarkable scientists have been an inspiration throughout my PhD career and will undoubtedly continue to inspire me for the rest of my life.

I would also like to express my sincere appreciation to all my colleagues in Monica's and Evan's groups. I want to thank my previous and current office mates Yange Lin, Brandon Onusaitis, and Dingwen Qian. I benefited a lot from the scientific and non-scientific discussions with them. I am thankful to Dr. Turash Haque Pial and Dr. Yao Xiong for the incredible work we accomplished together. My gratitude extends to Dr. Felipe Jimenez-Angeles, Dr. Jianshe Xia, Dr. Ali Ehlen, Dr. Chase Brisbois, Dr. Hang Yuan, Dr. Leticia Lopez-Flores, Dr. Chuting Deng, and Dr. Joseph McCourt, who have all contributed significant professional insights. I am especially grateful to Dr. Fanfan Du for our extensive discussions across various scientific areas and to Dr. Clayton Rische for our fruitful collaboration with Dr. Du. I also want to acknowledge Antara,

Sulton, Natalie, El Hadji, and Sofie for the uplifting small talks.

Beyond Northwestern, I am deeply thankful to my collaborators from various institutions. I am particularly grateful to Dr. Honggang Cui from Johns Hopkins University for initiating a challenging, intriguing, and impactful project, engaging in extensive scientific discussions, and providing invaluable career advice. I would also like to thank Myriel Kim from Johns Hopkins University and Carlos Jimenez from the University of Chicago for their collaboration and the cups of coffee we had. My sincere thanks also go to Dr. Matthew Tirrell from the University of Chicago and Dr. Xuankuo Xu from BMS for their insights during our collaboration.

Outside of academia, I am indebted to my family and friends. My parents have always been my strongest supporters, never doubting my choices and always encouraging me to pursue my dreams. I am also grateful to my grandparents for their love and support. My heartfelt thanks go to Murphy, Nomie, and Milky for their cuddles and unconditional trust. I also wish to thank Irene Zhang for being a heat generator and radiating energies to other. I want to thank Dr. Zihan Qu for overwhelming me with knowledge from a field that I know nothing about and also those loss streak we have in Dota 2. Dr. Guanhua Wang has been a great companion in sharing funny news and career anxieties. I also really appreciate Zach, XiaoLu, and Nannan for sharing their youth energy. I am also grateful to Tianyang Zhang, Xuan Mei, Jia Fu, Qiaoyu Jin, and Guo Chen for the weird memes and light-hearted moments we've shared. Lastly, I extend my thanks to Christy Liu for the fun and laughter we have had.

I am deeply grateful for the unwavering support I have received. Without the encouragement and positive influence from each of you, my achievements would not have been possible.

TABLE OF CONTENTS

LIST OF FIGURES

LIST OF TABLES

CHAPTER 1
INTRODUCTION AND BACKGROUND

The SARS-CoV-2 pandemic devastated the global population, infecting 776 million individuals and resulting in over 7 million fatalities. The crisis of 2020 further exacerbated global inequities, pushing more than 34 million people into extreme poverty. Even five years later, the world continues to endure its repercussions. A critical advancement during this global crisis was the introduction of mRNA vaccines for SARS-CoV-2. These vaccines were instrumental in reducing transmission rates and lowering the fatality rate of the disease. In recognition of their pioneering work, Dr. Katalin Kariko and Dr. Drew Weissman, developers of mRNA technology, were awarded the Nobel Prize in 2023. However, mRNA technology is not a recent innovation. In the 1980s, Dr. Katalin Kariko discovered that cells could be induced to produce specific proteins through the introduction of certain types of mRNA. In 2005, Dr. Kariko and Dr. Drew Weissman published a seminal work in Immunity, where they detailed how mRNA could be modified to induce protein production without eliciting severe immune responses[1]. In their conclusion, they highlighted the therapeutic potential of mRNA. Nevertheless, the inherent susceptibility of mRNA to degradation within the human body and its excessive negative charge, which limits cellular penetration, posed significant challenges.

A crucial advancement that facilitated the practical application of mRNA vaccines was the development of liposome nanoparticle delivery systems (**Fig. 1.1**). Liposomes, typically composed of lipid molecules, possess amphiphilic structures with hydrophilic heads and hydrophobic tails. In aqueous environments, these lipids self-assemble into bilayer nanoparticles, which can encapsulate therapeutic agents. Liposomes not only protect the mRNA from the biological milieu but also

enhance its ability to penetrate cells. Without this materials innovation, the mRNA vaccines would likely not have succeeded, as existing and widely utilized polymeric formulations and delivery strategies are not compatible with mRNA[2,3].

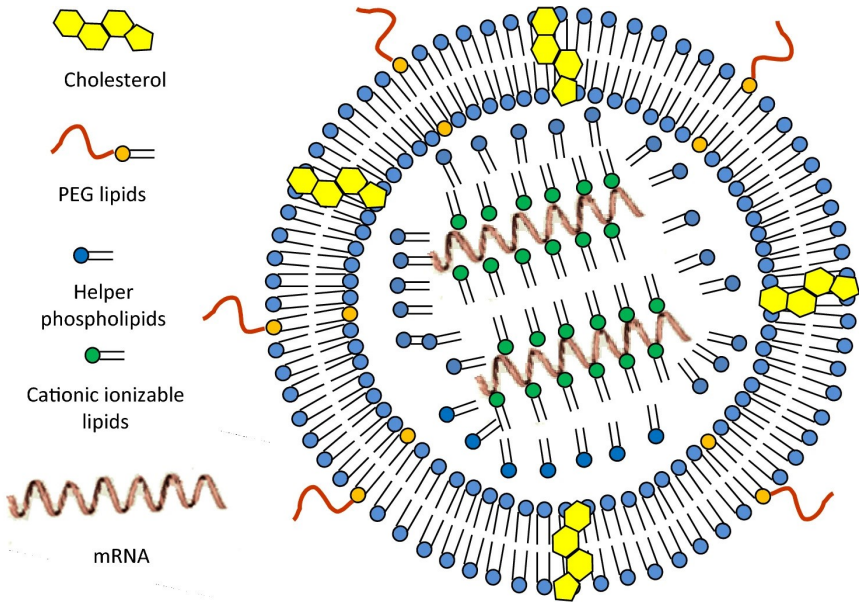

Figure 1.1: Schematic representation of components of lipid nanoparticles (LNPs) with mRNA.[3]

Beyond drug delivery and vaccines, polymeric materials have been extensively explored for a wide range of biological applications. By precisely tuning the properties of polymers, such as their degree of polymerization and hydrophobicity, various morphologies can be engineered to fulfill specific functions. For instance, in tissue engineering (**Fig. 1.2a**), different polymer networks can be designed to meet distinct needs: mechanically robust polymer networks provide structural support, while loose and porous scaffolds are ideal for regenerative purposes[4]. Moreover, conductive and biocompatible polymers can be developed into bioelectronics(**Fig. 1.2b**), bridging the interface between biology and electronics. These plastic bioelectronics can be either wearable, such as artificial skins, or implantable devices directly attached to organs. Equipped with integrated sensors, these devices enable real-time monitoring of biological activities, even at the level of single

neurons[5,6,7](**Fig. 1.2c**).

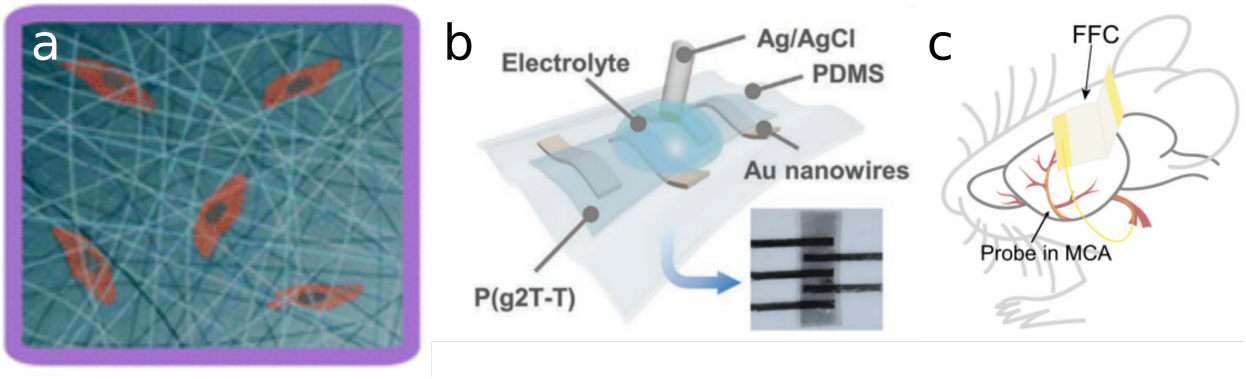

Figure 1.2: (a) Tissue Engineering; (b-c) Bioelectronics.

In this dissertation, I will discuss the major projects I have undertaken during my PhD program, focusing on the utilization of polymeric material self-assembly in conjunction with biological macromolecules. Chapter 2 introduces a novel peptide amphiphile system tailored for biomacromolecule purification. Peptide amphiphiles with human antibody binding groups self assembled into immunofibers and further form crosslinked networks upon capturing the antibodies. In Chapter 2, the mechanisms driving the co-assembly of peptide amphiphiles are discussed. Chapter 3 presents the novel polymer Poly(propylene sulfone), an amphiphilic homopolymer capable of capturing biomacromolecules without compromising their structural integrity or function. In Chapter 3, two strategies to conjugate proteins with Poly(propylene sulfone) are presented to accomplish the goals of multi-component drug delivery and biomolecule protection in foreign environments. Along the application, the binding mechanisms are extensively discussed. In addition to the completed work, this dissertation outlines future perspectives on how the two projects can be further developed. It is my hope that this dissertation will provide valuable insights and guidance for future research endeavors.

CHAPTER 2

HIGH-AFFINITY SUPRAMOLECULAR PEPTIDE MATERIALS FOR SELECTIVE CAPTURE AND RECOVERY OF PROTEINS

Therapeutic biomolecules have arisen attentions due to their biocompatibility, efficacy, and low side effects. The separation and purification of the therapeutic molecules pose challenges in the industrial production streamline. Human immunoglobulin G (IgG) is the most comman human antibodies ($\sim$75% of the serum antibodies) and can be engineered to target various receptors. Despite the high efficiency in upstream production, the bottom stream purification bottlenecks overall efficiency and yield. The prevailing purification method is the Protein A column chromatography (**Fig. 2.1**[*]). The columns are filled with a resin decorated with Protein A, a kind of bacteria-originated proteins that exhibits high affinity to IgGs. The upstream products containing IgGs and impurities are fed into the columns, and the IgGs are selectively binding to the Protein A. Subsequently, the IgGs can be separated from the columns by adjusting the pH. Desipte the its robustness, the Protein A chromatography suffers from limited capacities and high costs[8,9]. A more efficient, economic bottom stream purification process is required for further scale-up of the monoclone antibody industry.

Li et al, showed the supermolecular assembly of peptide amphiphiles with Z33 is a promising candidate for mAb capture, separation and recovery (**Fig. 2.2**). Z33 is a 33 amino acids minimized binding segments derived from the Protein A and binds with mAb with a molar ratio of 2:1. The

[*]Image adapted from `https://www.proteogenix.science/protein-purification/tag-purification/`

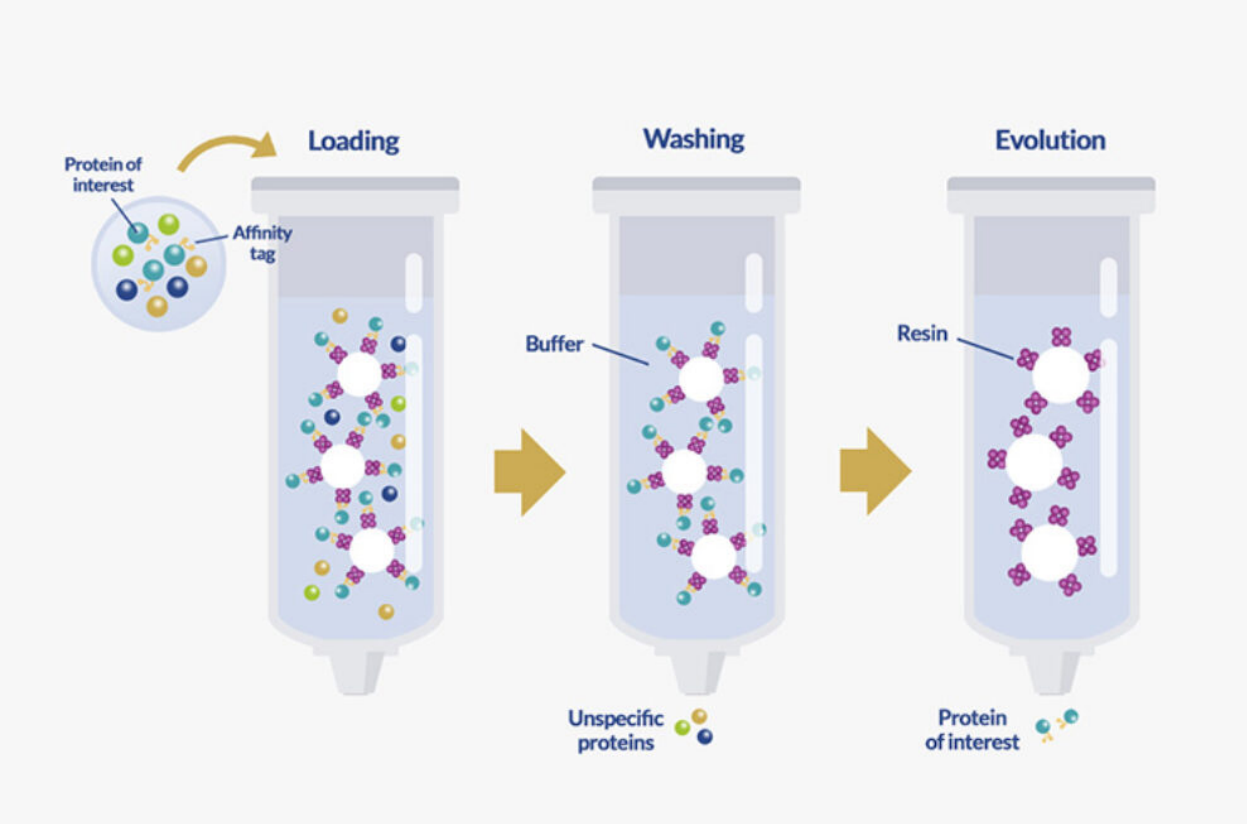

Figure 2.1: The scheme of human antibody purification with Protein A Chromatography.

binding between Z33 and mAb is pH sensitive. Z33-decorated PAs (ligands) self assembles with filler PAs into immunofibers, selectively binds with mAbs, and form cross-linked networks that separate from solutions. Subsequently, mAbs can be recovered by adjusting the pH. The scheme is shown below.

A clear understanding of the mechanism behind the assemble-binding-phase separation is significant to maximize the purification efficiency. In this chapter, the hierarchical assembly process will be discussed. First, the self-assembly of only fillers is discussed to unveil the importance of electrostatics. Subsequently, the co-assembly of fillers and ligands is investigated to introduce the

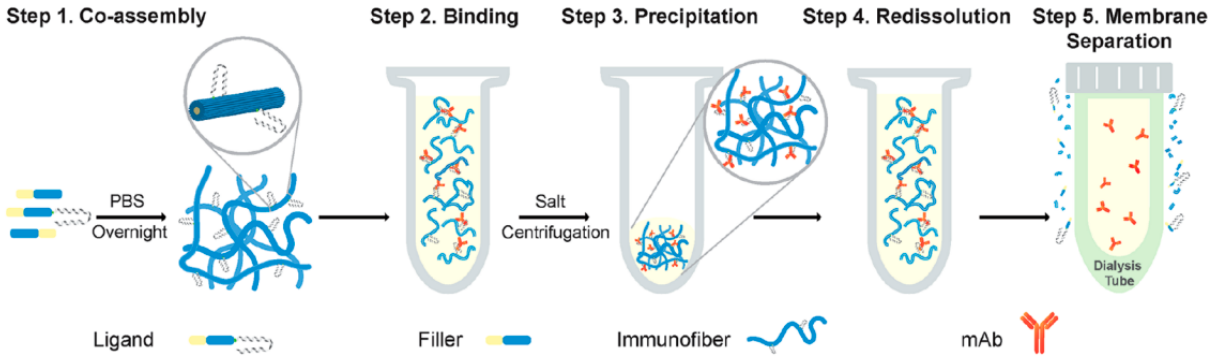

Figure 2.2: The scheme of human antibody purification with immunofibers.

local segregation of Z33 over the fiber surfaces.In the last part, I will briefly touch on multi-fiber interactions and IgG-fiber crosslinking process.

2.1 Aggregation-Induced Asymmetric Charge States of Amino Acids in Supramolecular Nanofibers

Authors: Yang Li, Myrial Kim, Turash Haque Pial, Yange Lin, Honggang Cui, and Monica Olvera de la Cruz.
This is work is adapted from *J. Phys. Chem. B 2023, 127, 38, 8176–8184,* `https://doi.org/10.1021/acs.jpcb.3c05598`. Y. Li conceived this study and performed the simulations and wrote the manuscript. M. K. carried out experiments and characterizations and wrote the manuscript. T. H. P. performed the simulation. Y. Lin fitted the titration and wrote the manuscript. H. C. supervised the experiments and wrote the manuscript. M. Olvera de la Cruz supervised all the research and wrote the manuscript.

2.1.1 Introduction

Self assembly is a ubiquitous phenomenon in amphiphile systems. In hydrophilic environments, the hydrophobic composition aggregates together to minimize the interfacial energies and vice versa. In this projects, two charged PA molecules are utilized to form high-aspect ratio nanofibers. The chemical formalus are shown below. The hydrocarbon tail renders hydrophobicity. The Valine is hydrophobic and forms directional hydrogen bonds with other Valine groups. The Lysin and Glutamic acid are hydrophilic and charged. The Z33 is the mAb binding group. At a concentration above the critical micelle concentration (CMC), PAs first self assemble into micelles and further aggregate into nanofibers.

Given their weak acid/base nature, charge regulation of amino acids varies due to numerous factors, such as pH, molecule concentration, and microenvironment. Research unveils that the charge states of amino acids shift by an unexpected amount under different conditions[10,11,12]. Isom et al. showed that, in a single protein, depending on the microenvironment, glutamic acid (GLU) has a $\mathrm{pK_a}$ ranging from 4.5-9.5 with a theoretical value of 4.5[10]. Similarly, the self-assembly process of PA brings about changes in the chemical environment of the assembled molecules. The $\mathrm{pK_a}$ shift of amino acids in peptide amphiphiles upon self-assembly has been long noticed in experi-

ments[11,12].

Theorists have made efforts to predict the acid-base equilibrium between the protonated and deprotonated acids in PA self-assembly under different pH and salt conditions[13,14,15]. However, the phenomenon draw few attention in simulation works[16,17]. All amino acids are usually assumed to be charged if they have an acidic/basic side chain. The first reason is the computation expense in molecular dynamics (MD) simulations. Even though many successful attempts have been made using the continuum model[18,19], simulating pH effects in the atomistic scale is still challenging and expensive. Furthermore, the time scale to which atomistic simulations can reach is limited. It is difficult to capture structural transitions in complex PA systems. Therefore, in these cases, regardless of the strong approximations, fully charged PA models often yield qualitative accurate results[14]. Another major reason lies in the deceiving fact that amino acids are calculated to be charged by using experimental pH and the theoretical $\mathrm{pK_a}$s of the amino acids. However, the $\mathrm{pK_a}$ of an amino acid is a function of its surroundings[20] and can vary significantly. Shifts in the $\mathrm{pK_a}$ of amino acids are often underestimated.

In this paper, we demonstrate that microenvironments have decisive effects on the charge states of amino acids, and the resulting quantitative difference in the charge would lead to a qualitative change in the nanostructure of PA assembly. The charge states of the fiber should be discretely described to accurately depict the properties of the fiber. As shown here, overestimating electrostatics in the PA superstructures yields significant deviations in various physical properties, including their structural density, charge density, and the degree of salt ion condensation. Furthermore, on the macroscale, PA fiber interactions that depend on the surface charges would be modified.

Motivated by the immunology studies on short carbon PAs, we first focus on a specific system of nanofiber self-assembled by hydrophobic-hydrophilic-patterned peptide amphiphiles with a short hydrophobic segment. This system is especially amenable to determining the competition between

hydrophobic and electrostatic interactions in PAs self-assembly into either spherical micelles or cylindrical fibers. In contrast, in systems with large carbon chains, the hydrophobic interactions usually dominate and fibers are formed regardless of the charge states of the amino acids in MD simulations where the amino acids are generally assumed to be fully charged. The chemical structure of the molecule in this study is shown in **Fig. 2.3**. In the system, 2 kinds of acid-base equilibrium exist.

$$\mathrm{C_{12}-VVE_1^0E_2 \rightleftharpoons C_{12}-VVE_1^{-1}E_2 + H^+} \tag{2.1}$$

$$\mathrm{C_{12}-VVE_1E_2^0 \rightleftharpoons C_{12}-VVE_1E_2^{-1} + H^+} \tag{2.2}$$

The superscript denotes the charge states of the Glutamic acid (referred to as GLU or E), where 0 means the protonated state where the residue is not charged and -1 means the deprotonated state where the residue carries a negative charge. The subscript denotes the location of the GLU in the sequence. Experimentally, the PAs form nanofibers under pH = 7.3 $\sim$ 7.4[21]. Usually, both GLUs are assumed to carry a negative charge under the experimental pH condition due to the very low $\mathrm{pK_a}$ of GLU in bulk solutions. However, we hypothesize that the self-assembly process would create different microenvironments for GLUs: the inner GLU ($\mathrm{E_1}$) will locate around the boundary between the hydrophobic cores and the solvent. With limited access to polar solvents and ions, the protonation states are expected to be different from those of the bulk condition. Furthermore, in the case of short peptide amphiphile systems, the repulsive interactions between charged amino acids become significant. Therefore, a discrepancy between the fully charged PA assumption in simulations and the experimental results is expected. Here, $\mathrm{C_{16}}$-VVEE fibers systems are also studied

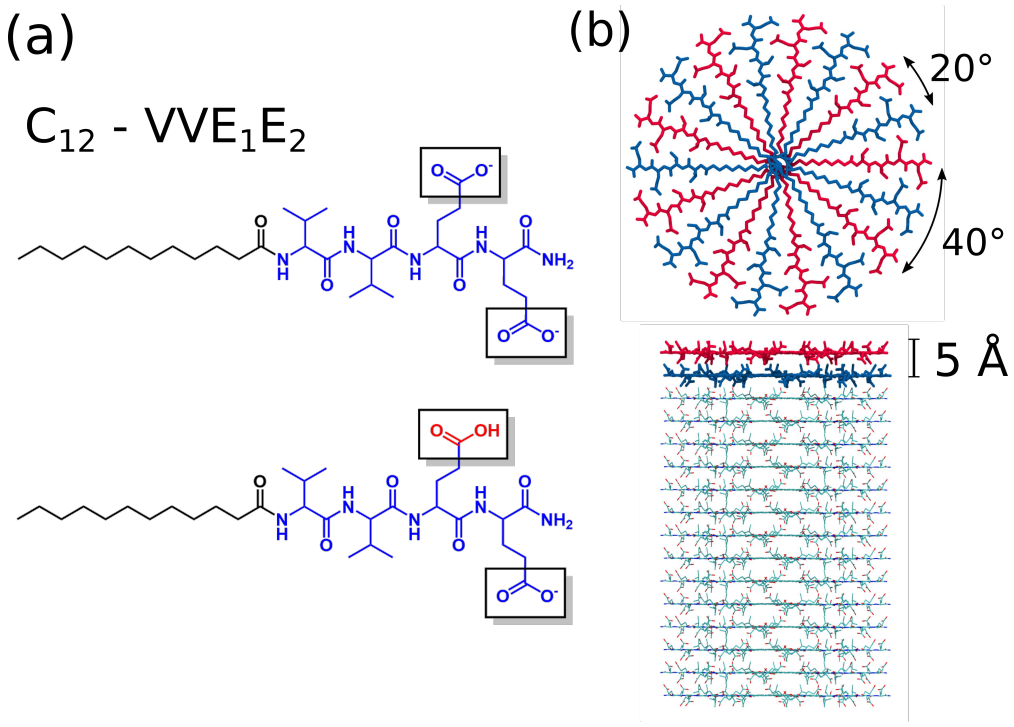

Figure 2.3: Chemical structures of the studied peptide amphiphiles and schematic illustration of the initial setup for atomistic simulations. (a) Peptide amphiphile molecule for the fiber simulation. The first molecule is fully deprotonated and carries $-2e$ charges. The second molecule is half protonated and carries $-1e$ charges. (b) Initial structure of the fiber.

to demonstrate that MD simulations give qualitatively similar results regarding fiber formation regardless of the assumptions in the charge states of the amino acids when hydrophobic interactions dominate yet structural properties such as amino acid packing and ionic cloud distributions in the fibers are affected.

2.1.2 Discussion

Based on both previous experiments and theoretical results, the $\mathrm{pK_a}$ values of GLUs vary depending on the local environments[10,11]. Under a certain range of pH, it is possible that due to the

difference in the microenvironment, E_1 is protonated and carries no charges, while E_2 is deprotonated and has a $-1e$ charge in the C_{12}-VV$\mathrm{E}_1\mathrm{E}_2$ molecule. We expect that, in these cases, distinct structures would form, and MD simulations can capture the transitions between structures since the hydrophobic interactions do not dominate over the Coulombic repulsions.

Two parallel simulations are performed with the same conditions except for the protonation states of the PA molecules. The atomistic simulation of the half-protonated PA system yields a stable, compactly packed fiber structure (**Fig. 2.4a**), which aligns with experimentally observed structures in literature. The convergence of energy and box size in the z direction indicates the equilibrium is reached (**Fig. A.2**). Around 9.8% of peptide heads form β-sheets, which help stabilize the structure. The C_{12} heads form a hydrophobic domain, where no water molecules or ions penetrate. In comparison, the fiber composed of fully charged PA molecules breaks down into spherical micelles (hereafter termed micelles) (**Fig. 2.4b**). Two micelles have 63 PA molecules and 81 PA molecules, respectively.

The change in the equilibrium structure can be attributed to the different protonation states of E_1 and E_2. E_1 is assumed to be protonated due to (1) decreased relative permittivity and (2) limited access to ions. The radial distribution functions (RDF) of E_1 and E_2 are shown in **Fig. 2.4c**. At the ion concentration applied in this study (0.1 M), the Debye length agrees well with experimental measurements and is used to estimate the interactions between charges[22]. We assume the relative permittivity of the hydrophobic domain is $\varepsilon_r = 2$ (oil) and the local Debye length $\varepsilon_r(r)$ is a linear combination of the volume fraction of fiber ($\varepsilon_r = 2$) and water ($\varepsilon_r = 80$). With Eq. (2.9), Debye length $\lambda_D(r)$ is calculated (**Fig. 2.4c**). The local Debye length is 26.7% larger at the position of E_1 ($\lambda_1 = 0.76\mathrm{nm}$) than that at the position of E_2 ($\lambda_2 = 0.60\mathrm{nm}$). The screening effect is much weaker in the environment of E_1. Further, if the acid-base equilibrium shifts and one GLU loses a

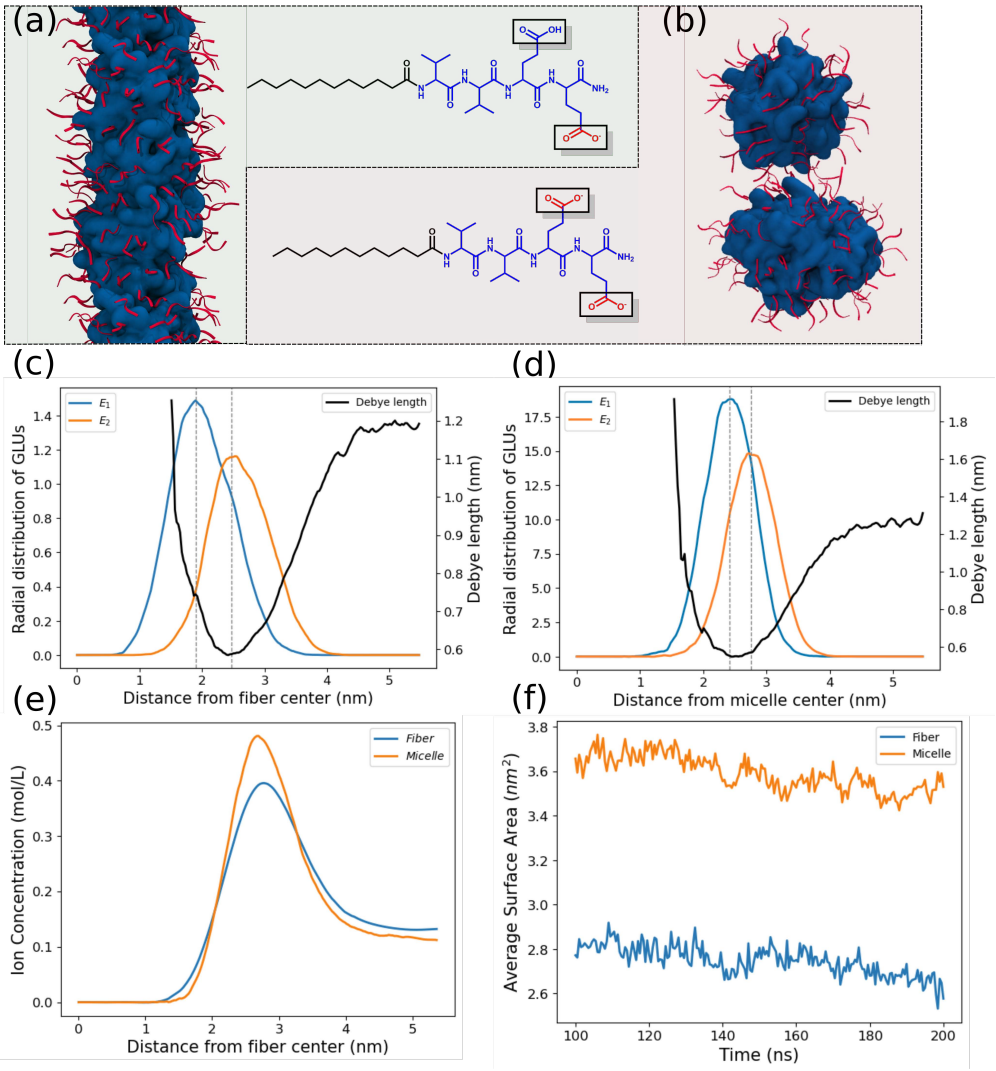

Figure 2.4: Atomistic simulation results of the peptide amphiphiles. (a) The equilibrium snapshot of the $C_{12} - VVE_1^0E_2^{-1}$ fiber. A densely packed fiber is formed. (b) The equilibrium snapshot of the $C_{12} - VVE_1^{-1}E_2^{-1}$ system. The fiber breaks down into 2 micelles. Blue surfaces are the C_{12} hydrophobic cores, and the red cartoons are the amino acids. The GLUs RDFs and the Debye length as a function of distance from the C_{12} center of (c) the fiber and (d) the micelles. Both E_2 have lower and wider peaks relative to E_1 because, farther away from the center, the GLUs have more free space. The Debye length near the hydrophobic cores is huge due to the sparse distribution of ions. It drops drastically as the distance from the center increases and reaches the minimum around the margin of the fiber/micelle due to the ion condensations. (e) The Ion condensation around the fiber and the micelle. The micelle has more ion condensed around it. (f) The average solvent-accessible surface area per PA molecule. The micelle has a much larger average surface area, allowing more ions and solvent molecules to diffuse into the micelle.

proton, the change in Coulombic interaction energy can be calculated with

$$\mathrm{d}E_{Coul}(r) = \sum_i \frac{|q_i|\,|q|}{4\pi\varepsilon_0 r_i^2} \times e^{-r_i k(r)} \propto e^{-r_i \lambda_D(r)^{-1}} \tag{2.3}$$

where $k(r)$ is the inverse of Debye length, r_i is the distance between the new charge and every other charge. Therefore, the energy penalty is exponentially higher if the charge is buried deeper inside the fiber. The synergistic effect of the low permittivity and low ion concentration suggests that E_1 is protonated.

A similar analysis is performed on the micelles, where both GLUs are charged in the PA molecules. The RDF of E_1, E_2, and Debye length are shown in **Fig. 2.4d**. The local Debye length at E_1 ($\lambda_3 = 0.55\mathrm{nm}$) and at E_2 ($\lambda_4 = 0.56\mathrm{nm}$) of micelles has very close values and is less than the Debye length near the cylindrical fiber (35.7% less than λ_1 and 8.9% less than λ_2). Both GLUs in the micelle experienced significantly stronger electrostatic screening. Compared with cylindrical fibers, micelles have larger unit surface areas ($\sim$31%) (**Fig. 2.4f**). Sparse distribution of the GLUs mitigates Coulombic repulsion. Furthermore, the micelles occupy less volume fraction at the same distance r from the center, compared with fibers. More free space allows more solvent molecules and ions to diffuse into the micelles, increasing the level of ion condensation around the micelle hydrophobic cores (**Fig. 2.4e**).

To further prove the statement that limited access to water and ions prevents deprotonation of the carboxylic groups, an artificial structure of the fiber with $-2e$ charges in each PA molecule is simulated by fixing the terminal atom of C_{12} with a position restraining force. The results are listed in **Fig. 2.5**. The RDF of the E_1 group has a shift away from the fiber center, as well as a narrower peak. The RDF suggests more extended PA chains in the artificial structure. A less compact structure is generated. Meanwhile, the distribution of Na^+ shifts toward the center of

the fiber, indicating that Na^+ penetrates deeper into the fiber. The narrowing gap between two distribution function peaks indicates E_1 has more access to ions and therefore screens out the electrostatic repulsions and gains electrostatic attraction energies via binding due to the smaller local permittivity. However, internally, the fiber is dehydrated, increasing the local electrostatic potential. It is entropically unfavorable for free Na^+ to move from a polar medium to a less polar medium and to bind with the fiber. Therefore, the synergy of these effects generates potential destructive effects on the cylindrical fiber structure.

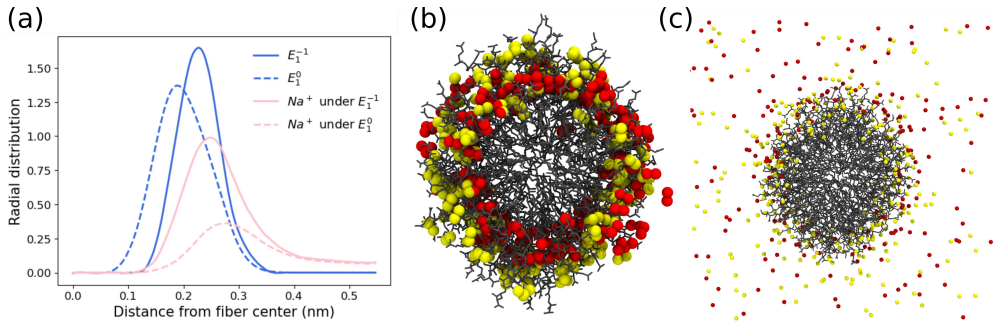

Figure 2.5: Simulation results of artificial supramolecular nanofiber structure. (a) RDF of E_1 and Na^+. E_1 has more access to Na^+ after deprotonation. The distribution of (b) E_1 and (c) Na^+. Red stands for the results of single-charged PA (E_1 is uncharged), while yellow stands for the results of double-charged PA (E_1 is charged).

MARTINI 3 coarse-grained simulations produced the expected results (**Fig. 2.6**). With fully deprotonated C_{12}-VVEE PA molecules, only micelles are formed. Two micelles have 64 and 86 PA molecules, respectively, qualitatively consistent with atomistic simulations. On the contrary, half-protonated C_{12}-VVEE PA molecules form micelles and quickly merge into cylindrical fibers.

To obtain the experimental $\mathrm{pK_a}$ values of the GLUs in the PA molecules, titration on C_{12}-VVEE is carried out. We also write the pH of the solution as an analytical function of the added volume

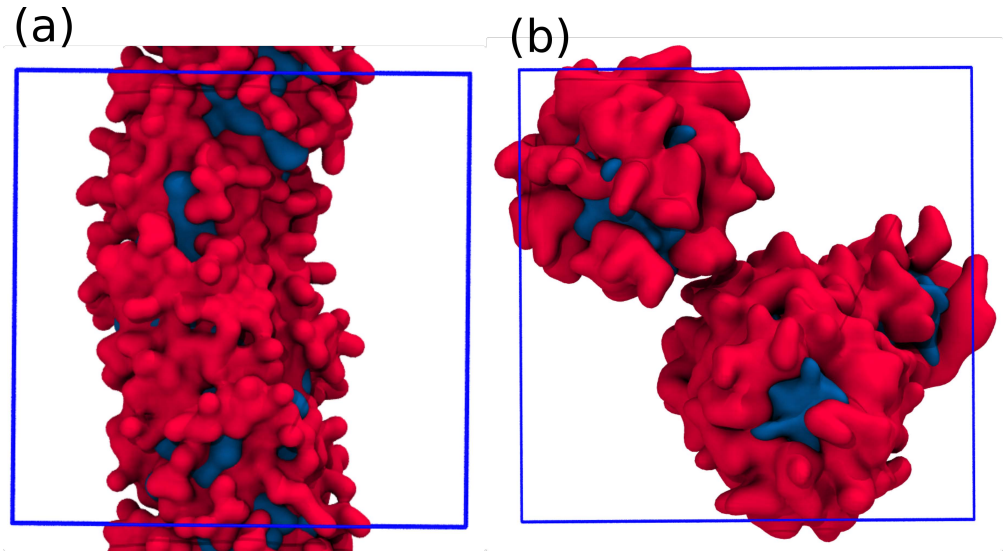

Figure 2.6: MARTINI3 coarse-grained simulations. (a) The equilibrium snapshot of the $C_{12} - VVE_1^0E_2$ fiber. A densely packed fiber is formed. (b) The equilibrium snapshot of the $C_{12} - VVE_1^{-1}E_2$ system. Two micelles form, consistent with the atomistic simulation results.

of NaOH based on the acid-base equilibrium, with 2 distinct $\mathrm{pK_a}$s as fitting parameters (details are included in the Appendix A). The titration curve and fitting curve are given in **Fig. 2.7a**, and the $\mathrm{pK_a}$ values are given in Table 1. A large shift in $\mathrm{pK_a}$s is observed. Under the fiber self-assembly experiments (pH = 7.3∼7.4), the protonation states are calculated with Henderson-Hasselbalch equation[20]

	theoretic $\mathrm{p}K_a$	experimental $\mathrm{p}K_a$	$\Delta\mathrm{p}K_a$	charged (%)
E_1	4.1	9.3	5.2	4
E_2		6.0	1.9	99

Table 2.1: $\mathrm{p}K_a$ of GLUs from Titrations

$$\alpha = \frac{1}{1 + 10^{\mathrm{pH} - \mathrm{p}K_a}} \tag{2.4}$$

where α is the percentage of the acidic form (charge-neutral) of the GLU residue under a cer-

tain pH. Only 4% of the inner GLUs (E_1) are charged while almost all the outer GLUs (E_2) are negatively charged. The results are consistent with our hypothesis and simulation results.

It became necessary to validate experimentally if there is indeed a morphological transition in

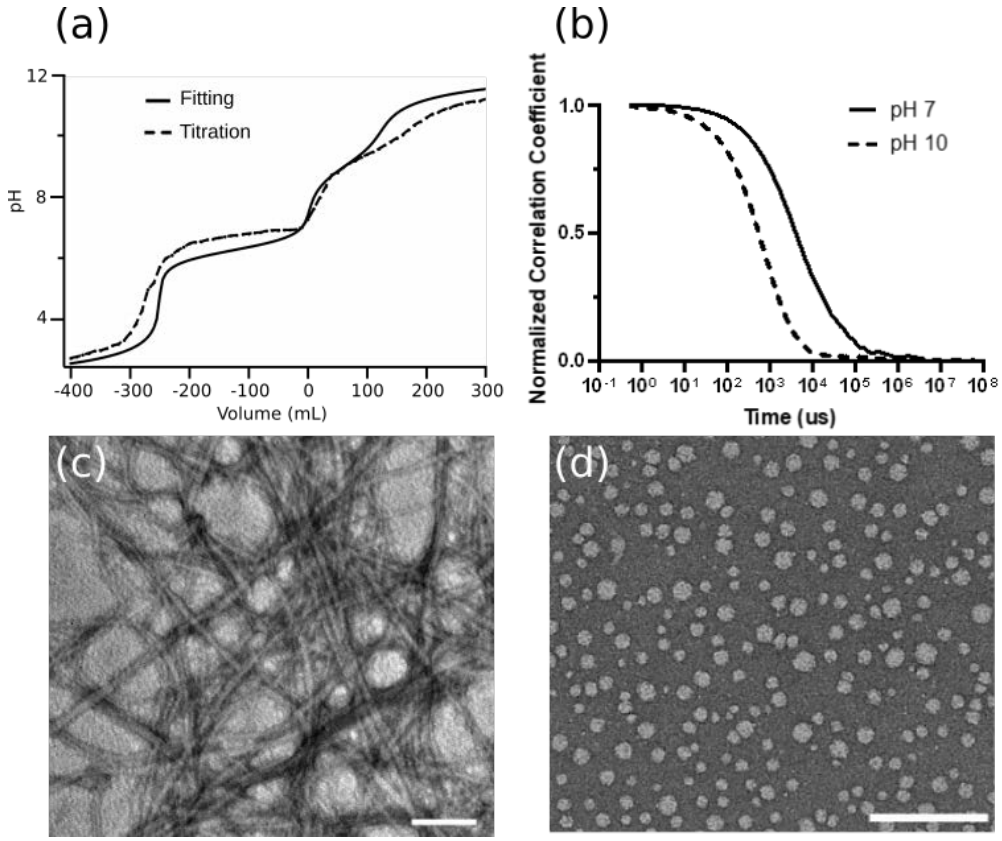

Figure 2.7: (a) Titration and fitting curves of $C_{12} - VVEE$. (b) Normalized correlation coefficient functions for solutions of 100 mM $C_{12} - VVEE$ assembled at pH 7 and 10 at 25.0 °C. Representative transmission electron microscopy (TEM) images of supramolecular nanostructures formed by $C_{12} - VVEE$ at (c) pH 7 and (d) pH 10. Prior to imaging, TEM samples were negatively stained using an aqueous solution of 2 wt % uranyl acetate. Scale bars indicate 200 nm.

the self-assembled structures formed by C_{12}-VVEE when the solution pH is changed from 7 to 10. Dynamic light scattering (DLS) is first used to probe the size changes. Given the difficulty of accurately fitting the filamentous nanostructures with a mathematical model, we use the correlation functions to qualitatively assess their size differences. These correlation functions can be

calculated from the time-dependent intensity trace using the equation

$$G(\tau) = \int_0^\infty I(t)I(t+\tau)\mathrm{d}t \tag{2.5}$$

As can be seen from **Fig. 2.7b**, solutions at both pH 7 and 10 show evidence of the formation of self-assembled structures. At pH 10, the curve is steeper and decays more rapidly at a much shorter time scale than that at pH 7, implying the formation of smaller particles of less polydispersity. These data corroborate our simulation results, which suggest that at pH 10, C_{12}-VVEE forms filamentous nanostructures at pH 7 but spherical particles at pH 10.

The structural transition from filamentous nanostructures at pH 7 to discrete particles at pH 10 was further validated by using transmission electron microscopy (TEM) imaging. **Fig. 2.7(c)(d)** reveals clearly that C_{12}-VVEE assembles into filaments at pH 7, but discrete particles of varying sizes (diameter: $18.9 \pm 9.6\mathrm{nm}$) at pH 10. The irregularity in particle shapes may be attributed to a drying effect during the TEM sample preparation and staining process, in which the peptide amphiphile concentration and solution pH were likely varied. Nevertheless, a clear morphological transition in the assembled C_{12}-VVEE structure is observed as the pH was raised from 7 to 10. The experimental results are highly consistent with the theoretical predictions.

To determine the possibility of micellization in PA with longer hydrocarbon tails, another PA fiber consisting of C_{16}-VVEE is modeled and simulated (**Fig. 2.8**) with different charge states. Similarly, in one system, both GLUs in the PA are fully charged, while in the other system, only E_2 is charged. Compared with the C_{12}-VVEE systems, both C_{16}-VVEE systems form fibers. The hydrophobicity is stronger in the C_{16}-VVEE systems, which compensates for the electrostatic penalties, even when both GLUs are charged. Similar to results from the artificial C_{12} fiber, the ions concentrate more and diffuse deeper into the fiber when the nanofiber carries 2 negative charges (**Fig. 2.8b**). During the equilibration, the doubly charged fiber quickly expands in the z direction to decrease the linear

charge density (**Fig. 2.8c**). On the contrary, the single charged fiber further condenses during the equilibration. The linear density of the half-protonated fiber (20.86 PA/nm) is 59% larger than the fully charged fiber (13.1 PA/nm), while the radius of the half-protonated fiber is only slightly larger than the fully charged fiber. The half-protonated fiber has fewer extended PA chains and hence a much more compact structure. The simulations further demonstrate that regardless of the assumptions on the charge states of PA molecules, MD simulations produce qualitatively similar results. However, significant quantitative inconsistencies are observed. Moreover, here, we simulated the physical properties of the fibers without the presence of other molecules. Large differences in molecular binding should be expected when other molecules are included.

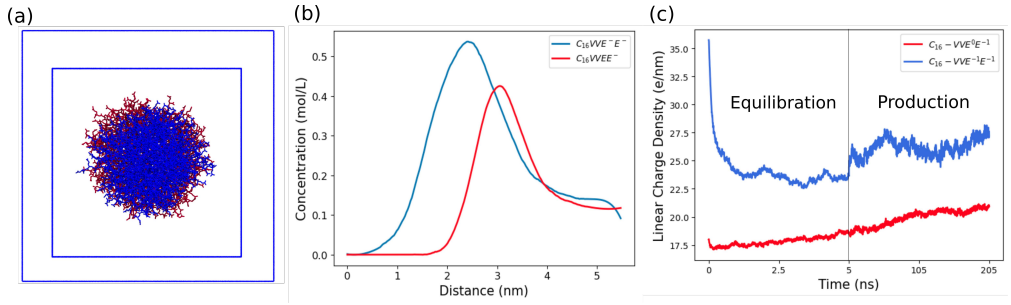

Figure 2.8: All-atom simulations for $C_{16}VVEE$ fibers. (a) Final snapshot of the $C_{16}VVE_1E_2$ fibers. The red surface is the half-protonated fiber, the blue surface is the fully charged fiber, and the blue squares are the simulation boxes. Two snapshots overlap to show the relative size of the fibers. (b) The ion condensation of the two systems. The peak of ion concentrations in the fully charged fiber system is much higher, indicating a stronger ion condensation. (c) The linear charge density of fibers. The double-charged fiber quickly expands to reduce charge density.

The oversimplified model with all amino acids charged does not construct a stable cylindrical fiber in the C_{12}-VVEE system because of the short hydrophobic chain and weaker hydrophobic interactions compared with other simulation work[23,24,25] on PA superstructure systems. Notably, for other PA systems, the all-charged model may generate desired superstructures despite the inaccurate assumption, but it does not give accurate descriptions of physical properties. Extra caution

is required if the all-charged model is used to study systems involving complex interactions, such as molecular binding and phase separation. Overestimation of the charge density could lead to distinct ion distributions and electrostatic potentials over superstructures' surfaces. Therefore, the oversimplified model possibly introduces challenges in calculating effective charges and predicting interactions involving PA superstructures. Careful examination and validation should be performed to determine the actual charge states of PAs in superstructures.

2.1.3 Method

Atomistic Simulations

GROMACS 2021.5[26] is used to perform molecular dynamics (MD) simulation in this paper. GROMACS is an MD package mainly designed for simulations of large biomolecules. The CHARMM36[27] force field is used for all-atom simulations. The CHARMM TIP3P combined with the SETTLE algorithm[28] is used to model water molecules. All visual analyses are performed with VMD[29] and MDAnalysis[30].

The PA molecule is initialized with Avogadro[31] and Packmol[32]. On the xy-plane, 9 PAs are distributed radially with an angle of 40° between each other to form the first layer. The second layer of 9 PAs is placed 0.5 nm above the first layer with a 20° shift. A total of 16 layers are created to initialize the fiber[33]. The fiber is solvated in water with 0.1 M NaCl except for the counterions. The initial structure is shown in **Fig. 2.3**. The system is equilibrated with gradually decreasing force constants applied on the C_{12}. A subsequent production run is performed on the fully relaxed system for 200 ns. All detailed parameters for the simulation can be found in the Appendix A. The final simulation snapshots are shown in **Fig. 2.4**. Same procedures are performed for C_{16}-VVEE PA systems.

Coarse-Grained Simulation

GROMACS 2021.5 and MARTINI 3 force field[34] are combined in the coarse-grained simulations. The details of the PA bead mapping are provided in **Fig. A.3** in Appendix A. We solvated 150 PAs in an aqueous solution at 0.1 M NaCl salt concentration along with counterions in a $9 \times 9 \times 9$ nm^3 box. Energy minimization is first performed on the system, followed by equilibration under NVT (constant number of molecules, constant volume, and constant temperature) ensemble and then NPT (constant number of molecules, constant pressure, and constant temperature) ensemble. A subsequent production run is performed for 1 μs. Detailed parameters for the simulations are listed in Appendix A.

Local Debye Length

The original formula for Debye length calculation is

$$\lambda_D = \sqrt{\frac{\varepsilon_r \varepsilon_0 k_B T}{\sum \left(Z_i e\right)^2 C_i}} \tag{2.6}$$

The Debye length depends on the ion concentrations and the relative permittivity. In the specific system, Na^+ tends to concentrate around the fiber to neutralize the negative charges carried by the PA molecules. The dielectric constant is assumed to be proportional to the volume fraction of oil (ε_r = 2) and water (ε_r = 80). Therefore, the Debye length varies, depending on the radial distance from the fiber center.

$$\lambda_D\left(r\right) = \sqrt{\frac{\varepsilon_r\left(r\right) \varepsilon_0 k_B T}{\sum \left(Z_i e\right)^2 C_i\left(r\right)}} \tag{2.7}$$

The local ion concentration can be calculated based on the simulation results with the radial distribution function (RDF)

$$C\left(r\right)=\frac{\mathrm{d}N}{\mathrm{d}V}=g(r)\times\rho_{0} \tag{2.8}$$

with a 2D radial distribution, $\mathrm{d}V=4\pi r\mathrm{d}r$. Therefore, the local Debye length is

$$\lambda_{D}\left(r\right)=\sqrt{\frac{4\pi r\mathrm{d}r\times\varepsilon_{r}\left(r\right)\varepsilon_{0}k_{B}T}{\sum\left(Z_{i}e\right)^{2}\mathrm{d}N_{i}}} \tag{2.9}$$

Titration on PA Solutions

First, PA solutions are prepared. The lyophilized peptide amphiphile powders are first pretreated with 400 μL of hexafluoro-2-propanol (HFIP) to eliminate any pre-existing structures before assembly. After evaporating off the HFIP under compressed air for a minimum of 20 min until a dry thin film formed at the bottom of the tube, enough Nanopure water is added to reach a final concentration of 2.5 mM. The peptide amphiphile solutions were sonicated in a 45 °C water bath for 40 min before being left overnight in a closed Eppendorf tube at room temperature to allow for complete assembly, and the pH was measured before and after the overnight assembly. The preparation of the fibers was done following the protocal described in refs[35] and[36]. Titration curves are determined by adding 10 μL of 0.1 M NaOH or HCl at a time to 5 mL of the peptide amphiphile solutions. After each addition of NaOH or HCl, the pH is measured, which is calibrated prior to experiments using pH 4, 7, and 10 buffers.

Fitting of the Titration Curve

The $\mathrm{C_{12}}$-VVEE molecule is denoted as $\mathrm{H_2A}$ for simplicity. The acid-base equilibrium is considered with the following equations

$$\mathrm{H_2A}+\mathrm{H_2O}\rightleftharpoons\mathrm{H_3A^{+}}+\mathrm{OH^{-}}\qquad\qquad K_{b} \tag{2.10}$$

$$\mathrm{H_2A} \rightleftharpoons \mathrm{HA^-} + \mathrm{H^+} \qquad K_{a_1} \tag{2.11}$$

$$\mathrm{HA^-} \rightleftharpoons \mathrm{A^{2-}} + \mathrm{H^+} \qquad K_{a_2} \tag{2.12}$$

With species conservation and charge neutrality, two final expressions are reached

$$w + \left[\mathrm{H^+}\right] + \frac{c_B V_B}{V_B + V_0} = \frac{K_w}{[\mathrm{H^+}]} + \frac{w K_w K_{a_1}}{[\mathrm{H^+}]^2 K_b} + 2\frac{w K_w K_{a_1} K_{a_2}}{[\mathrm{H^+}]^3 K_b} \tag{2.13}$$

$$w + \frac{w K_w}{[\mathrm{H^+}] K_b} + \frac{w K_w K_{a_1}}{[\mathrm{H^+}]^2 K_b} + \frac{w K_w K_{a_1} K_{a_2}}{[\mathrm{H^+}]^3 K_b} = \frac{c_0 V_0}{V_B + V_A} \tag{2.14}$$

where w is the concentration of $\mathrm{H_3A^+}$; Kw is the water dissociation constant; V_B is the volume of NaOH/HCl added; V_0 and c_0 are the initial volume and concentration of the $\mathrm{H_2A}$ solution. The two equations allow for extrapolation of the titration curve with the volume of NaOH/HCl added. More details can be found in the Appendix A.

2.2 Microscopically segregated ligand distribution in co-assembled peptide amphiphile nanofibers

Authors: Turash Haque Pial, Yang Li, and Monica Olvera de la Cruz.
This work is adapted from *Soft Matter, 2024,20, 4640-4647,* https://doi.org/10.1039/D4SM00315B.
M. O. d. l. C. acquired the funding and led the project. T. H. P. and Y. L. performed the simulations, T. H. P. and M. O. d. l. C. wrote the manuscript.

2.2.1 Introduction

Previously we discussed that for a system only contains one kind of PA molecules, the charge regulation plays an important role. Here in this section, the second fictionalized PA molecules are introduced to the system. The chemical structure was shown in **Fig. 2.9**.

Peptide Amphiphiles are a class of molecules consisting of peptide heads connected to hydrophobic alkyl tails that can self-organize in aqueous solutions. This self-assembly behavior is often driven by the tendency of hydrophobic domains to bury away from water while hydrophilic peptide regions to expose to the solvent. The ability of peptide amphiphiles (PAs) to selfassemble into fibers, membranes, and micelles has been widely explored for achieving functions such as mineralization, cell proliferation, molecular imaging, drug delivery, and pH sensing[37,38,39,40,41,42,43,44,45,46,47,48,49,50]. One of the critical advantages of PAs is their ability to be modified with specific ligands to achieve the desired functionality. For instance, PA nanofibers modified with ligands have shown potential in purifying antibodies[35,21]. Therefore, understanding the distribution of ligands on the nanofiber surface is extremely important to optimize functionalization, thereby enabling their widespread application in biomedical research and therapeutics.

Peptides can carry charge, and it has been observed that oppositely charged peptides can facilitate the co-assembly process of PAs with different peptides and epitopes. Coassembly by mixing oppositely charged PAs is a powerful way to achieve increased functionalities. Niece et al[51]. first

reported the importance of opposite charges on the co-assembly of PAs functionalized with different bioactive sequences, of which each bearing a different biological signal. Recently, Li et al[35, 21]. showed the assembly of negatively charged C_{12}-VVEE (filler) and positively charged C_{12}-VVKK–OEG_4–Z33 (ligand) to capture and purify IgG antibodies. Z33 is a 33 amino acid derivative (FNMQQQRRFYEALHDPNLNEEQRNAKIKSIRDD) of protein A[52] which strongly binds to the Fc domain of the antibody[53]. Their experiment suggests that aggregation of Z33 can reduce the purification efficiency as the steric effect may hinder Z33 from accessing and binding effectively with antibodies.15,16 As the demand for therapeutic antibodies continues to increase[54], it is crucial to understand the factors affecting the mechanism to recover antibodies. Here we exploit the co-assembly and distribution of positive ligands in a nanofiber made with negative filler PAs.

Phase segregation is a common phenomenon in amphiphilic supramolecular structures involving competitions among different driving forces[55,56,57]. Careful truing the competing forces is an effective method to design nanomaterial architecture and achieve functions[58,59,60]. To understand the physical origin of the supramolecular structure created by competing forces, previous theoretical works have analyzed the distribution of oppositely charged molecules absorbed on flat and cylindrical surfaces[61,62]. The model suggested that oppositely charged molecules with different cohesive energy or compatibility can induce the formation of charged domains or aggregation of molecules on the surface[61]. This is due to the competition between the line tension, and electrostatic energy. Line tension favors the growth of domains of segregated components of similar compatibility, while electrostatic repulsion increases rapidly as the surface charge density and the size of the domain increase. However, those models although can include the curvature of cylindrical fibers[61,62,63], lacked the complexity of real PAs and ligands. The possibility of small clusters or aggregation of molecules with similar compatibility and lack of homogeneity in ligand distribution

is also suggested by stochastic optical reconstruction microscopy in Stupp group[64]. Besides these works, there is a dearth of knowledge on understanding the co-assembly of oppositely changed PAs and ligands distribution in a co-assembled surface.

In this study, we use molecular dynamics simulations to coassemble oppositely charged filler and ligand PAs. We use the capability of the Martini3 coarse-grained model to simulate large time and length scales. We have also employed all-atom simulation to verify ligand aggregation. We find that ligands come close to each other in the assembled fiber and form clusters on the surface. We discussed the importance of attractive interactions between ligands and electrostatics of the fiber surface in creating local segregation of ligands.

2.2.2 Discussion

C_{12}-VVEE is an ideal candidate for forming one dimensional self-assembled structure. C_{12} is the hydrocarbon hydrophobic core, V (valine) provides hydrogen bonds, hydrophobicity and E (glutamic acid) is negatively charged and hydrophilic. Our previous study shows that only the outer E of the PA is deprotonated or carries $1e$ charge[65] in a self-assembled fiber. Keeping this in mind, we also model the inner glutamic acid as protonated. K (lysin) is used as positively charged group in our simulation in C_{12}-VVKK–OEG_4–Z33 ligand. Z33 acts as an epitope in the ligand with OEG_4 (oligoethylene glycol) helping as the spacer group. We used Martini 3 force field[34] which averaged 2–4 heavy atoms into one bead and was extensively used in many amino acid simulations.

The randomly added fillers and ligands initially form micelles and then assembled into a fiber. To differentiate the effect of Z33, we start our analysis with observing co-assembly of C_{12}-VVEE and C_{12}-VVKK. Interesting differences in the distribution of C_{12}-VVKK and C_{12}-VVKK–OEG_4–Z33 can be seen from the snapshot of the assembled fibers (**Fig. 2.9**) where C_{12}-VVEE act as filler chains. C_{12}-VVKK are randomly distributed in the fiber (upper panel), while C_{12}-VVKK–OEG_4–Z33

ligands come together and form ligands-rich regions. No distinct clusters of C_{12}-VVKK is observed in the upper panel, but we see C_{12}-VVKK–OEG_4–Z33 ligands form clusters in the fiber surface.

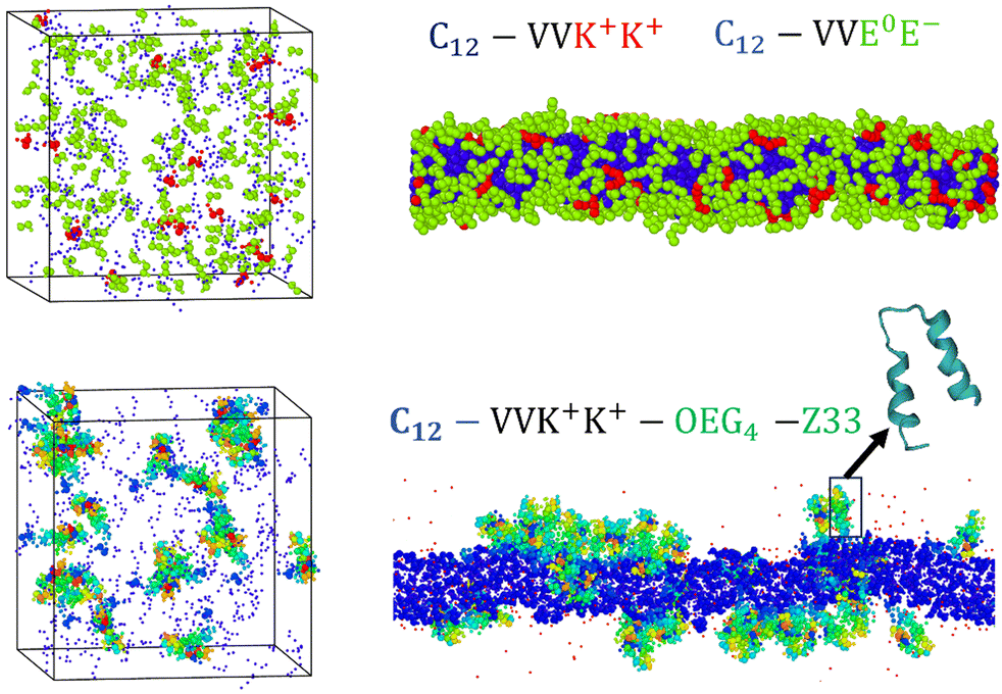

Figure 2.9: Simulation snapshots of the initial and co-assembled stages. Upper panel shows the distributions of lysin (red) and glutamic acid (green) amino acids in the assembled fiber. Lower panel shows the distribution of ligands in the fiber surface. A double alpha-helix structure of Z33 is shown in the inset. Water, ions, valines are omitted from the snapshots for better visualization. In both cases the ratio between ligand and filler are 1/10 and no extra salt is added except counterions.

To better understand the distribution, we have calculated the cluster size distributions of Z33. The cut-off distance of Z33 beads was set to 0.7 nm when calculating the cluster; two Z33s are considered to form a cluster when they have at least one pair of beads closer than 0.7 nm. We chose 0.7 nm as the cut-off as it is the first valley of the radial distribution function of the Martini3 beads and is also suggested in previous studies as the optimal cut-off distance for amino acid cluster

analysis[66,67]. Additionally, we checked the cluster size distribution of C_{12}-VVKK for comparison (the simulation snapshot is shown in **Fig. 2.9**, upper panel). We used 1.1 nm as the cut-off distance between K of different PAs for this case, as it represents the second valley of the radial distribution function of the Martini3 beads and would consider two C_{12}-VVKK to form a cluster even if they are separated by one layer of C_{12}-VVEEs.

In **Fig. 2.10** we plot the cluster size probability distribution for various ligand-filler ratios and two salt concentrations. Comparison between C_{12}-VVKK and C_{12}-VVKK–OEG_4–Z33 (salt 0.0 mM) can be observed from **Fig. 2.10(c)**. A quick drop in the probability value with increasing N shows that C_{12}-VVKK does not form large clusters, they stay separated from each other. Electrostatistically this is reasonable as positively charged groups prefer to mix with oppositely charged groups to minimize the electrostatic energy. On the other hand, larger clusters are observed when we add the Z33 ligands.

From **Fig. 2.10(b)–(d)**, we can see that the probability of finding small clusters reduces with increasing the concentration of the ligand. More interestingly, we see a non-monotonic reduction of the cluster probability with increasing the number of ligands in a cluster, N arise. This non-monotonic cluster size distribution is associated with micellar aggregation[68,69,70]. Srebnik and Douglous also observed this kind of cluster size distribution, where positive and negative coarse-grained beads were aggregating in a neutral nanotube surface[71]. A small but finite probability for a very large cluster size indicates the formation of large clusters by transient bridges between more persistent smaller structures. The effect of salt can be easily understood from these plots. The addition of 100 mM salt results in smaller clusters of ligands for all ligand concentrations.

To clearly understand how ligands are distributed in a fiber surface, we have plotted the distribution of Z33 ligands by mapping them onto a plane. To do this, we calculated the angle each Z33

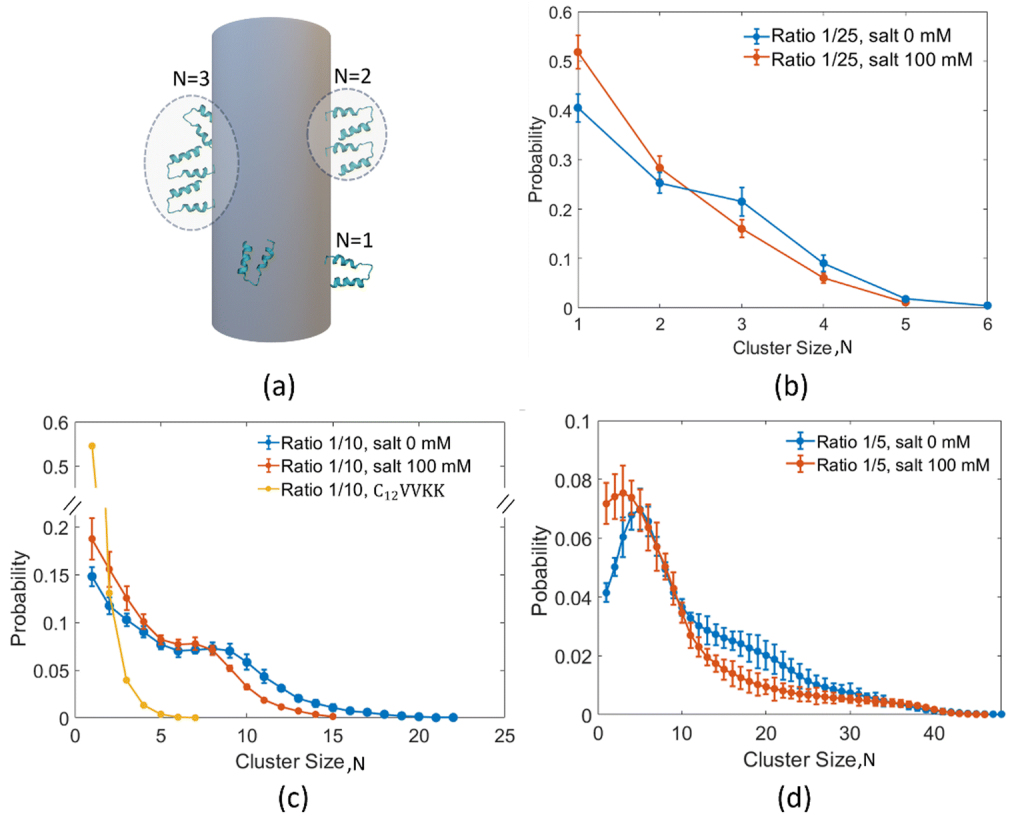

Figure 2.10: Cluster size distribution. (a) A cartoon representation of the cluster size (N) definition. (b)–(d) shows the cluster size distribution probability for ligand-filler ratio of 1/25, 1/10 and 1/5 respectively.

forms with the fiber center and the x-axis by taking each Z33's center of mass. We then plotted these angles against the axial position of each Z33 along the fiber, which gave us a rectangular visualization of their distribution on the cylindrical surface of the fiber. The mapping is depicted in a cartoon in **Fig. 2.11** (top panel). Red arrows indicate new positions of Z33s in the mapped plane. We multiplied the visualization twice in the radial and axial directions to account for periodicity (**Fig. 2.11(a)–(c)**).

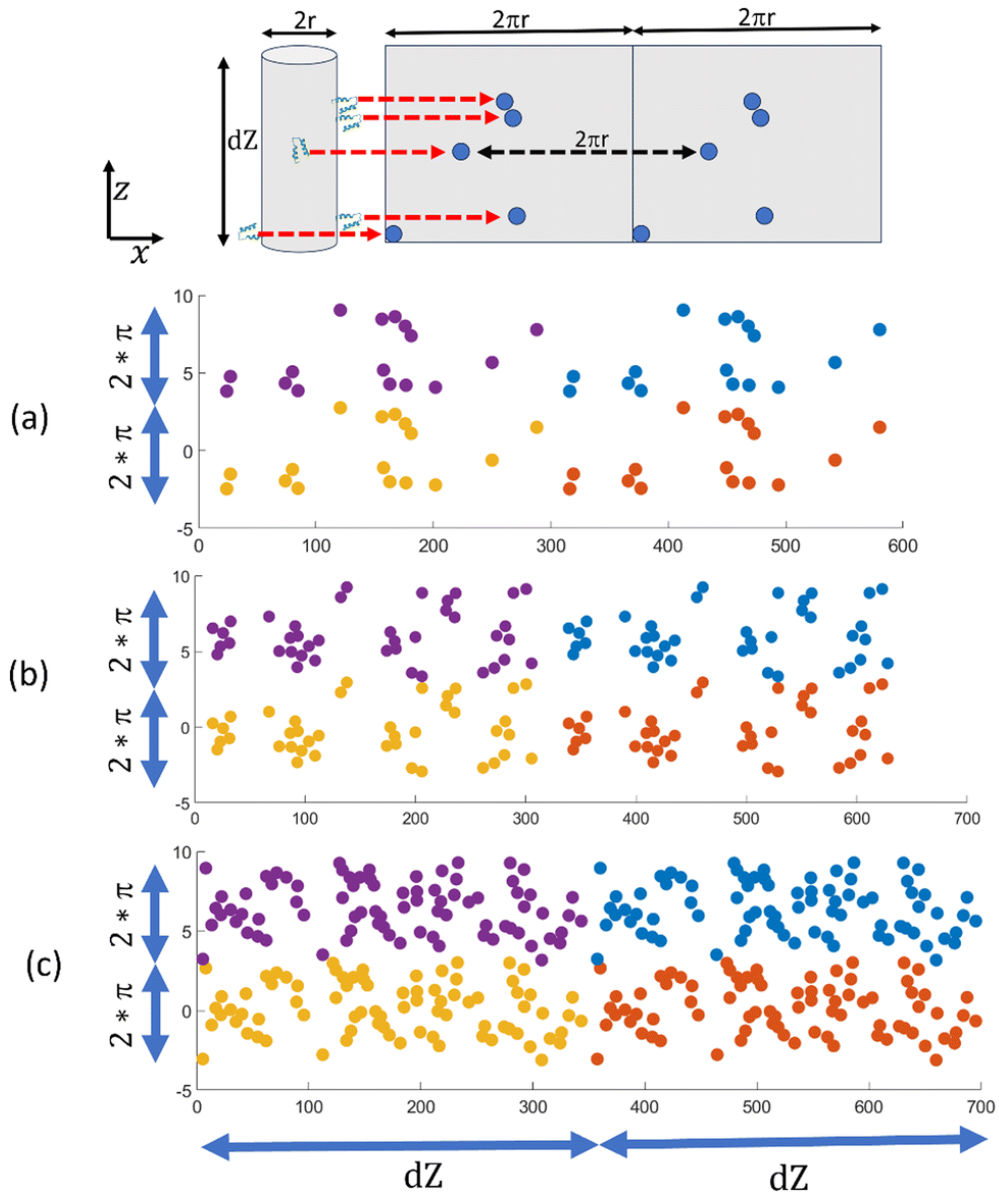

Figure 2.11: Top panel shows the cylinder (radius r) to plane (width $2\pi r$) mapping. Red arrows indicate new positions of Z33s in the mapped plane. Mapped distribution is repeated twice in radial direction for periodicity. (a)–(c) show the mapped distribution for ligand-filler ratio of 1/25, 1/10 and 1/5 respectively. Four color indicates 4 periodic distributions.

In **Fig. 2.11**, we have plotted the distribution of Z33 for ligandfiller ratios of 1/25, 1/10, and 1/5

(without any additional salt) in (a), (b), and (c), respectively. The plots clearly show that Z33s are forming clusters. What is more, all three distributions exhibit regions with high Z33 concentrations as well as areas without any Z33s. This is an example of local or microscopic segregation, which has been proposed in previous theoretical analyses[61,62,63]. Recent studies also suggested the possibilities of similar segregation in other structures, like in charged polymer vesicles, polyelectrolyte brushes[72,73]. Microscopic segregation arises from two competing forces: a short-range attractive force that encourages molecules to come close and form large-scale aggregates or macroscopic segregation, and a long-range repulsive force that opposes it. In the following sections, we will delve into the opposing factors in our case that could result in the local separation of ligands on the fiber surface.

To understand why we are seeing local segregation of Z33s or ligands, we analyzed how Z33 aggregates in the bulk. Randomly added Z33s aggregate in both Martini3 (**Fig. 2.12(a)**) and all-atom (**Fig. 2.12(b)**) force fields (we are showing two simulation boxes for better visualization). These simulations show that, in bulk solutions, Z33s form large aggregates or macroscopic segregation, suggesting strong attractive interactions between Z33s. Simulations with 100 mM added salt show a weaker aggregation behavior for both Martini3 and all-atoms (**Fig. 2.12(c)(d)**); one or two Z33s stay separated from the aggregates. To quantify the aggregations for different cases, we calculated the number of nearest neighbors (NN) for each Z33. This number indicates how many Z33s are in close contact with another Z33 (0.7 nm is used as the cut-off). **Fig. 2.12(e)** shows the neighbor number distribution for Martini3, and all-atom have similar profiles, although Martini3 shows a slightly higher probability for large NN. A weaker aggregation with the addition of salt is apparent from the reduction of probability at higher NN. This weaker aggregation can describe the salt concentration-dependent cluster size distribution discussed in **Fig. 2.10**; the addition of salt reduces the probability of having a large cluster. This demonstrates the importance of controlling

attractive interactions among ligands to regulate the cluster size in fiber surfaces.

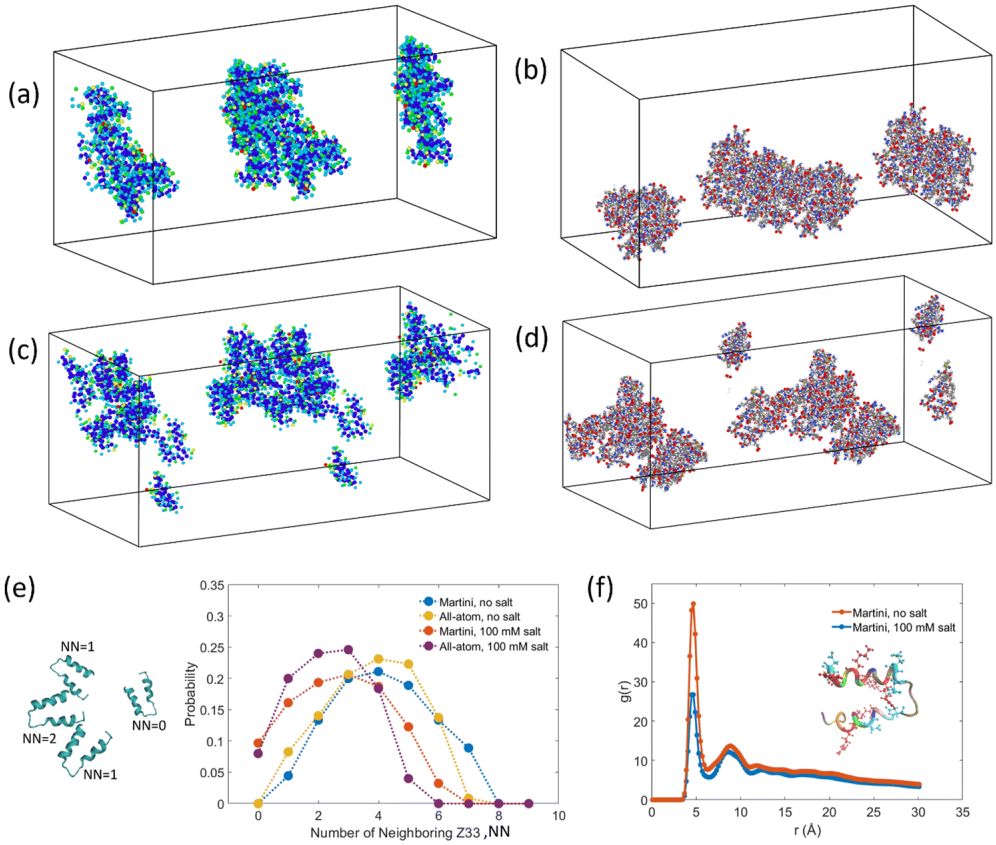

Figure 2.12: Aggregation of Z33 in bulk solution. (a)–(d) shows snapshots of Z33 aggregation for Martini3 (a) and (c) and all-atom simulation (b) and (d) with no added salt (a) and (b) and 100 mM salt (c) and (d). Two periodic images are shown for better visualization. (e) Nearest neighbor analysis for the simulations shown in (a)–(d). A cartoon representation is added to help understand the nearest neighbor definition. (f) Radial distribution function plot of positive and negative amino acids beads of Z33 in Martini3 simulations. Inset showing the positive (red) and negative (teal) amino acids.

We know that protein aggregation in water is complicated and involves several factors, such as the interaction between hydrophobic amino acids, electrostatic interactions, hydrogen bonds, and the compactness of the protein. There are van der Waals and electrostatic energy gain associated

with Z33 aggregation as some of the 33 amino acids are hydrophobic and nonpolar (see **Fig. A.5**, Appendix A), which prefer to stay away from polar water. Although the total charge of a Z33 is zero, some of the 33 amino acids are charged; positively charged amino acids are shown in red, and negatively charged amino acids are shown in teal color in the inset of **Fig. 2.12(f)**. When the salt concentration is low, these positively charged and negatively charged amino acids form strong electrostatic interactions, leading to stronger attractive interactions. However, adding salt neutralizes some of the charged amino acids and reduces the electrostatic interactions, as seen in the radial distribution plot of positive and negative beads of the charged amino acids in **Fig. 2.12(f)**. The addition of salt reduces the value of g(r) which indicates a less attractive electrostatic interaction between positive and negative amino acids at high salt concentrations.

We conducted three additional simulations to verify that the electrostatic penalty linked with large clusters of positively charged ligands in a negatively charged fiber might cause the local segregation of ligands in the fiber. We modified our original ligand from C_{12}-VVKK–OEG_4–Z33 to C_{12}-VVEE–OEG_4– Z33 by replacing the positive lysin (K) with negative glutamic acids (E) in an already co-assembled fiber. We have depicted the cylinder-to-plane mapping of the ligands in **Fig. 2.13** using similar methodologies in as **Fig. 2.11**. We can see more connected ligand clusters are observed for all concentrations. No electrostatic penalty is associated with large clusters for these modified ligands, as all the molecules in the fiber now have similar charges. As a result, cluster formation is wholly driven by Z33–Z33 attractions, which can generate extensive, separated regions of ligand-rich and filler-rich surfaces.

It is worth mentioning that we have performed our simulation with C_{12}-VVEE–OEG_4–Z33 starting with a co-assembled structure to distinguish the effect of electrostatics in local segregation, we have not checked the co-assembly process itself. Because of very large differences in

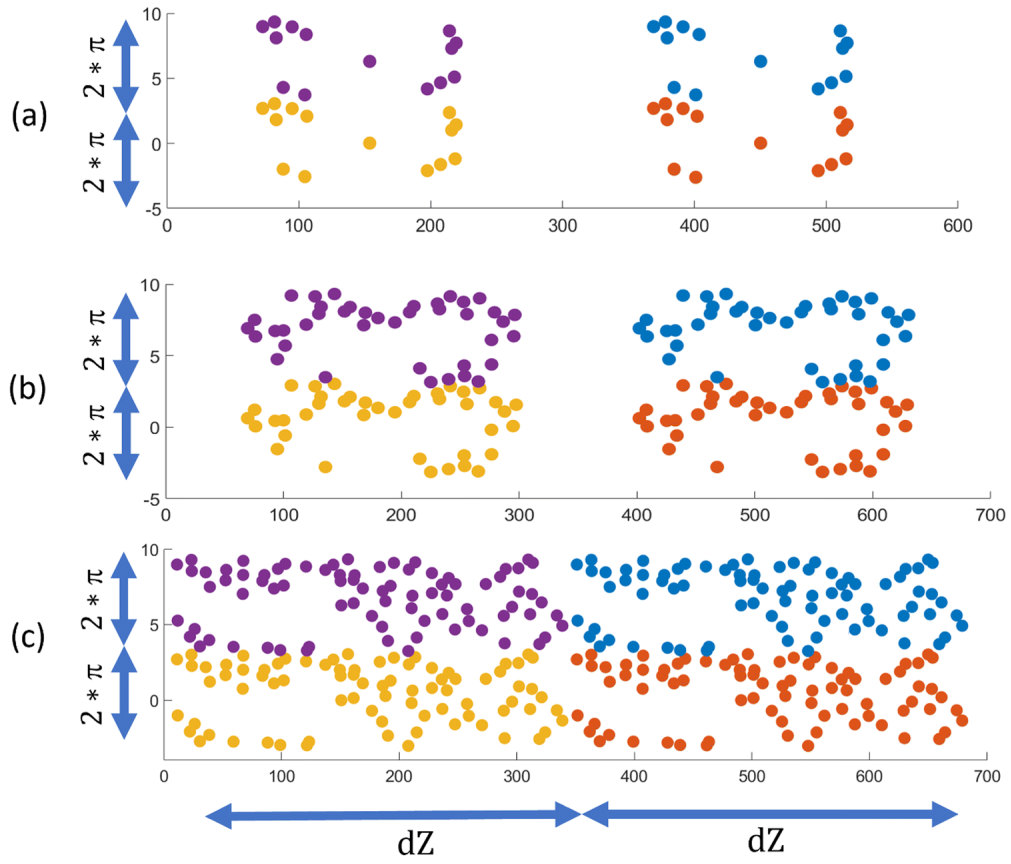

Figure 2.13: (a)–(c) shows the mapped C_{12}-VVEE–OEG_4–Z33 ligands distribution for ligand-filler ratio of 1/25, 1/10 and 1/5 respectively. Four color indicates 4 periodic distributions

cohesive energy between C_{12}-VVEE and C_{12}-VVEE–OEG_4–Z33, co-assembly should be less favorable without any added benefit coming from opposite charges. We have also observed some instability in the fiber when few ligands came close (**Fig. A.8(a)**, Appendix A), although we did not observe any demixing of C_{12}-VVEE–OEG_4– Z33 from the fiber during 10 ms of simulation time. We have performed two simulations to check the relative co-assembly of oppositely charged (C_{12}-VVEE and C_{12}-VVKK–OEG_4–Z33) and similarly charged (C_{12}-VVEE and C_{12}-VVEE–OEG_4–Z33) ligands and fillers. All the oppositely charged C_{12}-VVKK–OEG_4–Z33 ligands entered the already assembled fiber of fillers (upper panel, **Fig. A.8(b)**, Appendix A) showing

good mixing or co-assembly behavior. On the other hand, only 3 of the 16 added similarly charged C_{12}-VVEE–OEG_4–Z33 ligands enter the fiber after 1 ms, indicating a significantly lower propensity of co-assembly.

2.2.3 Method

GROMACS 2021.5[26] and MARTINI3 force field[34,74] are combined in the coarse-grained simulations. We used similar definitions of MARTINI3 beads for C12 as defined in our previous work[65] and mapped bond, angle parameters with allatom simulation. Our previous work showed that Martini 3 would provide a similar fiber structure to CHARRM36 force-field. We used Martinize2[75] to get amino acid parameters which can define bead types, bond, angle, dihedral parameters and can constrain protein's secondary structure. Initially, we solvated 200 fillers and 8 ligands in an aqueous solution in a $14 \times 14 \times 14\mathrm{nm}^3$ box resulting a 1/25 ligand-filler ratio. We used regular waters beads in Martini 3 simulations. We have increased the number of ligands and box size for other ratios. We have also added required numbers of counterions and salts. Energy minimization is first performed on the system, followed by equilibration under NVT (constant number of molecules, constant volume, and constant temperature) ensemble and then NPT (constant number of molecules, constant pressure, and constant temperature) ensemble. After the co-assembly of filler and ligands, we have replicated the fiber along the axial direction of the fiber, which doubles the number of fillers, ligands and gives better statistics. We have also increased the simulation box size in the other two directions and solvated with new water and ions (we changed the ligand type for **Fig. 2.13** in this stage). Then we performed the energy minimization and equilibration under NVT for 500 ns and semi-isotropic NPT for 10 ms. The last 3 ms was considered as the production run. 3 copies of simulations are performed to get error bars. For Z33 aggregation in bulk simulations (**Fig. 2.12**), we have added 10 Z33s in a $13 \times 13 \times 13\mathrm{nm}^3$ simulation box and

added required water and ions. The CHARMM36[27] force field was used for all-atom simulations and the recommended CHARMM TIP3P water model was applied with the SETTLE algorithm[28]. Other simulation parameter details can be found in the Appendix A. We used Ovito[76] for clustering (see **Fig. 2.10**) and visualizations. To calculate the nearest neighbor (**Fig. 2.12(e)**), we got the contact map from VMD[29]. This contact map contained the residue-residue minimum distance information and combined with in-house code to get nearest neighbor probability. A such contact map for all-atom, no salt system is shown in **Fig. A.7** (Appendix A). We have also used VMD to get the g(r) shown in **Fig. 2.12(f)**.

2.3 Future Perspectives

Antibody purification with PA self assembled nanofibers is a complex process involving mulitple stages. In previous sections, I have discussed the first stage where two kinds of PAs self assembled into nanofibers. In this section, I will briefly address on the subsequent stages.

2.3.1 Nanofiber-nanofiber interactions

From previous publications, it is observed that filler-ligand assembled nanofibers form small bundles alone without the presence of IgG (**Fig. 2.14a**). The cause behind the phenomenon remains elucive. One possible cause is the short-range attraction between the Z33 groups among different fibers. As discussed in previous section (Sec 2.2), free Z33 monomers prone to form large clusters. After co-assembled into fibers, the Z33 groups can still attract each other and promote the formation of bundles. The other possible cause is the depletion effect. Given the fact the fiber surface is highly charged, a lot of ions are correlated in the fiber surface, lowering the electrostatic penalty with a trade-off of entropy. When fibers form bundles, some ions are released from the surface, gaining entropy. The system's free energy is lowered. Another cause is that when fibers approach to each other, the positively charged domain in one fiber induce the GLU groups in another fiber to dissociate and bear charges (**Fig. 2.14b**). The electrostatic interaction lower the total energy while releasing an ion increases the entropy in the same time. The free energy of the system is thus lowered.

The impact of bundle formation on the purification process remains ambiguous. First, it is likely that some Z33 groups become buried within the fiber bundles, reducing the number of accessible Z33 groups. Consequently, a greater quantity of fibers or higher filler/ligand ratios would be necessary to capture the same amount of IgG. In industrial settings, this could result in increased

production costs. Second, the formation of bundles may lead to a higher density in the separated phase compared to the phase formed by individual fibers. This could mean that the separated phase might manifest as a solid (precipitation) or as a gel (coacervation), potentially influencing the subsequent separation and recovery stages.

Given these potential implications, it is crucial to thoroughly investigate the bundle formation process. Understanding the conditions under which bundles form, as well as their structural characteristics, will enable more precise control over the purification process.

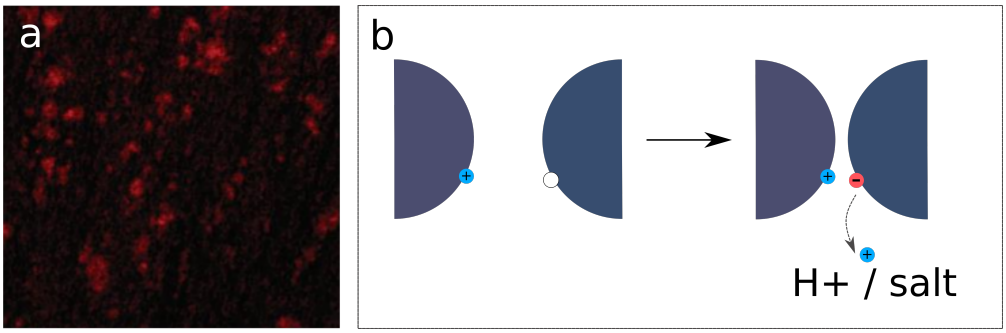

Figure 2.14: (a)TEM image of ligand-coassembled fibers aggregate without IgG. The Rhodamine B fluorescence was monitored to show the aggregation. (b) A cartoon demonstration of positively charged domain induce negative charges in another fiber.

2.3.2 Crosslinks and self-loops between IgG and nanofibers

Z33 is adapted short segment from Protein A and has strong specific binding with IgG Fc domains with a binding ratio of 2:1. From the design of the IgG purification technique, one IgG binds with 2 Z33 in 2 fibers and forms a crosslink. As the interaction proceeds, in the solution there will be local regions enriched with IgG and nanofibers and therefore lead to phase separation.

However, we consider the free energy change in thermodynamic equilibrium

$$\Delta F = \Delta H - T\Delta S \tag{2.15}$$

where the change in enthalpy is approximated by the binding energy between IgG and Z33. If IgG and fibers form a large network in which most IgG molecules create crosslinks among fibers (bridges), the resulting loss in translational entropy is significant. Conversely, in an extreme scenario where each IgG binds only with Z33 from the same fiber (loops), the energy reduction remains constant while the translational entropy of the fibers is largely preserved. The change in free energy is minimun in the latter case. In other words, forming loops rather than bridges is thermodynamically favorable.

From the kinetic perspective, the diffusion coefficient of IgG and nanofiber is calculated with Stokes-Einstein-Sutherland equation and rod-like macromolecule diffusion equation respectively[77,78].

$$D = \frac{k_B T}{6\pi\eta r} \tag{2.16}$$

$$3\pi\eta_0 L D_t / k_B T = \ln p + v \tag{2.17}$$

where η is the viscosity of the solution, r is the radius of the sphere, L is the rod length, p is the ratio of rod length and diameter, v is the end-effect corrections. The details can be found in Appendix A2.3. Though the specific length of the fiber cannot be obtained, TEM images suggest a high aspect ratio. As a demonstration, the aspect ratio of the nanofibers is assumed as 10^3, then the ratio between the diffusion coefficients of the IgG and Fiber is $\frac{D_{fiber}}{D_{IgG}} = 10^2$. This indicates that IgG diffuses much faster than the fiber within the system. Once an IgG binds with a Z33, it is likely to bind with another Z33 on the same fiber, given its rapid diffusion in a confined space, making it probable for the IgG to encounter a nearby Z33 group before the fiber diffuses to meet another fiber.

A coarse-grained MD simulation is done to verify the hypothesis. In the initial setup, 108 fibers

with 6480 IgG are mixed in the simulation box. The binding between Z33 and IgG is modelled as bonds. IgG and fibers are coupled with separate Langevin dynamics and with different damping coefficient to simulate the different diffusion coefficients. The simulation details can be find in Appendix A. The first and final snapshots of the system in shown in **Fig. 2.15**. The number of bonds formed is analyzed (**Fig. 2.15d**). IgG first single bonded with a Z33. Once a single bond form, most of the single bonded IgG quickly form loops as predicted.

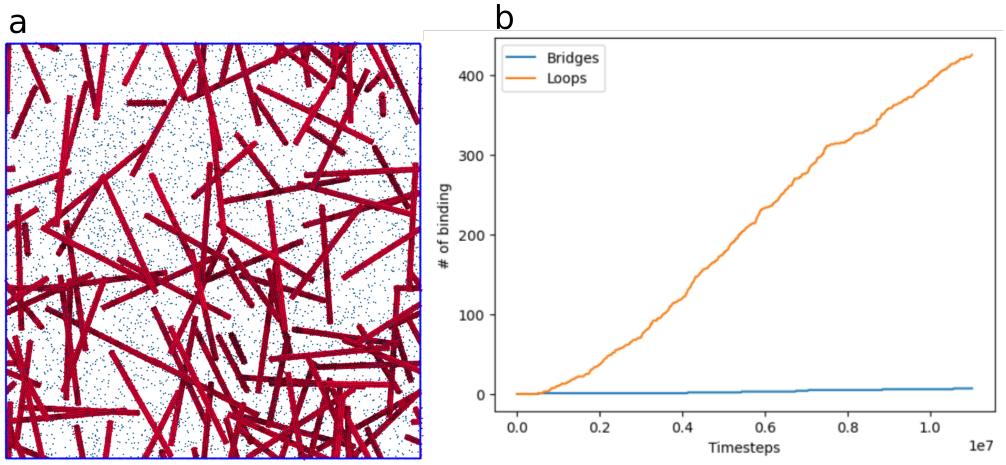

Figure 2.15: (a)The final snapshot of the coarse-grained model. (b) The number of bridges and loops formed in the simulation.

Control over the ratio $\frac{N_{bridge}}{N_{loop}}$ is essential in manipulate the kinetics of purification process. The number of crosslinks could contribute most to the phase separation process. With a low $\frac{N_{bridge}}{N_{loop}}$ ratio, the kinetic is possibly very slow, leading to a prolonged process time, which is unfavored in industrial setting. On the contrary, if the $\frac{N_{bridge}}{N_{loop}}$ ratio is high, the crosslinked network possibly phase separates from the solution prematurely, meaning only a small percentage of Z33 groups actually bind with IgG before the crosslink network forms, significantly lowering the overall yield. Possible ways to alter the binding process include changing the linker length and rigidity, varying the

filler/ligand ratio for assembled nanofibers, post-self-assembly of nanofiber with ligand-pretreated IgG. A deep understanding of the crosslink kinetics is essential in optimizing the purification efficiency.

2.3.3 Conclusion

As mentioned previously, utilizing PA supramolecular immonufiber to selectively capture IgG from upstream is a complex technique involving physics from various field. Beyond the topics discussion in this chapter, there are many other aspects worth attention. For example, what is the critical point at which the crosslinked network phase separates from the solution, and what are the determining factors of this critical point? The ability to decompose and understand this critical point is essential for controlling both the thermodynamic equilibrium and the kinetics of the process. Another critical aspect is the role of hydrodynamics. In the preceding discussion, a coarse-grained model was employed to explore the significance of diffusion. However, the Langevin dynamics does not account for hydrodynamic effects. Moreover, the model was constructed with a relatively high resolution, which confines the simulation's length/time scale due to limited computational resources. To thoroughly investigate the hydrodynamic effects, a more highly coarse-grained model might be required.

The discussions in this chapter focus primarily on the early stages of the process. It is hoped that this exploration will shed light on further studies and inspire continued research in this complex and multifaceted field.

CHAPTER 3

POLY(PROPYLENE SULFONE) SUPERSTRUCTURES AS PROTEIN ANCHORS

Protein adsorption is an extensively investigated area due to its extensive applications in the bio-related field such as drug delivery, biosensors and surface coatings. The phenomenon is a highly complex process with various determining factors. To optimize the application, stable and non-destructive adsorption of proteins onto surfaces is desired. In general, hydrophilic surfaces usually render weak adsorption with low degree of denaturation, whereas hydrophobic surfaces render strong adsorption with high degree of denaturation.

Prof. Evan Scott's group has recently developed a homopolymer, poly(propylene sulfone) (referred to as PPSU) that exhibits extraordinary protein affinity while preserve protein functions (Fig. 3.1). The versatile PPSU polymer can conjugate with various proteins to form different systems such as colloid suspension and hydrogels. With different morphology, PPSU-protein complexes achieve different functions such as drug delivery, controlled drug release. The first section investigates the binding of pure PPSU nanoparticles with proteins with various surface characteristics to prove PPSU's ability to non-selectively binds with proteins. The integrity of adsorbed are analyzed. Subsequently, a multi-component nanomedicine is developed based on the broad affinity and non-destructive adsoprtion of PPSU nanoparticles. In the section second, a block copolymer is developed based on PPSU. The new copolymer retains PPSU's ability to capture proteins without disturbing the integrity and functions. Furthermore the copolymer induced liquid-liquid phase separation once capture proteins. The phase-separated droplet protects proteins from foreign environment. Last section first briefly introduces the application of aggregated PPSU hydrogel in slow drug release, followed by a hypothesis on the mechanism of PPSU self-assemly into various

morphologies.

As an emerging material, PPSU holds significant untapped potential across various fields. This chapter represents an initial effort to explore its possibilities, with the hope that it will inspire further innovative applications of PPSU.

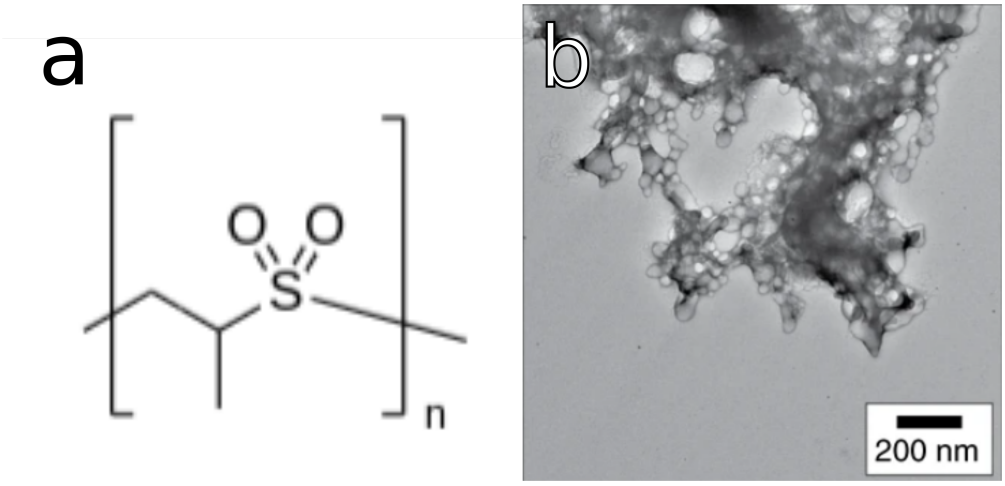

Figure 3.1: (a) The chemical structure of PPSU. (b) The TEM image of PPSU-protein complex.

3.1 Controlled adsorption of multiple bioactive proteins enables targeted mast cell nanotherapy

Authors: Fanfan Du, Clayton H. Rische, Yang Li, Michael P. Vicent, Rebecca A. Krier-Burris, Yuan Qian, Simseok A. Yuk, Sultan Almunif, Bruce S. Bochner, Baofu Qiao, and Evan A. Scott.
This work is adpted from *Nat. Nanotechnol. 19, 698–704 (2024).* https://doi.org/10.1038/s41565-023-01584-z. F.D. designed and contributed to all the experiments, analysed the data and wrote the manuscript. C.H.R. performed the MC experiments, completed the in vivo validation, analysed the data and wrote the manuscript. Y.L. carried out the simulations, analysed the data and wrote the manuscript. M.P.V. contributed to the trypsin proteolysis assay. R.A.K.-B. performed the MC experiments and completed the in vivo validation. Y.Q. performed the cellular uptake studies. S.A.Y. completed the SEM experiments. S.A. contributed to the SAXS measurements. B.S.B. supervised the validation research and wrote the manuscript. B.Q. supervised the simulations and wrote the manuscript. E.A.S. supervised all the research and wrote the manuscript.

3.1.1 Introduction

Nanomaterials that preserve the bioactivity of anchored proteins hold promise for a wide range of applications such as nanozymes, diagnostic sensors and targeted delivery systems[79,80,81]. Although various synthetic platforms have been developed, unmodified nanoparticles(NPs) remain challenging in interfacing with a wide range of proteins without affecting protein folding or function[81,82]. For example, NPs with hydrophobic surfaces tend to irreversibly adsorb protein adlayers,leading to denaturation and associated loss of protein bioactivity[83,84]. It is, therefore, mandatory to involve hydrophilic 'anti-fouling' polymers, such as poly(ethylene glycol) (PEG)[85] and zwitterionic moieties[86,87], within NP surfaces to prevent this non-specific adsorption[88,89,90].

Given their highly hydrophilic surfaces after modifications, most NPs require the tedious process of chemical coupling to reliably interface with proteins to harness their bioactivity[79,80,81,91,92,93]. This method has simultaneously enabled the surface display of targeting antibodies but also typically limited the control to a single antibody type with minimal control over the surface density. Protein adsorption, thus, presents a comparatively facile non-covalent approach to rapidly engi-

neer bioactive NP surfaces with multiple antibodies and proteins. However, the application of this approach is hampered by the continued desorption or loss of activity of the protein layer[94,95,96]. It is noteworthy that controlling the composition and stability of anchored proteins, particularly for multiple antibodies, has remained challenging even when employing chemical coupling strategies, which have conjugation yields dependent on the reactivity of the NP surface and accessibility of binding sites within proteins.

We report on poly(propylene sulfone) (PPSU) NPs that irreversibly adsorb non-specific proteins without compromising the protein function. This ready-to-use protein immobilization platform is effective for both single and multicomponent antibody and enzyme coatings with well-controlled composition. To further demonstrate this design freedom, we engineer PPSU NPs into an antibody-based nanomedicine for selectively inhibiting allergic responses in mast cells (MCs). The nanotherapy requires the controlled co-adsorption of two separate antibodies at an optimized ratio to tune the simultaneous signalling of Siglec-6 and FcεRIα receptors in close proximity on MC surfaces. This therapeutic strategy realizes allergen-selective immunotherapy without triggering anaphylaxis in a humanized mouse model.

3.1.2 Site-specific dipole relaxation stabilizes proteins at PPSU surface

Hollow PPSU NPs (**Fig. 3.2a**) were fabricated at scale (**Fig. B.1**) according to our previous report[97]. As prepared, the NPs are negatively charged on their surfaces with a zeta potential between -30 and -40 mV in an aqueous solution (**Fig. B.1**). We ascribed this phenomenon to the spontaneous orientation of propylene sulfone (PS; **Fig. 3.2b**) at the interface between water and PPSU due to the amphiphilicity inherent within the repeating unit. To explore this postulate, explicit solvent all-atom molecular dynamics (AAMD) simulations of PPSU in water were performed to construct a hollow aggregate that mimics the experimentally observed PPSU NPs. Hollow NPs were formed

in both the 125-chain and 600-chain simulation systems (**Fig. 3.2c**) without a severe deformation or collapse of the shell structures (**Fig. B.2**). Because PS orientation promotes the surface enrichment of polar sulfone groups, the NPs showed increased surface hydrophilicity compared with a single PPSU chain (**Fig. 3.2c**). This was concluded by calculating the ratio of the Coulombic (polar) interactions between PPSU and water to the corresponding Lennard-Jones (non-polar) interactions (**Fig. B.3**). It is noteworthy that the quantitative analysis of surface hydrophilicity has implicitly taken into account the topology and size of the aggregates[98].

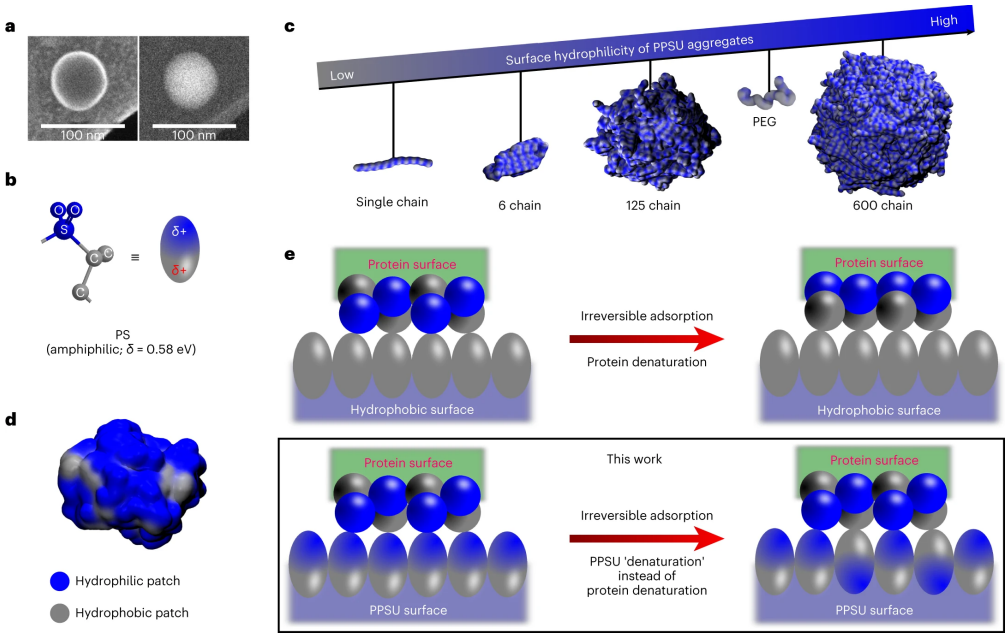

Figure 3.2: Protein-induced dipole rotation of interfacial PS leads to heterogeneous PPSU surfaces that mimic protein surfaces. a, Simultaneous recording of the cryo-STEM and cryo-SEM images, showing a typical PPSU hollow NP and its surface, respectively. b, Schematic of the dipole moment of amphiphilic PS—the repeating unit of a PPSU homopolymer (blue indicates hydrophilic and grey indicates hydrophobic for all the schemes in this Article, unless stated otherwise). c, Atomistic simulations demonstrating enhanced surface hydrophilicity as the aggregation of PPSU chains become disordered. PEG is included for comparison. d, As seen in trypsin using glycine as the reference, the surfaces of water-soluble proteins are heterogeneous, with characteristic patch size distributions based on hydrophobicity. e, Protein induces the formation of locally heterogeneous PPSU surfaces that mimic protein surfaces. Hydrophobic interactions at the interface between this PPSU surface and the adsorbed protein can be sufficiently weak to not outcompete the forces governing protein folding despite irreversible adsorption. Fast spreading of protein on a hydrophobic surface is included for comparison6.

The simulations showed that the PPSU NPs exhibit comparable or even greater surface hydrophilicity compared with that of PEG. However, we were surprised to observe the rapid adsorption of non-specific proteins by PPSU NPs in phosphate-buffered saline (PBS) (**Fig. B.4**). Protein surfaces are chemically diverse, with characteristic distributions of surface-accessible hy-

drophobic patches (**Fig. 3.2d**)[99]. Because the hydrophilic state of PPSU surfaces is induced by the aqueous solvent molecules, we inferred that the dominant orientations of interfacial PS could also be directed by the hydration of adjacent patches experienced at protein interfaces. That is, a hydrophobic protein patch could flip the orientation of interfacial PS, whereas a hydrated hydrophilic patch would preserve the hydrophilic state of PPSU surfaces (**Fig. 3.2e**). Such local hydrophilic/hydrophobic switching events thermodynamically favour the screening of electrostatic repulsion among sulfone groups, leading to small site-to-site heterogeneous NP surfaces at PPSU-protein interfaces.

To investigate the mechanism of protein adsorption, the AAMD simulation of a 600-chain PPSU NP was performed by adding six molecules (the limit set by space constraints) of trypsin in the aqueous system. The last simulation snapshot is shown in **Fig. 3.3a** and Supplementary Video 1*. All six trypsin molecules were adsorbed by the PPSU NP. Calculations of trypsin-NP interactions explicitly supported that the hydrophobic interactions were a major determinant of the adsorption process (**Fig. 3.3b**). The three-dimensional structure of the adsorbed trypsin was preserved at the PPSU surface, supported by the small root-mean-square deviation of approximately 1.5 Å for each trypsin molecule during the simulation (**Fig. B.5**)[100]. This is in contrast with traditional hydrophobic surfaces where proteins were often found to spread and unfold upon hydrophobic binding (**Fig. 3.2e**)[84]. Furthermore, the six trypsin molecules were randomly oriented after anchoring (**Fig. 3.3c** and **Fig. B.6**). The non-specific orientation of trypsin allowed the exposure of their active sites for five out of the six molecules, demonstrating the retention of enzymatic activity even when shielding by further corona formation was taken into account[94]. Dipole relaxation of the PPSU backbone at all six PPSU-trypsin interfaces was confirmed by calculating the surface percentage of sulfone groups, revealing significantly enhanced surface hydrophobicity triggered

*This video can be accessed in `https://www.nature.com/articles/s41565-023-01584-z`

by trypsin adsorption (**Fig. 3.3d** and **Fig. B.7**). Simulations also showed that water lubricated the PPSU-trypsin contact regime via PPSU-water-trypsin hydrogen bonds (**Fig. 3.3a**, inset). Furthermore, the hydration of trypsin, described by the amount of trypsin-water hydrogen bonds and water neighbours, remained unchanged despite hydrophobic adsorption (**Fig. 3.3e**). This retention of protein hydration is an appealing feature for hydrophilic surfaces and essential for preserving the bioactivity of proteins[100]. Taken together, the simulation results suggest that the restructuring of the PPSU surface, rather than the denaturing of the adsorbed trypsin, led to controlled interfacial hydrophobic interactions for preserving the protein structure. It is noteworthy that similar results were reported by simulating the PPSU NP with immunoglobulin G (IgG) (**Fig. 3.6**) and bovine serum albumin (BSA) (**Fig. B.8**).

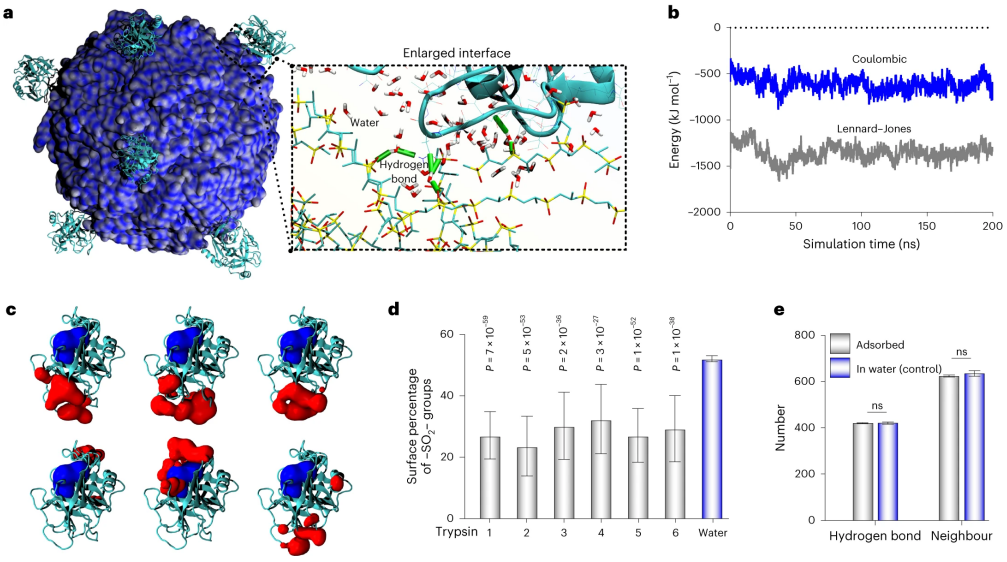

Figure 3.3: Atomistic explicit solvent simulations confirm the interfacial hydrophilic/hydrophobic transition within PPSU surface on trypsin adsorption. a, Simulation snapshot of an equilibrated 600-chain NP adsorbed with six adsorbed trypsin molecules (in cyan). The protein-NP interfaces are lubricated by water molecules, leading to the preserved structure of trypsin. The green cylinders refer to the water bridges connecting the PPSU chains and trypsin via hydrogen bonds. b, Lennard-Jones trypsin-NP interactions dominated over the trypsin-NP Coulombic interactions, supporting the hydrophobicity-driven feature of trypsin adsorption. c, Orientations of the six trypsin molecules are non-specific on adsorption. The adsorption sites and active sites on trypsin are coloured in red and blue, respectively. d, Percentage of sulfone groups at the trypsin-NP contact region, revealing enhanced NP surface hydrophobicity after trypsin adsorption. Significant P values relative to the water-NP interface are displayed on the graph. e, No significant (ns) differences in trypsin hydration were detected between the adsorbed trypsin and unbound trypsin. The numbers of trypsin-water hydrogen bonds and those of the water neighbours of trypsin were calculated. The data in d and e are presented as mean values±standard error. Statistical significance was determined by a two-sample t-test from 52 to 196 ns (calculated every two nanoseconds; n=73).

3.1.3 Irreversible adsorption of proteins enables the bioactivity of PPSU NPs

Having understood the distinct protein affinity of PPSU surfaces, we established a facile and versatile process for coating PPSU NPs with protein adlayers (**Fig. 3.4a**). In brief, PPSU NPs were incubated with excess proteins in PBS for 5 min at room temperature, followed by thorough wash-

ing to remove dynamically adsorbed proteins as well as residual proteins in solution. The saturation of adsorbed proteins on the NPs avoided aggregation in PBS (**Fig. B.9**). The obtained protein-coated NPs showed improved colloidal stability, with their zeta potential dependent on the adsorbed protein identity (**Fig. 3.4b**). Using BSA as a model protein, small-angle X-ray scattering (SAXS) measurements revealed that the shell thickness of NPs increased from 5.3 to 7.1 nm after adsorbing a protein coating (**Fig. 3.4c**). The BSA-coated NPs were imaged by transmission electron microscopy (TEM) and cryogenic scanning transmission electron microscopy (cryo-STEM), showing consistent sizes and morphologies with that of the pristine PPSU NPs (**Fig. B.10**). To probe the displacement of adsorbed proteins by competitive serum proteins, we coated PPSU NPs with fluorescein isothiocyanate (FITC)-tagged bovine serum albumin (FITC-BSA) and incubated the complex of FITC-BSA@NP in pooled human plasma at 37°C. Negligible FITC-BSA ($<$0.3%) was detected by fluorescence in the supernatants, and there were no significant differences for the 48-h-incubation and 0-h-incubation mixtures (**Fig. B.11**). The stable presentation of FITC-BSA at the PPSU surfaces was not contributed by the FITC labels, as FITC cannot be irreversibly adsorbed by PPSU NPs (**Fig. B.12**).

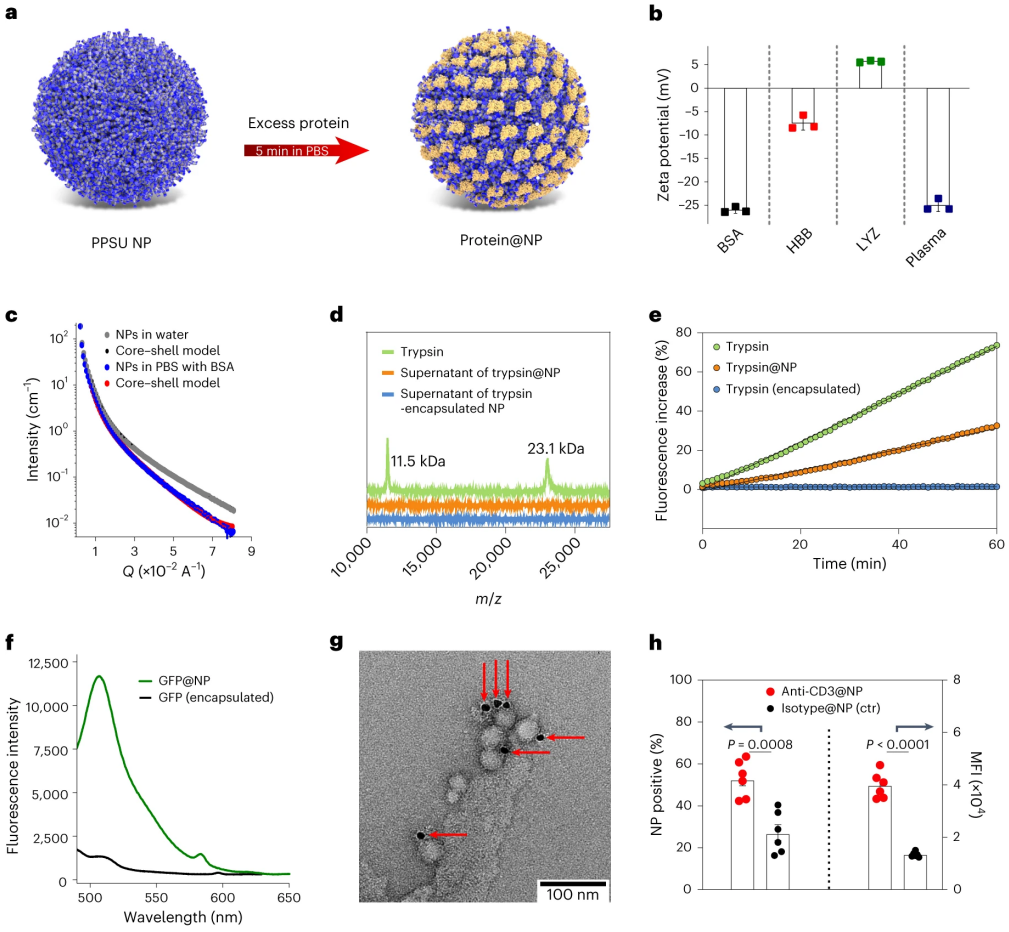

Figure 3.4: PPSU NPs preserve protein function within stable adlayers. a, Schematic of the rapid and facile process of coating PPSU NPs with protein adlayers. After incubation, the unbound proteins are removed by thorough washing. b, Zeta potential of protein-coated NPs is dependent on the adsorbed protein type. Data are presented as mean values ± standard error. The results were obtained from three parallel samples (n=3). c, SAXS data supporting the increase in shell thicknesses from 5.3 to 7.1 nm after BSA adsorption. d, Trypsin is stably adsorbed at the NP surfaces and free trypsin is undetectable by MALDI-TOF mass spectrometry in the supernatant after the centrifugation of trypsin@NP. Samples were stored at 4 °C for 48 h before centrifugation. e, Kinetic assay demonstrating the bioactivity of adsorbed trypsin. Trypsin is encapsulated within the NPs for comparison. f, Fluorescence of GFP was detectable for GFP@NP but not for GFP-encapsulated NPs. g, Immunogold labelling showing the binding of pre-adsorbed anti-CD4 antibodies to secondary antibodies. Here 10 nm colloidal gold-secondary antibody is indicated by the arrows. h, Targeting of irreversibly adsorbed anti-CD3 towards Jurkat T cells is confirmed by flow cytometry as assessed by the percentage of NP-positive cells and median fluorescence intensity (MFI). Data were obtained from six parallel experiments (n = 6) and are presented as mean values ± standard error. Significant P values are displayed on the graph. Statistical significance was determined by a two-way analysis of variance with Tukey's multiple comparisons test.

We explored the effect of irreversible adsorption on protein bioactivity using various adsorbed proteins as models. Trypsin and green fluorescent protein (GFP) were coated onto PPSU NPs to form the complexes of trypsin@NP and GFP@NP, respectively. The stable surface presentation of adsorbed trypsin was demonstrated by matrix-assisted laser desorption ionization time-of-flight (MALDI-TOF) mass spectrometry (**Fig. 3.4d**). To assess the enzyme activity of trypsin@NP, we quantified the increase in fluorescence resulting from the proteolytic cleavage of quenched FITC-BSA solutions into FITC-labelled peptides (**Fig. B.13**). This assay confirmed the ability of trypsin@NP to cleave BSA (**Fig. 3.4e**). A fluorescence 'turn-on' assay was subsequently performed to investigate the trypsin activity of the proteolysis mixture, revealing less than 0.1% of trypsin desorption after the proteolysis of BSA (**Fig. B.14**). We previously reported that GFP had no detectable fluorescence after encapsulation within PPSU NPs, probably due to exposure to dimethyl sulfoxide (DMSO) during NP formation19. In contrast, the structure-dependent fluorescence of GFP was readily detectable for GFP@NP (**Fig. 3.4f**), verifying surface adsorption to be a reliable and facile process for loading proteins without exposure to denaturing organic solvents.
We next assessed the retention of antibody-binding affinity, using low mass ratios of antibodies to achieve near 100% adsorption efficiency. Given the incomplete surface coverage of the antibody-adsorbed NPs, BSA as a blocking agent was subsequently coated to avoid non-specific interactions with unoccupied regions on the NP surface. This two-step pre-adsorption protocol allows us to incorporate various and even multiple antibodies into protein adlayers with well-controlled composition (**Fig. B.15**). Staining anti-CD4/BSA@NP with secondary gold-coupled antibodies verified the surface presence as well as immunological recognition by the pre-adsorbed primary antibodies (**Fig. 3.4g** and **Fig. B.16**). Using CD3 as a cellular target, anti-CD3/BSA@NP significantly increased uptake into T cells compared with controls (**Fig. 3.4h** and **Fig. B.17**).

3.1.4 Optimizing the adsorption of multiple proteins for MC-targeted nanotherapies

MCs are tissue-based granulocytes involved in allergic and other responses and are historically difficult to selectively target with therapeutics[101,102,103]. Perhaps the most challenging barrier to develop selective therapies for MCs is the difficulty in identifying specific surface targets to mediate inhibitory signalling upon FcεRIα activation following allergen binding. Siglec-6 has been identified as such a target[104,105], but optimizing inhibitory Siglec-6 signalling during FcεRIα engagement has not been achieved. We hypothesized that the co-engagement of Siglec-6 with pre-adsorbed antibodies on PPSU NPs could be optimized to inhibit MC secretion for the prevention of anaphylaxis. To test this hypothesis, PPSU-based nanomedicines (**Fig. 3.5a**) that consist of co-adsorbed anti-Siglec-6 (MC inhibiting) and anti-FcεRIα (MC activating) antibodies were prepared with a controlled surface density of anti-Siglec-6 antibodies. We confirmed the bioactivity of pre-adsorbed anti-FcεRIα antibodies to bind and activate primary human skin MCs in vitro (**Fig. B.18**). Importantly, inhibited secretion was observed when the nanomedicines were administered (**Fig. 3.5b-e** and **Fig. B.19**). This result suggested co-localized Siglec-6 engagement to inhibit the FcεRI-mediated activation of primary human skin MCs (**Fig. 3.5c**).

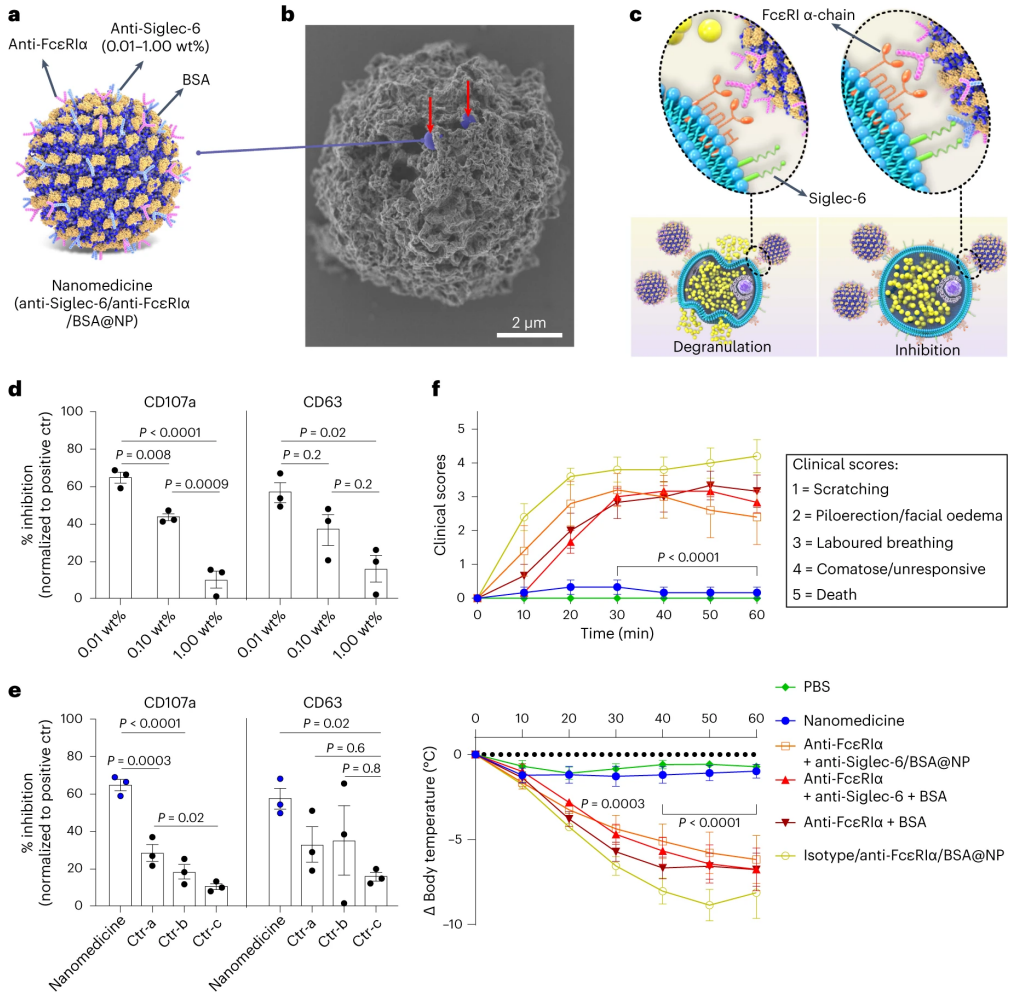

Figure 3.5: Optimization of a nanotherapy to inhibit anaphylaxis in a humanized mouse engraftment model. a) PPSU-based nanomedicines consisting of co-adsorbed anti-Siglec-6 (light blue), anti-FcεRIα (pink) and BSA (blocking agent, yellow) with a controlled surface density (as wt% of PPSU) of anti-Siglec-6. b) Imaging the nanomedicines (blue, indicated by the red arrows) on the surface of an MC (grey) by SEM. c) Activation of MCs (left) is achieved via the cross-linking of FcεRIα by anti-FcεRIα/BSA@NP, whereas the nanomedicine inhibits MC degranulation (right) via co-localized engagement of FcεRIα and Siglec-6. d) Optimizing the nanomedicine formulation by adjusting the surface density of anti-Siglec-6. e) In vitro results demonstrating the importance of binding Siglec-6 in close proximity and time with engagement of FcεRI in suppressing CD107a and CD63 expression by MCs. ctr-a: anti-Siglec-6/BSA@NP + anti-FcεRIα; ctr-b, anti-Siglec-6 + anti-FcεRIα + BSA; ctr-c, BSA@NP + anti-FcεRIα. In d) and e), inhibition is normalized from MCs receiving only anti-FcεRIα and expressing a positive population mean of 52.7±5.0% for CD63 and 71.2±8.0% for CD107a. f) The in vivo optimized nanomedicine (2.5 wt% of anti-Siglec-6) was highly effective as an allergen immunotherapy without triggering anaphylaxis in a humanized mouse model. Each mouse sample was only measured once. Statistical significance was determined by one-way analysis of variance (ANOVA) in d) and e), and by two-way ANOVA in f), both with a Tukey's post hoc test. All data are represented as mean values±standard error.

Cell surface markers (CD107a and CD63) for MC degranulation were quantified via flow cytometry to assess the extent of MC activation (**Fig. 3.7**). The experiments showed that lower densities of anti-Siglec-6 on the NP surfaces resulted in greater receptor engagement and inhibition (**Fig. 3.5d**). The treatment was further evaluated and compared with a variety of controls, including a mixture of free-form anti-FcεRIα with anti-Siglec-6/BSA@NP to assess the ability of a nanotherapy to inhibit pre- or co-activated MCs. The data indicated that the localized co-engagement of both Siglec-6 with FcεRIα is necessary to achieve a significant reduction in degranulation ($>$60%; $P < 0.001$), which was compared with control formulations where anti-FcεRIα was delivered without being co-adsorbed or without anti-Siglec-6 (**Fig. 3.5e**). In particular, these in vitro data demonstrated the need for both antibodies to be simultaneously present on the NP surfaces.

For in vivo validation, we tested the optimized nanomedicine formulation in a humanized MC mouse model by intravenous injection (**Fig. B.20**). In this model, anaphylaxis was induced by utilizing anti-FcεRIα antibody to cross-link FcεRI and trigger MC degranulation. In preparation for these experiments, we conducted a small pilot study of anti-Siglec-6 density (1.0, 2.5 and 10.0 wt%) on the surface of PPSU. We found that the requirements for in vivo inhibition appeared to be less stringent than those observed in vitro, as each group displayed comparable inhibitory activity. We conservatively selected 2.5 wt% since it worked well and probably better mirrored the in vivo MC receptor density; we previously observed that primary MCs can lose Siglec-6 density when cultured in vitro28.

Anaphylactic reactions were measured by monitoring the changes in body temperature using a digital rectal thermometer and a clinical scoring system (**Fig. 3.5f**)[106]. Mice that experienced anaphylaxis had significantly greater drops in body temperature and increased clinical scores (ΔT $>$ 5 °C; clinical scores, $>$ 2,; $P < 0.001$). The successful inhibition of anaphylaxis was manifested by responses that were statistically indistinguishable from the PBS negative control (ΔT

$\leq$ 1°C; clinical score, <0.5). Mice treated with the nanomedicine displayed a near-complete inhibition of anaphylaxis, whereas other formulations that did not have antibodies co-adsorbed or were freely solubilized did not display any significant inhibition of anaphylaxis. These findings confirmed our in vitro data, which suggested that co-engagement is necessary for the optimal inhibition of anaphylaxis (**Fig. 3.5e**). This is probably due to the spatiotemporal requirements of Siglec-6 signalling in optimal proximity to FcεRI during FcεRI-mediated activation. We and other groups have demonstrated that engaging Siglecs and other receptors containing an immunoreceptor tyrosine-based inhibitory motif (Siglec-6 included) recruits phosphatases SHP-1/SHP-2 and SHIP, which—in turn—dephosphorylate and disrupt the tyrosine kinase activity resulting from FcεRI signalling[91,107,108,92,109,110].

Although it is possible to achieve co-engagement by flooding in vitro assays with both antibodies in a soluble form to achieve inhibition, it is much more difficult to achieve this in vivo without administering impractically high concentrations of antibodies to ensure that both receptors are engaged simultaneously. By utilizing PPSU NPs as a platform to unite both antibodies in proximity, we can maximize the co-localization of both signals and achieve the data shown in **Fig. 3.5f**. We also tested a model for inhibiting IgE-mediated allergy (**Fig. B.20**); in this case, we utilized 4-hydroxy-3-nitrophenylacetyl (HN) hapten-conjugated bovine serum albumin (nBSA) to simulate allergic sensitivity to a hapten molecule[106,111]. The resulting data (**Fig. 3.8**) mirrored the findings of the above experiment, which utilized anti-FcεRIα. In terms of therapeutic strategies, it is probable that anti-FcεRIα or a similar broad-targeted antibody or protein holds greater merit for clinical development, as seeking regulatory approvals for individual allergens would be incredibly cost and time prohibitive.

3.1.5 Conclusions

Using a combination of in silico, in vitro and in vivo methods, as well as a simple mixing protocol, we demonstrate the controlled, irreversible adsorption of multiple proteins simultaneously to PPSU NP surfaces while preserving protein function. Highly dynamic PPSU surfaces were capable of site-to-site hydrophilic/hydrophobic switching in the presence of adsorbing protein, which allowed the facile binding of bioactive enzyme and antibody combinations. This design freedom provided the flexibility to create and optimize a nanotherapy for acute anaphylaxis, achieving the targeted inhibition of FcεRI receptor activation on human MCs via Siglec-6 signalling. Our work validates PPSU as a robust platform for the facile engineering of bioactive NPs and allows the customization of the complex and combinatorial capabilities of biologics in the treatment of disease.

3.1.6 Methods

Preparation of PPSU NPs

PPSU was synthesized as described in our previous report[97]. The self-assembly of PPSU was performed via stepwise hydration using a confined impingement jet mixer. Typically, 15 mL of PPSU solution (25 mg mL^{-1} in DMSO) and 15 mL of water were impinged against one another within the mixer by syringe injection. This process was repeated once more using 15 mL of water and the 30 mL of suspension obtained from the prior impingement. After the two-step hydration, 45 mL of the suspension was collected, followed by dialysis in water (3 days) to remove DMSO. As prepared, the NPs (suspended in water) were stored at room temperature before use.

Cryo-STEM

Lacey carbon grids (200 mesh, Electron Microscopy Sciences) were treated for 20 s in a Pelco easiGlow glow discharger (15 mA, 0.24 mbar). Each sample (4 μL) was pipetted onto a grid and plunge frozen into liquid ethane using an FEI Vitrobot Mark IV cryo-plunge freezing robot

with a blotting time of 5.0 or 5.5 s and a blotting pressure of 1. The frozen grids were stored in liquid nitrogen and then loaded into a Gatan 626.5 cryo-transfer holder cooled down to -180 °C before imaging in a Hitachi HD2300 STEM instrument at 200 kV. The frozen samples were pre-viewed with phase-contrast transmission electron (TE) and high-angle annular dark-field detectors to verify sample preparation. With the sample still in the microscope, the cryo-holder was slowly warmed up to -95 °C over the course of 30 min to sublime away ice within the vacuum. Imaging in the microscope continued using a secondary electron (SE) detector in the STEM instrument to image the surfaces of NPs. The image data were collected with a Gatan digital micrograph and a DigiScan system. Any further image processing conducted on the aligned frames was completed in ImageJ (v.1.53e) software.

AAMD simulations

All simulations were performed with GROMACS 2021.5[26], a molecular dynamics package designed primarily for the simulations of large biomolecules. The CHARMM 36 m force field[27] was used for the AAMD simulations, which has been validated in our prior work[97]. The recommended CHARMM TIP3P water model was applied with the structures constrained using the SETTLE algorithm[28]. All visual analyses were performed with the VMD software[29]. In all simulations, the degree of polymerization of 20 was employed for the polymer chains, the same as that for PPSU20 in the experiments.

Preparation of protein@NP complex via protein adsorption

With the exception of antibodies, excess protein was used to achieve full adlayer coverage on NP surfaces. The following steps were employed: (1) NPs (5 mg mL^{-1}) were suspended in a protein solution (10 mg mL^{-1} in PBS) for 5 min; (2) solutions were then centrifuged and the NP pellet was collected; (3) the pellet was resuspended in PBS, followed by centrifugation. Step (3) was repeated for a total of three times to remove any unbound proteins. The final protein@NP complex

was suspended in PBS.

Encapsulation experiments

Rhodamine B was encapsulated during the formation of PPSU NPs. Here, 200 μL of PPSU solution (25 mg mL^{-1} in DMSO) was thoroughly mixed with 200 μL of an aqueous solution of rhodamine B (0.01 mg mL^{-1});then, 200 μL of water was added and thoroughly mixed. The mixture (600 μL) was dialysed in water for 3 days to completely remove DMSO and free rhodamine B. The encapsulation efficiency of rhodamine B is nearly 100% by fluorescence measurements. Trypsin was encapsulated using an overloading method. Then, 200 μL of PPSU solution (25 mg mL^{-1} in DMSO) was thoroughly mixed with 200 μL of an aqueous solution of trypsin (20 mg mL^{-1}); subsequently, another 200 μL of the trypsin aqueous solution was added and thoroughly mixed. After the additionof 1.4 mL of water, the mixture (2.0 mL) was centrifuged, and the pellet was resuspended in water. The water washing steps were repeated for a total of three times. All the supernatant was collected to quantify the free trypsin using an ultraviolet spectroscopic analysis technique (SpectraMax M5, SoftMax Pro v. 6.3 software), showing a saturation encapsulation/adsorption of 0.96 mg of trypsin per 1.00 mg of NPs.

Trypsin proteolysis fluorescence-based kinetic assay

Here 2 μg mL^{-1} of trypsin (free protease or nanoparticulate form) was incubated with 1 mg mL^{-1} of quenched FITC-BSA substrate at 37 °C. Trypsin cleaves and yields FITC-labelled peptides derived from the full-length protein, which releases the fluorophore from a quenched state and results in an increase in fluorescence. Proteolysis was, therefore, monitored by measuring the increase in fluorescence over a 1.5 h period (one measurement per minute). The measurements were obtained in three replicates per condition.

SAXS measurements

SAXS measurements were performed at the DuPont, Northwestern, Dow Collaborative Access

Team beamline at Argonne National Laboratory's Advanced Photon Source with 10 keV (wavelength, $\lambda = 1.24$ Å) collimated X-rays. All the samples (5 mg mL^{-1}) were analysed in the q range (0.001-0.500 Å^{-1}), with a sample-to-detector distance of approximately 8.5 m and an exposure time of 5 s. The beamline was calibrated using silver behenate and gold-coated silicon grating with 7,200 lines mm-1. The momentum transfer vector q is defined as $q = 4\pi \sin\theta\lambda^{-1}$, where 2θ is the scattering angle. Data reduction and buffer subtraction were performed using the IRENA 2.71 package within IGOR PRO 9 software (WaveMetrics). Model fitting was completed using SasView 5.0.5 software package where the core-shell sphere model was utilized to fit and analyse the data.

MALDI-TOF mass spectrometry detection of trypsin

Trypsin (5 wt%) was encapsulated or adsorbed by PPSU NPs. As prepared, the samples were stored for 48 h at 4 °C to permit the leakage of weakly associated trypsin (if present). The samples were pelleted by centrifugation at 20,000g for 10 min at room temperature. The supernatants were collected and were mixed (in a ratio of 1:1) with sinapinic acid matrix prepared in ultrapure water along with 0.2% trifluoroacetic acid. Trypsin prepared at 2 μg mL^{-1} was used as a positive control for detecting the full-length protein. The supernatant collected from PPSU NPs prepared in the absence of protein was used as a negative control. These mixtures were spotted on a stainless steel MALDI disc (Bruker), and full-length trypsin protein (23 kDa) was detected by MALDI-TOF mass spectrometry. The positive-ion mass spectra were collected on a Bruker rapifleX MALDI Tissuetyper operating in the linear time-of-flight mode. The spectra were obtained in triplicate.

Immunogold labelling

Samples were prepared by mixing 90 μL of PPSU NPs (1.0 mg mL^{-1} in water), 10 μL of anti-CD4 antibodies (0.5 or 0 mg mL^{-1} in PBS), 10 μL of 10× PBS and 100 μL of BSA (1.0 mg mL^{-1} in PBS). After incubation for 5 min at 4 °C, the samples were centrifuged, and the collected pellets

were resuspended in PBS. This step was repeated for a total of three times to remove the unbound protein molecules. Then, 20 μL of secondary gold-coupled antibodies (with 1 wt% of BSA in PBS) was added into each of the samples and the mixtures were dialysed in water to remove the salts. Negatively stained grids were prepared using 0.5 mg mL^{-1} of NPs water and then visualized on a JOEL 1400 TEM instrument operating at 120 kV.

Cellular uptake studies

Rhodamine B-encapsulated NPs were mixed with 5 wt% of anti-CD3 antibodies (or isotype control at 10 μg mL^{-1}) in PBS for 5 min and then suspended in PBS with 10 mg mL^{-1} of BSA. The unbound proteinsand any leaked rhodamine B were removed by washing with PBS. The antibody-adsorbed NPs (25 μg mL^{-1}) were incubated with Jurkat T cells for 30 min at 37 °C. The cells were analysed using a BD Fortessa flow cytometer. The cellular uptake was measured as a percentage of NP-positive cells and median fluorescence intensity.

Preparation of formulations for anti-Fc εRI α-mediated in vitroand in vivo validation experiments

Stocks of antibody-adsorbed NPs were prepared by concurrently incubating PPSU NPs with set concentrations of anti-Fc εRI α (0.1 wt% for in vitro or 0.2 wt% for in vivo) and variable amounts of anti-Siglec-6 to create NPs for co-engagement. Anti-Siglec-6 concentrations for in vitro experiments were determined by loading different weight percentages of the total PPSU mass present in each sample (0.01, 0.10 and 1.00 wt%), which translated to final well concentrations of 8, 80 and 800 ng mL^{-1}, respectively. In mouse experiments, we utilized 2.5 wt% anti-Siglec-6 (5 μg per injection). When preparing PPSU NPs with multiple antibodies, the protein was added to a microtube in the desired ratios and concentrations before the addition of PPSU NPs. After the incubation of antibodies for 5 min, the NPs were incubated with excess BSA before final washes to remove any unbound protein.

Preparation of formulations for IgE-mediated in vitro and in vivo validation experiments

Stocks of PPSU NPs for in vivo experiments composed of anti-Siglec-6 antibody and/or nBSA were prepared by sequentially incubating PPSU NPs (100 μg) with set concentrations of (1) anti-Siglec-6 (10 wt%) for 10 min followed by (2) nBSA (200 μg). Before injection, nBSA was quantified by measuring the sample eluents on a NanoDrop ultraviolet-visible spectrometer (NanoDrop 1000 and 2000 software) at 430 nm and adjusting to a final dose of 100 μg per mouse. In vitro samples were prepared in the same manner, with different concentrations of reagents to better fit the cell culture conditions. For this, we incubated PPSU NPs with 0.25 wt% of nBSA and a range of anti-Siglec-6 concentrations (10.00, 1.00 and 0.10 wt%). The samples were formulated to achieve a final concentration of 100 ng mL^{-1} nBSA. All the in vivo and in vitro samples were prepared, washed and suspended in 1× PBS before use.

MC isolation and cell culture

Skin-derived primary mast cells (SkMCs) were isolated from 100 cm2 human skin samples received from the Midwestern Division of the Cooperative Human Tissue Network. Multiple donors were used across our experiments to ensure consistency despite patient variability. The samples were de-identified and therefore not required to supply informed consent or subject to review by Northwestern's Institutional Review Board. We utilized a protocol developed elsewhere[112]; in brief, we cut the skin into less than 1 cm2 pieces and then subjected the tissue to a digestive enzyme wash at 37 °C for 1 h, completing three rounds of wash. After this, the cells were pelleted under centrifugation and further purified by collecting a buffy coat over Percoll. Cells were then purified (>95%) via passive media selection in culture for eight weeks before use in experiments.

SEM

The medium was removed after cell incubation, and glutaraldehyde solution (2.5%) was added for fixation overnight at 4 °C. The cells were then rinsed three times with 0.1 M of sodium cacodylate

buffer and once with water (5 min) and incubated in osmium tetroxide (2%) for 1 h. After staining, the cells were rinsed another three times with water (10 min per time). The cells were dehydrated with a series of ethanol gradients (30%, 50%, 70%, 85% and 95%) for 10 min at each step. The dehydrated cells were rinsed with 100% ethanol two times (10 min per time) and were completely dried using SAMDRI-795 (tousimis) critical point dryers. After drying, the cells were placed on a carbon tape attached to an aluminium stud and coated with an SPF osmium coater (10 nm thickness) for scanning electron microscopy (SEM) analysis. The morphology was then observed by a Hitachi SU8030 scanning electron microscope. Three biologically independent sets of samples were generated for imaging.

Analysis of degranulation markers with flow cytometry

In preparation for the experiments, we used dose curves to optimize the concentration of anti-Fc εRI α required to induce a clear expression of degranulation markers on SkMCs above the baseline levels (80 ng mL^{-1}). Additionally, we incubated the cells with 10 ng mL^{-1} of polyclonal human IgE (Abcam) O/N to stimulate Fc εRI expression and prime the cells for activation. For the experiment, SkMCs were resuspended in ice-cold Tyrode's buffer at 300,000 cells per sample and given a variety of experimental formulations containing PPSU NPs, free or antibody-adsorbed NPs, or a combination of each. Mouse IgG2a-isotype antibody (BioLegend clone MG2a-53) was used as a control comparison for anti-Siglec-6. Cells were placed in a 37 °C incubator for 20 min before being placed immediately back on ice to halt ongoing degranulation. Cells were then washed with PBS and suspended with live/dead fixable blue dead cell stain for 30 min at 4 °C. Subsequently, the cells were washed with FACS buffer (PBS with 3-4% FBS) and resuspended with a mixture of anti-human and anti-mouse Fc blocking buffer (BD Pharmingen) for 10 min and then a 50 μL of a master mix containing all the antibody labels was directly added (each antibody administered at a ratio of 5 μL of stock per one million cells) to incubate for 45 min at 4 °C. Fluorescence minus-one

controls were stained using the same method. At last, the cells were washed two times with the FACS buffer or fixed with 4% paraformaldehyde and then washed with more FACS buffer. All of the flow sample data were collected on a BD FACSymphony A5 instrument and simultaneously compensated using the equipped FACSDiva software. Antibodies: BV421-labelled anti-CD117 (KIT) (clone 104D2 from BioLegend; lot B369859). PE-labelled anti-Siglec-6 (clone 767329 from R&D Systems; lot ADZQ0221091), BV650-labelled anti-CD63 (clone H5C6, from BioLegend; lot B356296), APC-labelled anti-CD107a (lamp1) (clone H4A3, from BD Biosciences; lot 1264705) and FITC-labelled anti-Fc εRI α (clone AER-37, from BioLegend; lot B323076). Unlabelled antibodies used are anti-Siglec-6 (clone 767329 from R&D Systems; lot CIIM0221111), anti-Fc εRI α (clone AER-37 from Invitrogen; lot 2011282) and mouse IgG2a-isotype control (from Invitrogen; lot UF285470). The samples were analysed on FlowJo software v. 10. All the samples were gated for singlets followed by live/dead and normal KIT expression before analysing other markers. Additionally, the samples were gated to a minimum of 15,000 KIT+ cells. The experiments were conducted using cells derived from three different donors for these experiments, totalling n = 3 for each group.

Cytokine expression analysis via enzyme-linked immunosorbent assay

Human TNF- α (cat. no. QTA00C) enzyme-linked immunosorbent assay kits were obtained from R&D Systems. 100,000 SkMCs cells per well (n = 2 from two tissue donors for a total of n = 4) were incubated with formulations for 3 h. The supernatant was then collected and stored overnight at -20 °C before being used in kits as prescribed in their protocols. The same conditions were utilized for our other in vitro experiments. Here we dosed cells with 0.1 wt% anti-Siglec-6 (80 ng mL^{-1}) on PPSU NPs, with a final well concentration of 80 μg mL^{-1} of PPSU NPs (8 μg per sample). Similar to the flow cytometry samples, anti-Fc εRI α was adsorbed onto PPSU NPs or separately dosedat 80 ng mL^{-1}.

Humanized mouse engraftment and anaphylaxis model

We utilized a previously established and characterized model to test the inhibitory effects of our formulations in vivo[106]. Four-week-old NSG-SGM3 mice were retro-orbitally injected with hCD34+ stem cells. After 16 weeks, the mice were checked for engraftment using flow cytometry. We used FITC-labelled anti-hCD45 clone 2D1 (BioLegend) and APC/Cy7-labelled anti-mCD45 clone 103116 (BioLegend) to compare the human and mouse cell populations. Successfully engrafted mice (>5% hCD45+) were then randomized with respect to the percentage of engraftment and retro-orbitally injected with test formulations. Nanoparticulate-free anti-Fc εRI α antibody (1 μg mL^{-1}) was used as a positive control to compare the mice given the nanomedicine and the other test formulations. Visual clinical scoring and a rectal temperature probe were used to track the anaphylactic reaction severity for 1 h post-injection, with the data collected at 10 min intervals. The clinicalscores were determined as follows: 1, scratching; 2, piloerection/facialoedema; 3, laboured breathing; 4, comatose/unresponsive; 5, death. The mice were then killed and not reused.

Humanized mouse model of IgE-mediated anaphylaxis

For this work, 13-to-18-week-old NSG-SGM3 mice pre-engrafted with hCD34+ stem cells were acquired from the Jackson Laboratory. This experiment directly adapts previous methods that utilized engrafted NSG-SGM3 mice[106,113,114,115]. Each mouse was given a single retro-orbital intravenous injection of 1.6 μg IgE (produced by the cell line JW8/5/13 (Sigma-Aldrich) and kindly provided by Allakos) in 100 μL of PBS to sensitize them to the HN hapten. The following day (18-24 h later), the mice were injected with experimental or control reagents in 100 μL of PBS. The reagents were formulated as previously described; in brief: PPSU NPs (100 μg) were incubated with anti-Siglec-6 (10 μg; R&D Systems clone 767329) and an excess of nBSA (200 μg; 8 HN units per nBSA; Biosearch Technologies) or PPSU NPs were incubated with nBSA (no anti-Siglec-6) using the same amounts. Anti-Siglec-6 was mixed with NPs 20 min before nBSA to

reduce competition and ensure a consistent adsorption of the antibody. We utilized 100 μg of solubilized nBSA in PBS as a positive control and a PBS vehicle control. In the particle samples, eluent nBSA concentrations were measured on a NanoDrop ultraviolet-visible spectrometer (NanoDrop 1000 software) at the absorption peak of HN (430 nm) and the concentrations were adjusted to a final dose of 100 μg of nBSA in 100 μL per mouse. Mouse temperatures and clinical scores were measured as previously noted in the anti-Fc εRI α anaphylaxis model.

Biological statistical analyses

Initial data visualization and final statistical analyses were conducted using GraphPad Prism (v.9.5.0) software. Final vector representations of the analysed data were created using Inkscape.

Animal care and use

All of the experiments conducted in vivo were performed and supervised in accordance with the animal protocols approved by the Institutional Animal Care and Use Committee at Northwestern University. Animal work was completed under the approved Institutional Animal Care and Use Committee study #IS00017606. Engrafted NSG-SGM3 mice were housed in high-level barrier facilities for immunocompromised animals and given the prophylactic administration of sulfamethoxazole/trimethoprim (Bactrim), as advised by Northwestern's Center for Comparative Medicine. The housing facility was maintained at a dry-bulb temperature of 20-26 °C, humidity between 30% and 70% and illuminated from 6 a.m. to 6 p.m.

3.1.7 Extended Data

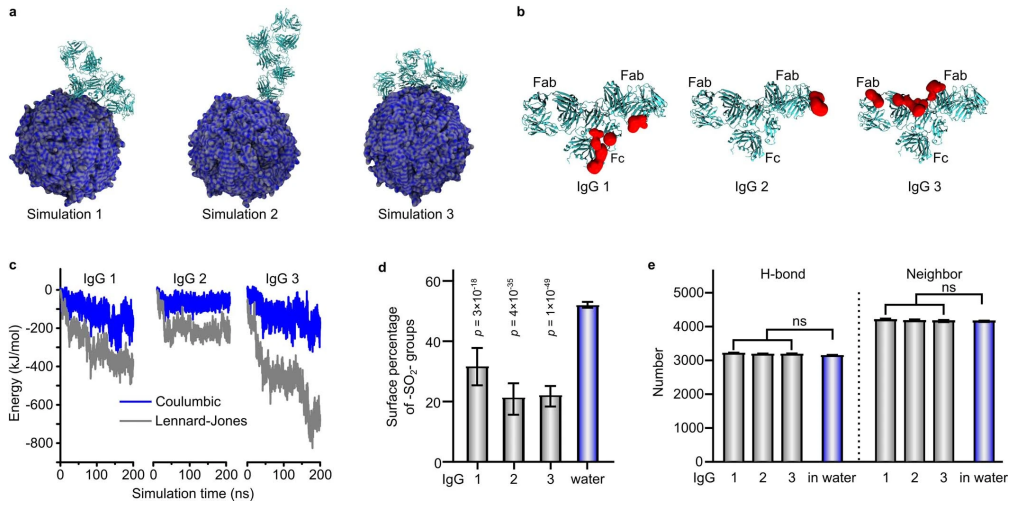

Figure 3.6: (a) Atomistic simulation snapshots showing the adsorption of IgG (cyan) onto the surface of the 600-chain NP in three parallel simulations. Only one IgG molecule can be simulated in each system due to the limit set by space constraints. (b) Orientations of the 3 IgG molecules in the three parallel simulations are non-specific upon adsorption. The adsorption sites are colored red. (c) The Lennard-Jones IgG-NP interactions dominated over the IgG-NP Coulombic interactions, supporting the hydrophobicity-driven feature of IgG adsorption. (d) Percentage of sulfone groups at the IgG-NP contact region revealing enhanced NP surface hydrophobicity after IgG adsorption. Significant P values relative to water-NP interface are displayed on the graph. (e) No significant (ns) differences in IgG hydration were detected between the adsorbed IgG and unbound IgG. The numbers of IgG-water H-bonds and of water neighbors of IgG were calculated. The data in (d) and (e) are presented as mean values $\pm$ standard error. Statistical significance was determined by two-sample t-test from 52 ns to 196 ns (calculated every two nanoseconds; n = 73).

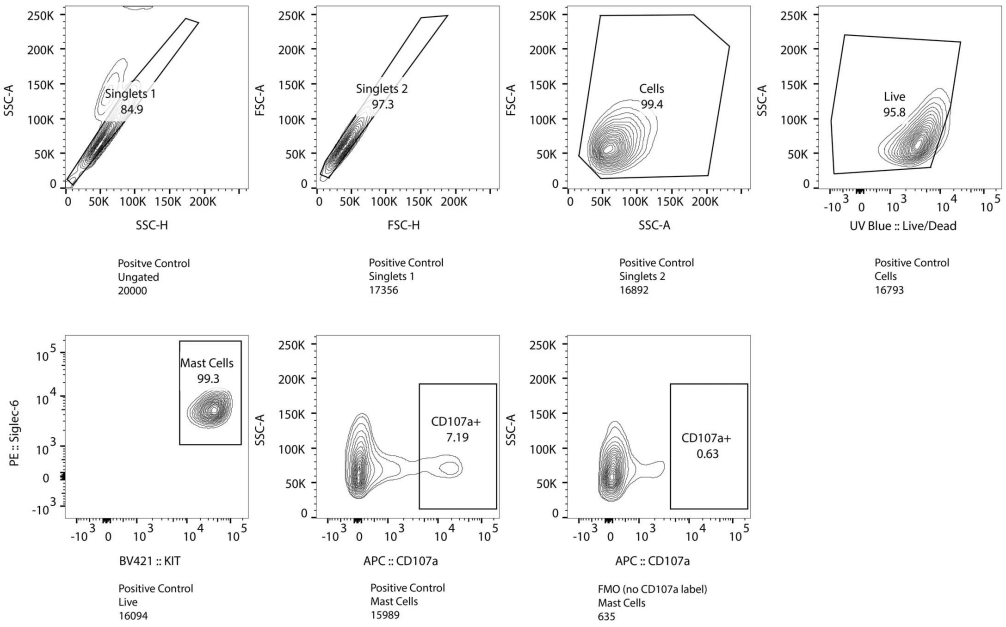

Figure 3.7: Primary human skin cell activation was analyzed by first gating singlets and live cells, followed by verification of mast cell-specific markers Siglec-6 and KIT receptor. This population was then analyzed for degranulation marker expression using the relevant antibodies. Here, we show the gating strategy for CD107a, along with an example of FMO control used to authenticate CD107a+ stained cells. This strategy was used for CD63, and CD107a flow cytometry data seen in **Fig. 3.5d, e** and **Fig. 3.8b**.

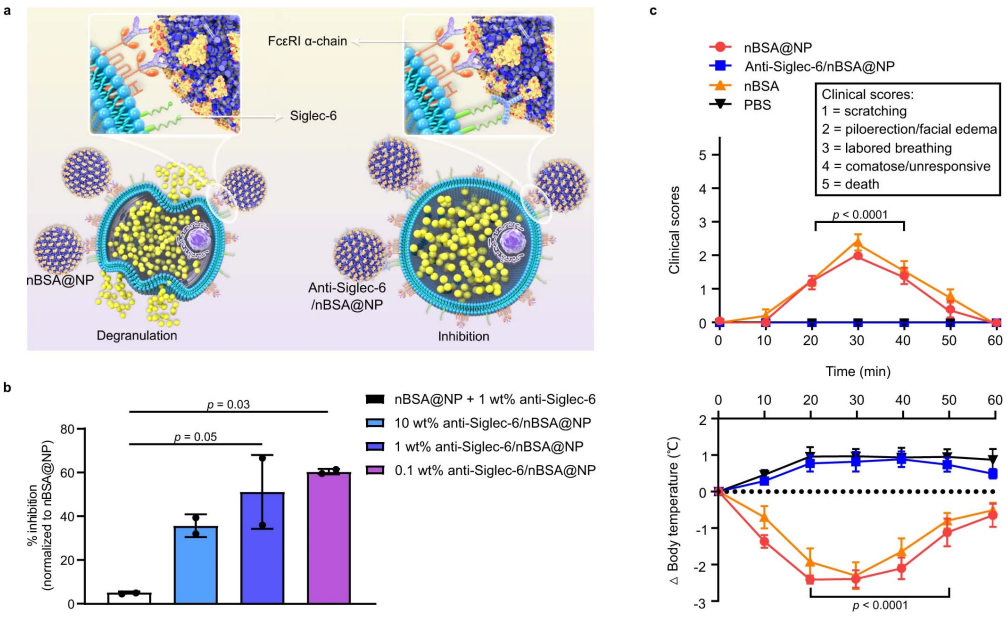

Figure 3.8: (a) Activation of mast cells (left) is achieved via cross-linking of FcεRIα (IgE-sensitized) by nBSA@NP, whereas anti-Siglec-6/nBSA@NP inhibits mast cell degranulation (right) via co-localized engagement. (b) Optimizing nanotherapy formulation via adjusting the surface density of anti-Siglec-6. Data are represented as mean values +/- standard error. Results were from two independent experiments (n = 2). Statistical significance was determined by one-way ANOVA with Tukey-post hoc test. (c) Humanized mice (n = 5 biologically independent animals combined from 2 independent experiments) were IgE-sensitized for the 4-hydroxy-3-nitrophenylacetyl hapten-BSA (nBSA) allergen followed by intravenous injections of formulations containing different combinations of PPSU NP, nBSA, and anti-Siglec-6. Mice injected with solubilized or NP-bound nBSA experienced a decrease of 2-2.5 °C in body temperature, indicating the onset of anaphylaxis. In contrast, the presence of anti-Siglec-6 in conjunction with nBSA on the surface of NPs resulted in inhibition of anaphylaxis. Data are represented as mean values +/- standard error. Statistical significance was determined by two-way ANOVA with Tukey-post hoc test.

3.2 Nonspecifically cross-linking hydrogel nanofibrils with proteins: from bioactive liquid droplets to thermally stabilized nanoenzymes

Authors: Fanfan Du, Yang Li, Simseok A. Yuk, Sultan Almunif, Baofu Qiao, and Evan A. Scott.
F.D. conceived this study and contributed all the data and wrote the manuscript. Y.L. carried out the simulations, analyzed the data and wrote the manuscript. S.A.Y. completed the SEM experiments. S.A. contributed to the SAXS measurements. B.Q. supervised the simulations and wrote the manuscript. E.A.S. supervised all the research and wrote the manuscript. This manuscript is in preparation.

Applications of proteins in harsh environments have been hampered by the potential of denaturation and a resulting loss of activity. The fragility of proteins stems from their hierarchical architectures that are subject to changes in organic solutions or at high temperatures. It has already been demonstrated that confinement originating from a synthetic support can thermally stabilize proteins[116,117,118,119,120]. Application of this strategy, however, has been hampered by the lack of general approaches to place diverse proteins in place within barely wider cavities. Specifically, cage inclusion requires appropriate pore sizes to accommodate a specific protein[121,122]; network encapsulation leaks proteins or limits protein accessibility[123,124]; metal-organic framework crystallization lacks sufficient mesoporous platforms[125,126].

Hydrophilic supports, including hydrogels formed by cross-linking either natural or synthetic polymers, are by far the primary materials being used to interface with proteins. Multipoint immobilization can be achieved for proteins with sufficient functionalizable groups or strong surface charges, but both require a tedious process of surface modifications to impart chemical coupling or ionic bonding[81,127]. Controlled surface adsorption has emerged to be promising in interfacing nonspecific proteins with synthetic components. The Xu group reported the rationally designed random heteropolymer capable of preserving protein function in organic solvent through robust surface coverage[99,128,129,130]. Our recently developed homopolymer poly(propylene sulfone)

(PPSU)[97] was also able to retain the bioactivities of pre-adsorbed proteins[131]. These results suggest the feasibility of using controlled but nonspecific adsorption of sol-gel precursors for restricting proteins within post-formed porous structures.

Here, we report on hydrogel nanofibrils capable of protein anchoring, forming liquid drops without compromising protein function and accessibility. Deswelling the liquid drops leads to the formation of confined proteins with improved solubility and stability in organic solvents. The hydrogel nanofibrils consist of poly(ethylene glycol)-b-poly(propylene sulfone) (PEG-PPSU) (**Fig. 3.9A**) block copolymers, which can bind to protein surfaces using propylene sulfone as the anchor. PEG was chosen to leverage its well-known ability to stabilize proteins as well as its solubility in water and organic solvents. The high protein affinity of PEG-PPSU was confirmed by explicit solvent all-atom molecular dynamics (MD) simulations. The simulations were performed on mixtures of PEG-PPSU molecules with a variety of proteins, including β-barrel green fluorescent protein (GFP), trypsin (TRP), and organophosphorus hydrolase (OPH), showing efficient adsorption of PEG-PPSU at the protein surfaces (**Fig. B.21** and **Fig. 3.9A**). Energy analysis revealed that the adsorption originates from the short-range van der Waals interactions between propylene sulfone units and amino acids, with the attraction strength of 3.2 typical hydrogen bonds (**Fig. B.22**). We were interested in the simulated polymeric framework around each protein, which would improve protein solubility and stability given the solubilization and confinement effects. Experimentally achieving this robust coverage is, however, challenging in water as the polymers aggregate before being adsorbed. Simulations suggested the formation of a PEG-PPSU superstructure even in the ultra-diluted aqueous solution of a single polymer chain (**Fig. B.23**).

3.2.1 Formation of protein-affinity hydrogel nanofibrils

We then considered protein stabilization by the adsorption of PEG-PPSU assemblies rather than the free molecules. To this end, PEG-PPSU was synthesized through the complete oxidation of poly(ethylene glycol)-b-poly(propylene sulfide) (PEG-PPS) by hydrogen peroxide (**Fig. B.24**). Remarkably, PEG-PPSU is highly "soluble" in water, with an apparent solubility of 110 g/L. This contrasts with the dissolution behavior of PPSU homopolymers, which cannot be directly suspended in water[97]. Despite the good water dispersity for PEG-PPSU, we found by cryogenic transmission electron microscopy (Cryo-TEM) the presentation of uniform nanofibrils in the aqueous system of PEG-PPSU (**Fig. 3.9B**). These nanofibrils are essentially hydrogels and the ice within nanofibrils contributed to the contrast during Cryo-TEM imaging (**Fig. B.25**). X-ray scattering demonstrated that PPSU was partially crystallized in the nanofibril structure (**Fig. 3.9C**). Small-angle X-ray scattering (SAXS) further confirmed the formation of cylinder structures. Importantly, the nanofibrils had an average diameter of 4.4 nm by Cryo-TEM (not including the corona) and 7.7 nm by SAXS. Artificial approaches to fabricate hydrogel nanofibrils with their diameters close to the size of proteins are unusual, which would allow us to anchor multiple nanofibers to the surface of a protein.

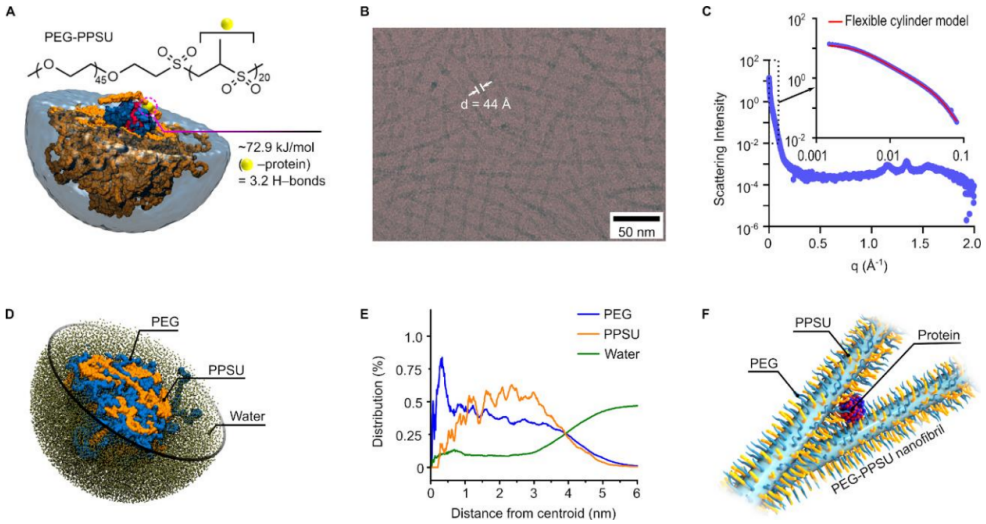

Figure 3.9: Hydrogel nanofibrils formed by PEG-PPSU with controlled protein affinity for maintaining protein function. (A) Computational studies suggest the feasibility of using propylene sulfone (highlighted by the yellow ball) as protein anchors. The simulations performed on the mixture of PEG-PPSU (orange; inset is the chemical structure) with proteins (hydrophobic patches, red; hydrophilic patches, blue) in water (cyan) led to the formation of a polymeric framework around each protein. The average binding energy between the repeating unit of PPSU and proteins is approximately 72.9 kJ/mol. (B) Cryo-TEM imaging shows the spontaneous formation of hydrogel nanofibrils by mixing PEG-PPSU with water. (C) X-ray scattering demonstrating crystallization of PPSU within the hydrogel nanofibrils. The inset shows the SAXS curve that fits the cylindrical model. (D) Atomistic simulation on PEG-PPSU in water yields a weak-phase separated structure, with the component distributions provided in (E). (F) The exposure of propylene sulfone units enables nanofibril cross-linking by the addition of proteins.

PPSU has a high affinity for a wide range of organic molecules[97], demonstrating a slightly higher hydrophobicity than PEG[131]. A weak phase separation between PEG and PPSU could be thus expected upon the formation of PEG-PPSU hydrogel nanofibrils. This was confirmed by atomistic simulation on PEG-PPSU assembly in water (**Fig. B.26**), showing that PPSU was not distinctly separated from PEG (**Fig. 3.9D,E**). In contrast, a control simulation on the PEG-PPS assembly supported a core-shell structure, wherein the hydrophobic PPS chains were completely shielded by the PEG corona (**Fig. B.27**). The simulations also showed the presence of water within

the PEG-PPSU assemblies, consistent with the characteristics of hydrogels. Therefore, PEG-PPSU assemblies, including the hydrogel nanofibrils, would preserve the protein affinity of PPSU despite the PEG coronas. In our design, mixing proteins with the hydrogel nanofibrils would lead to the formation of framework structures through the physical cross-linking (**Fig. 3.9F**).

3.2.2 Characterizations of bioactive liquid droplets

Using three model proteins with distinct isoelectric points (pI), including bovine serum albumin (BSA, pI 4.9), hemoglobin (HBB, pI 6.8), and lysozyme (LYZ, pI 11.35), we demonstrated by the phase transition the responsiveness of PEG-PPSU nanofibrils to nonspecific proteins (**Fig. B.28**). It should be mentioned that we did not observe nonspecific adsorption of proteins for the PEG-PPS nanostructures, regardless of the morphologies or sizes[132,133,134,135]. Transmittance of PEG-PPSU in aqueous solution was tracked as a function of BSA concentrations, showing that the nanofibril-protein complex can be liquefied by excess proteins (**Fig. 3.10A**). This result suggested the feasibility of changing the degree of cross-linking even after adsorption.

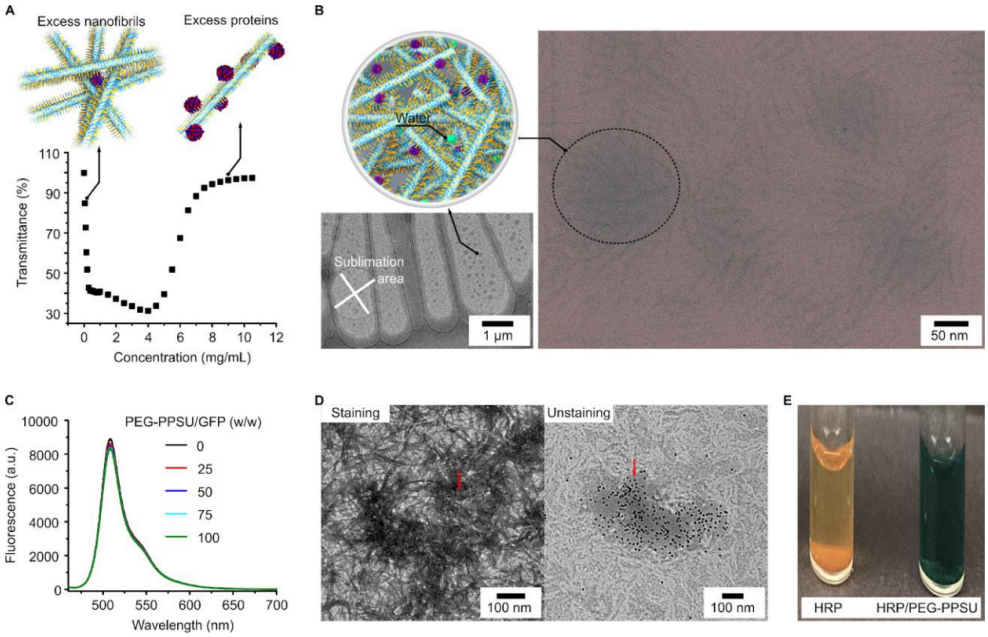

Figure 3.10: Physically cross-linking hydrogel nanofibrils with proteins leading to bioactive liquid droplets in aqueous solution. (A) Immediately tracking the transmittance of PEG-PPSU aqueous solution (1 mg/mL) upon the addition of BSA. Insets propose the structures formed before and after reaching the stoichiometric balance. (B) Cryo-TEM imaging showing the formation of liquid droplets (schematic) by mixing 1 wt.% of BSA with PEG-PPSU in PBS. In situ ice sublimation was performed to obtain the best contrast (**Fig. B.28**). (C) Fluorescence titration of GFP with PEG-PPSU in PBS. (D) Using 10 nm colloidal gold-antibodies (indicated by the red arrows) to locate the liquid droplets. TEM images were obtained for the aqueous suspension with and without staining the hydrogel nanofibrils by uranyl formate. (E) PEG-PPSU hydrogel nanofibrils (625 μg/mL) serve as surfactants for the elevated solubilization of HRP (12.5 μg/mL) intermediates in citric acid buffer (with TMB and H_2O_2 provided in the kit). The displayed color evolution (starting from colorless) confirmed the activity of HRP/PEG-PPSU. The orange precipitates indicated the presence of too much HRP.

While protein adsorption at the PPSU surface is irreversible[131], the use of PEG in the nanofibril structures effectively decreased the nanofibril-protein interactions to favor protein release on demand. The release of confined proteins from mesoporous materials and chemically cross-linked networks is typically challenging. Cryo-TEM imaging revealed a process of liquid-liquid phase

separation upon mixing nanofibrils to BSA, leading to the formation of liquid droplets (**Fig. 3.10B**) that are similar to membraneless organelles[136,137]. The liquid droplets were more visible but unable to show the fine structures at the low magnification. In situ ice sublimation was then performed to obtain the best contrast for the liquid drops at high magnification (**Fig. B.29**).

Fluorescence titration of GFP with PEG-PPSU showed that the adsorption of nanofibrils neither decreased the intensity nor shifted the emission peak in phosphate-buffered saline (PBS) (**Fig. 3.10C**). This result is not surprising as PPSU and hydrogels have demonstrated the ability to stabilize proteins[131,138]. When applied to the 10 nm colloidal gold-antibodies, adsorption of nanofibrils yielded a mixture of heterogeneously distributed nanofibrils (**Fig. 3.10D** and **Fig. B.30**). The TEM images also showed enriched but unaggregated colloidal gold nanoparticles in the droplets, indicating a near-homogeneous distribution of the antibodies within the liquid droplets. This solubilization strategy can be expanded to proteins with limited solubility. Taking horseradish peroxide (HRP) as an example, the adsorption of nanofibrils prevented the typical precipitation of HRP in 3,3′,5,5′-tetramethylbenzidine (TMB) substrate assay (**Fig. 3.10E**).

3.2.3 Effect of immobilization on protein function and accessibility

Having obtained evidence that bioactive liquid droplets form by mixing PEG-PPSU nanofibrils with proteins, we removed water by high vacuum from the systems to obtain immobilized proteins. The deswelling process yielded fluffy solids that demonstrated porous by the scanning electron microscopy (SEM) imaging (**Fig. 3.11A**). We observed the formation of spherical aggregates for GFP/PEG-PPSU, whereas a relatively regular network consisting of filamentous structures with much-enlarged diameters was formed by drying PEG-PPSU (**Fig. B.31**). These results

indicated that the addition of the proteins facilitated a hybridization event between nanofibrils. Interestingly, GFP/PEG-PPSU had undetectable fluorescence in the solid state, whereas solid GFP alone remained fluorescent (**Fig. B.32**). Because proteins need some flexibility to function, we resuspended the GFP/PEG-PPSU solids in PBS and found negligible loss of fluorescence after the deswelling-swelling cycle (**Fig. 3.11B**).

We further confirmed the preserved functions of proteins by applying the deswelling-swelling process to enzymes, such as TRP and OPH. Three typical substrates, including small molecules, proteins, and insoluble insecticides, were used to assess the enzymatic activities and accessibility. TRP digestions demonstrated that TRP/PEG-PPSU showed 100% native activity in the fluorometric assay of 7-amino-4-methylcoumarin (AMC) (**Fig. 3.11C** and **Fig. B.33**), and even higher activities were detected with the fluorescein isothiocyanate-tagged BSA (FITC-BSA) substrate (**Fig. 3.11D** and **Fig. B.34**). The well-known pesticide methyl parathion (MP) was chosen as the hydrophobic substrate for OPH/PEG-PPSU (**Fig. 3.11E**). Despite the excellent ability to degrade organophosphates, OPH showed inefficient hydrolytic activity in Tris-HCl due to the poor water solubility of the substrate. The presence of PEG-PPSU speeded up the degradation, resulting in a yellow solution due to the absorbance at 405 nm for the hydrolysate[99]. Co-solubilization of MP by the nanofibrils facilitated the reaction, as the nanostructure served as surfactants, able to promote the solubilization of hydrophobic molecules in aqueous environments (**Fig. B.35**).

Given the possibility of transporting and storing proteins without the use of a cold chain, we also investigated the thermal stability of GFP/PEG-PPSU and TRP/PEG-PPSU by aging the solids at 80 °C. In samples treated this way, we demonstrated improved thermal stability for TRP by using PEG-PPSU (**Fig. 3.11F** and **Fig. B.36**). However, negative effects of PEG-PPSU on the thermal stability were found for GFP, which became very thermosensitive in the presence of PEG-PPSU (**Fig. B.27**).

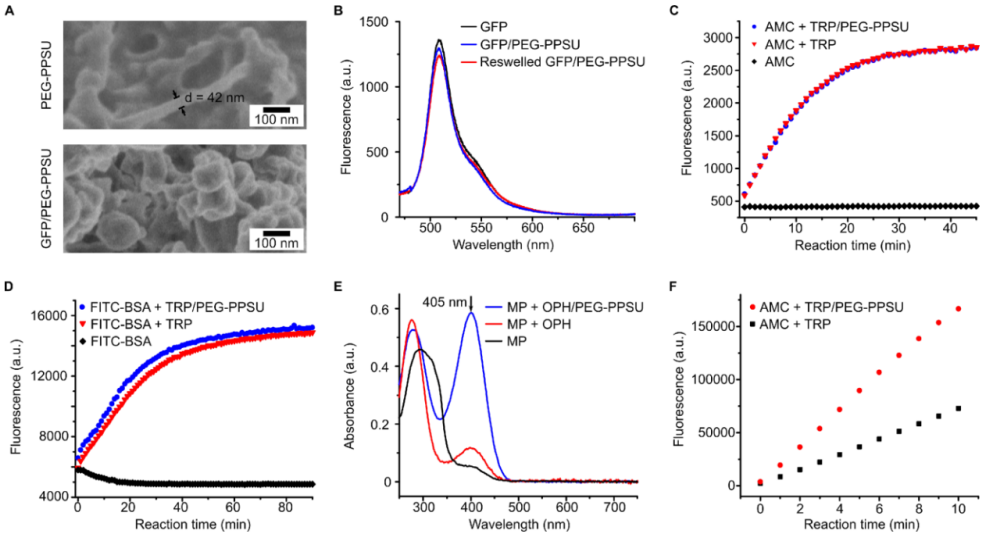

Figure 3.11: Removal of water from the liquid droplets gives immobilized proteins without compromising protein functions. (A) Removal of water from PEG-PPSU aqueous solutions (with/without GFP) leads to porous structures seen by SEM. (B) A deswelling-swelling process did not result in obvious fluorescence loss for GFP. Measurements were performed in PBS at 23 °C. (C) Using AMC as the small-molecule substrate to quantify the preserved activity of reswelled TRP/PEG-PPSU. (D) Using FITC-BSA as the protein substrate to quantify the preserved activity of reswelled TRP/PEG-PPSU. (E) The nanofibril-enabled MP solubilization in Tris-HCl promoted the degradation of the hydrophobic insecticide by OPH. (F) Improved thermal stability for dried TRP was achieved in the presence of PEG-PPSU. Activities were measured by the AMC assay after storing the TRP or TRP/PEG-PPSU solids at 80 °C for 3 hours.

3.2.4 Stabilized water-soluble proteins in organic media

We also utilized organic solvents such as toluene, chloroform, and tetrahydrofuran, to selectively dissolve PEG in the solids of GFP/PEG-PPSU. Percolation by the organic solvents allowed us to prepare fluorescent nanoparticles with good dispersity (**Fig. 3.12A** and **Fig. B.38**). Characteristic fluorescence was not detectable for GFP in these organic media. Interestingly, the fluorescence of GFP/PEG-PPSU in toluene was not completely quenched even stored at 80 °C over 24 hours (**Fig. 3.11B**). By contrast, GFP in water had no fluorescence after storing in water at 80 °C for 2

hours, regardless of the addition of PEG-PPSU (**Fig. B.39**). With the improved thermostability by PEG-PPSU, we were able to store GFP in toluene rather than in aqueous solutions at room temperature (23 °C) without significantly decreasing the fluorescence over 35 days (**Fig. B.40**).

Most native enzymes denature in solution at temperatures above 40 °C and require even low storage temperatures than that for GFP, typically below -20 °C. We quantified the activity of TRP/PEG-PPSU that experienced heat exposure in water and toluene (**Fig. B.41**). The results were consistent with that of GFP, showing that PEG-PPSU preserved 23% of native activity after storing TRP/PEG-PPSU in toluene at 80 °C for 5 hours (**Fig. 3.12C**). Complete loss of activity by the heat denaturation was found for TRP/PEG-PPSU in water, as was for TRP without PEG-PPSU in both solvents. In terms of the OPH/PEG-PPSU system, the preserved abilities to efficiently degrade MP in Tris-HCl were also confirmed after heating in toluene (**Fig. 3.12D**, and **Fig. B.42**). These results indicated the universality of PEG-PPSU in stabilizing other proteins.

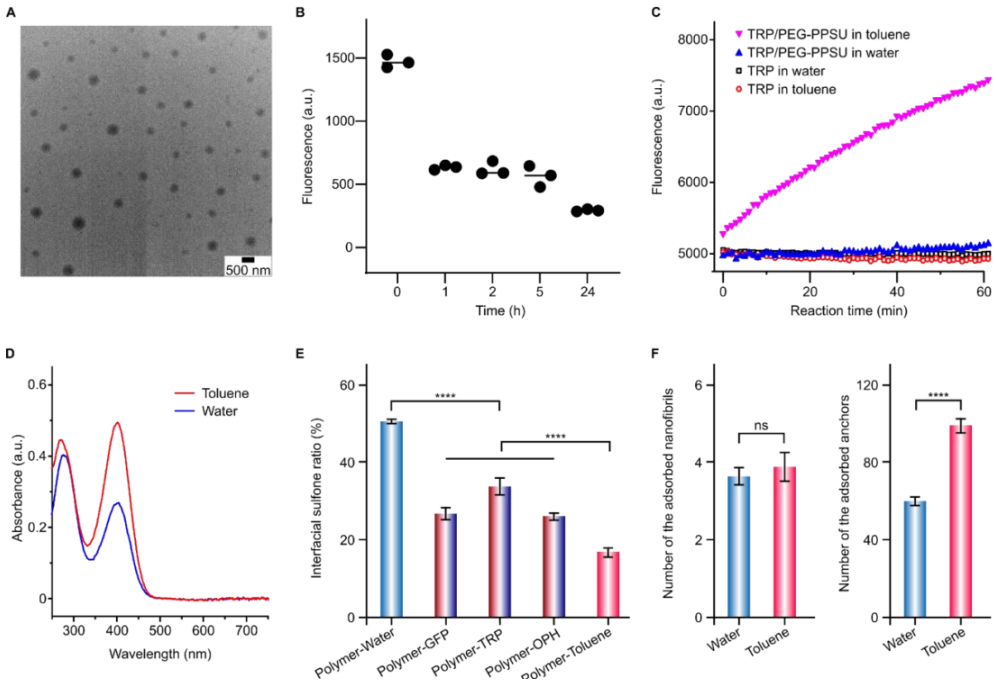

Figure 3.12: Experiments and simulations demonstrating the elevated thermal stability of proteins through nanoconfinement. (A) TEM imaging of nanoparticular GFP stabilized by PEG-PPSU in toluene. (B) Storing the nanoparticular GFP in toluene at 80 °C does not quench the fluorescence. The intensity of fluorescence (Ex/Em = 390/508 nm) was measured in toluene at 23 °C for three parallel samples. (C) PEG-PPSU preserves TRP activity in toluene rather than in water at 80 °C. The digestion reactions of FITC-BSA were performed in TRP buffer after the hot storage (5 hours in water or toluene with or without PEG-PPSU). (D) Enzymatic activity of OPH/PEG-PPSU as a function of storage media at 80 °C for 5 hours. Degradation reactions of pesticide MP were carried out in Tris-HCl to assess the activity. (E) All-atom MD simulations highlight the ability of PPSU to preserve protein function through site-specific dipole relaxations at the polymer-protein interfaces (n = 402). (F) Coarse-grained simulations supported that the dominated hydrophilic surfaces of water-soluble proteins allowed the adsorption of a higher number of propylene sulfone anchors in toluene than in water. No significant (ns) differences were found for the numbers of adsorbed nanofibrils in the two solvents. The data in (E) and (F) are presented as mean values $\pm$ standard error. Statistical significance was determined by a two-sample t-test. Statistical significance: $^{****}p \leq 0.0001$.

To elucidate the mechanism of thermal stabilization, we simulated the interactions between the proteins and PEG-PPSU in toluene (**Fig. B.43**). Dynamic PPSU undergoes site-specific dipole

relaxations to match the surface hydrophobicity/hydrophilicity of the attached patch at protein surfaces, as demonstrated in our previous observations[131]. This adsorption-induced dipole relaxations were confirmed for all the proteins, as calculated by the interfacial sulfone ratios (**Fig. 3.12E**). The results suggested the adaptable feature of the protein anchor (propylene sulfone) that its hydrophobic anchoring site was favored in polymer-protein interactions in water, whereas its hydrophilic anchoring site was preferred in toluene. In comparison, the recently developed random heteropolymers for protein retention in organic solvents utilized the 4 types of side chains, either hydrophilic (charged or not) or hydrophobic, to achieve the adaptable orientations according to the surface hydrophilicity/hydrophobicity at the binding sites[99]. In principle, our PPSU polymers alone achieve similar structural adaptability for preserving protein activity with the inclusion of the PEG portion for the fine-tuning of protein adsorption.

On the basis of these data, a coarse-grained model was built for simulating the adsorption of nanofibrils by a model protein with a higher ratio of hydrophilic surfaces (**Fig. B.44**). The obtained simulation results showed that an increased number of propylene sulfone were adsorbed at the protein surface in toluene than in water. Regardless of the solvents used, 4 were adsorbed around the surface of the model protein. The number of adsorbed nanofibrils could be limited due to spatial hinderance and the size of the target protein. These results suggested an improved confinement effect resulting from multiple-patch anchoring when transited protein/PEG-PPSU from water to toluene. Not to mention the further confinement imparted by nanofibril aggregation in toluene. The surfaces of water-soluble proteins are dominated by hydrophilic patches despite being chemically diverse and heterogeneous (**Fig. B.44**). Therefore, it is probable that the stabilization approach can be generalized to other water-soluble proteins by using the easily synthesized PEG-PPSU structure.

3.2.5 Conclusion

Our work shows that bioactive liquid droplets can be formed by physically cross-linking hydrogel nanofibrils with nonspecific proteins. The nanofibrils are easily fabricated, taking advantage of weak phase separation to achieve controlled protein affinity for maintaining protein function. Toluene drives the aggregation and redistribution of nanofibrils around the surface of a protein, leading to the confinement effect for protein stabilization. By applying this strategy, we have succeeded in preparing various nanoparticular proteins with enhanced solubility and thermal stability. As far as the stabilization mechanism is concerned, the simulations suggest the generality of the study for water-soluble proteins.

3.3 Other Works and Future Perspectives

As elaborated in previous sections, poly(propylene sulfone) (PPSU) is diverse polymeric materials with unexploited potentials. Given its biocompatibility, low-toxicity, non-selective affinity and non-destructive binding with biomolecules, PPSU emerges as a promising biomaterial with applications spanning drug delivery, controlled drug release, purification, tissue engineering, and beyond. Although notable progress has been made in the application of PPSU, the fundamental mechanisms driving its self-assembly remain inadequately understood. In this section, I will briefly review pertinent studies and propose hypotheses concerning the mechanisms underlying PPSU self-assembly.

3.3.1 Hierarchical PPSU Hydrogels for Multi-Component Vaccines

Authors: Fanfan Du, Simseok A. Yuk, Yuan Qian, Michael P. Vincent, Sharan Bobbala, Tirzah M. Abbott, Hyeohn Kim, Yang Li, Haoyu Li, Sijia Yi, Baofu Qiao and Evan A. Scott.
F.D., S.A.Y., and Y.Q. contributed equally to this work. F.D. started the studies, prepared the materials, validated the characterization, analyzed the data, and wrote the manuscript. S.A.Y. designed and conducted the *in vivo* experiments, validated the *in vivo* characterization, analyzed the data, performed SEM and rheology experiments, and wrote the manuscript. Y.Q. designed and carried out the vaccination experiments, analyzed the data, and wrote the manuscript. M.P.V. and S.B. conducted the blood analysis and drug loading experiments. T.M.A. performed the SEM-EDX experiments. H.K. conducted the rheological characterization. Y.L. performed the atomistic simulations. H.L. contributed to the flow cytometry experiment. S.Y. performed the RAW-blue macrophages experiment. B.Q. supervised the simulations. E.S. supervised the entire research process and wrote the manuscript. This work is submitted to *Nature Communication* and is under review.

In *Sec 3.1*, the potential of PPSU vesicles to capture multiple bioactive molecules is demonstrated. Here, the ability is further exploited to fictionalize PPSU with a hierarchical assembly strategy from a single simple homopolymer via a multi-stage process, that enable ratiometric loading and delivery of four physicochemically distinct adjuvants along with a protein-based antigen. Starting with a PPSU solution, the addition of water promotes interchain sulfonesulfone bonding, yielding nanogels with short PPSU coronas capable of self-bonding or protein anchoring. When

transferred into protein solutions in saline, the nanogels irreversibly aggregate into microgels as a secondary structure via surface fusion or protein bridging. Following subcutaneous injection, the microgels then bind to extracellular matrix (ECM) components, mainly collagen fibers, via PPSU coronas to form stable *in situ* nanocomposite hydrogels as the tertiary structure (**Fig. 3.13**). The delivery system takes advantage of efficient loading ($> 90\%$) throughout the process, allowing us to develop an optimized vaccine formulation. Simulation studies revealed that hydrophobic interactions promotes the molecular adsorptions onto PPSU hydrogels.

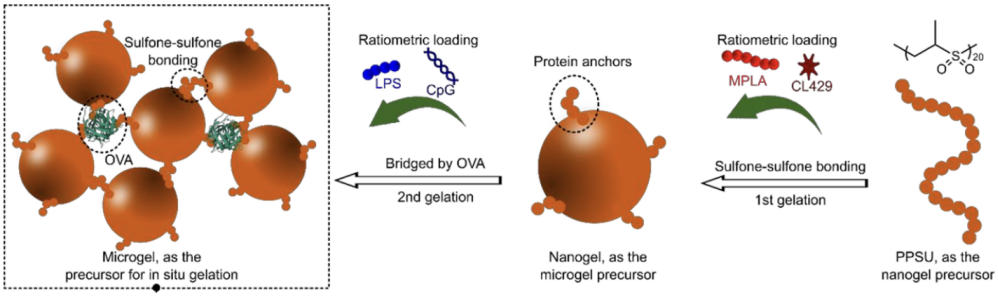

Figure 3.13: Schematic of PPSU-based hierarchical hydrogels that enable ratiometric loading of multiple adjuvants for vaccine optimization. Hydrophobic adjuvants are encapsulated through network assembly of PPSU (1^{st} gelation). Water-soluble adjuvants are adsorbed during the formation of microgels triggered by bridging nanogels with the antigen OVA (2^{nd} gelation). Microgels anchor onto collagens upon subcutaneous injection (3^{rd} gelation)

The *in vivo* studies confirmed that the multi-component-loaded PPSU hydrogels elicited a robust immunostimulatory response (**Fig. B.45a**). Furthermore, the tertiary and secondary structures of the *in situ* hydrogel facilitate the sustained release of the encapsulated antigens. Seven days post-immunization, mice immunized with PPSU-4Ad showed a significant increase in anti-OVA IgM antibodies compared to those immunized with PPSU-CpG or the blank PPSU and PBS controls (**Fig. B.45c**). This approach has the potential to reduce the frequency of vaccine administration and significantly enhance patient compliance.

3.3.2 Dipole Relaxation, Angle Relaxation and Hydrophobicity of PPSU self assembly

Experimentally, the size and morphology of PPSU self-assembled superstructures can be meticulously controlled by adjusting the hydration rate of PPSU-DMSO solutions[97]. A slow hydration rate leads to the formation of branched structures, whereas a rapid rate leads to the formation of micellar particles. An intermediate hydration rate induces the formation of hollow nanoparticles. All resulting structures remain stable suspensions due to electrostatic repulsion. It is confirmed by the fact that all stuctures have negative zeta potentials and addition of salts in the solution leads to aggregation of the particles[97]. Given that the initial and final components of the solutions are identical, the self-assembly of these distinct morphologies is a kinetically controlled process. The systems traverse distinct paths across the free energy landscape, ultimately becoming trapped in different local minima. It is hypothesized that the relative kinetics of dipole relaxation, angle relaxation, and hydrophobic interactions dictate the system's progression across the free energy landscape.

The following key observance are elucidated:

1) PPSU exhibits amphiphilic characteristics, possessing a hydrophilic $-\mathrm{SO}_2-$ group and a hydrophobic methyl group.

2) The dipole moment of the PPSU repeat unit (6.53 D) is significantly stronger than that of DMSO (5.11 D) and water (2.35 D).

3) WAXD patterns for each nanostructure indicate that crystallinity increases progressively from micelles to branched superstructures.

4) Micelles, hollow particles, and branched superstructures display decreasing Surface area/Volume ratios.

5) PPSU behaves as a flexible polymer chain in DMSO, whereas in water, it adopts a stiffer con-

formation (persistence length $l_p = 7$ repeat units).

In DMSO, the dipole-dipole interaction energy between DMSO and PPSU (E_{DM-PS}) is comparable to the interaction energy between PPSU units (E_{PS-PS}). The entropy contribution dominates the system. Conversely, in pure water, the dipole-dipole interaction energy between water and PPSU (E_{W-PS}) is higher than E_{PS-PS}. The decrease in energies (hydrophobic interactions and dipole-dipole interactions) compensates for the loss of entropy, leading to the aggregation of PPSU. When the hydration rate is rapid, the solvent's average dipole moment changes swiftly, causing aggregation before the PPSU chains can fully relax to their persistence length, thus leading to the formation of micelles, which exhibit the smallest Surface area/Volume ratio. Conversely, with a slow hydration rate, PPSU chains are afforded sufficient time to fully relax and align their dipoles with neighboring repeating units (dipole relaxation). In regions of high crystallinity, both dipoles and angles are fully relaxed, minimizing the energy contributions from chain bending and dipole-dipole interactions, which in turn leads to the formation of larger-scale structures. Branching likely arises from defects in the aggregation process; some angles may not fully relax before a chain attaches to another, resulting in branch formation. These branches do not merge due to the excessive surface negative charges they carry.

Verification of the aforementioned hypothesis via molecular dynamics simulations presents considerable challenges due to the wide range of length scales involved. The PPSU repeat unit is relatively small, with a fully extended length of approximately $4.8\mathring{A}$, yet TEM images reveal that the superstructures span a broad range of length scales, from very small micelles (a few nanometers) to large branched superstructures (several micrometers). Modeling a system encompassing such a vast range of length scales requires a highly coarse-grained model, which inevitably sacrifices critical chemical information. For instance, if a coarse-grained bead represents multiple PPSU

units, the model loses the essential alternating dipole characteristics of PPSU chains. Therefore, the development of a sophisticated model is imperative for investigating the underlying aggregation mechanism. It is hoped that this discussion will provide valuable insights for the design of such a model.

3.3.3 Conclusion

PPSU is an emerging material with exceptional properties as a biomacromolecule anchor. Through comprehensive experimental and theoretical investigations, we have demonstrated that PPSU exhibits extraordinary binding affinity with biomolecules while preserving the structural integrity and functionality of the adsorbed molecules. In this chapter, a straightforward strategy has been employed to conjugate biomolecules with PPSU particles, specifically by simply mixing the biomolecules with PPSU particles. However, more advanced applications across various fields can be envisioned if more sophisticated strategies are adopted. For instance, by first saturating PPSU nanoparticles with molecular recognition groups, it would be possible to selectively capture specific molecules, enabling functions such as purification.

Furthermore, the mechanism underlying PPSU self-assembly remains inadequately understood. A deeper understanding of this mechanism would enable greater control over the morphologies of the assembled superstructures. This, in turn, could facilitate the development of novel applications, such as the formation of a macromolecule-capturing semi-permeable film.

The potential of PPSU in various domains is significant and merits further exploration.

CHAPTER 4
CONCLUSION AND FUTURE WORK

This dissertation focuses on the study of polymeric material superstructures in biological applications. Theoretical methods and simulations have proven to be powerful tools for predicting system behavior and elucidating interaction mechanisms by enabling detailed examination of microscopic structures. When combined with experimental approaches, these methods provide researchers with a more comprehensive understanding of the subjects under investigation. The projects discussed in this dissertation involve close collaborations between theorists and experimentalists.

In Chapter 2, a peptide amphiphile (PA) system is presented for the purification of IgG from upstream products. Negatively charged PAs (fillers) co-assemble with positively charged, IgG-binding PAs (ligands) to form immunofibers. The charge states of the immunofibers were first investigated. It was predicted that after self-assembly, the local charge density increases, forming a domain of low dielectric constant with limited access to water and ions. The increased electrostatic penalty leads to the protonation of GLU groups, resulting in fewer charges over the fibers. Simulations and experiments validate this hypothesis. Subsequently, the distribution of ligands on the fiber surface is studied. The short-range attraction of the binding group Z33 in the ligand tends to cause aggregation, while the positive charges of the ligands repel each other. These competing forces result in finite-sized local segregation.

In Chapter 3, an emerging material, poly(propylene sulfone) (PPSU), is introduced. PPSU forms hollow nanoparticles (NPs) in water and non-selectively captures biomacromolecules such

as proteins. Simulation methods revealed that the dipole moments and hydrophobic methyl groups on the NP surfaces adjust their orientations to minimize energy as proteins approach. The adjustable dipole moments create matching patterns according to the protein surfaces. The semi-flexible dipole and methyl group endow PPSU NPs with the ability to non-selectively capture proteins. Subsequently, a block copolymer, PEG-PPSU, was developed to further leverage PPSU's potential for protein capture. Unlike other amphiphilic block polymers, PEG-PPSU forms nanofibrils in water rather than core-shell superstructures. The PEG-PPSU nanofibril further forms liquid droplets upon capturing proteins. Moreover, simulations indicate that PEG-PPSU captures proteins in toluene and relaxes the dipole accordingly. These liquid droplets help preserve the proteins' structure and function in toluene. This study presents a new potential strategy for protein protection and has potential applications in biomolecule storage.

Polymeric biomaterials have been extensively investigated and applied in various fields due to their versatility. This dissertation primarily focuses on protein-binding functional polymer superstructures. Regardless of the eventual applications, binding affinity or capture efficiency remains the ultimate criterion that researchers aim to improve. Multiple factors, such as the geometry of the superstructures and the kinetic processes involved, have a profound synergy in this regard. In Chapters 2 and 3.2, nanofibers are utilized to capture molecules and induce phase separation, while in Chapter 3.3.1, a strategy to use nanoparticle hydrogels for protein capture is briefly introduced. Although the merits and demerits of these methods are not compared, a thorough study comparing the efficiency of different superstructures in similar applications would be beneficial.

Furthermore, due to the nature of polymeric materials, some systems may not fully evolve to thermodynamic equilibrium but rather become trapped in configurations that require significant

energy to overcome the barriers. Therefore, the kinetics of these processes are crucial in determining binding efficiency. In simulation studies, the initial configuration of a system can sometimes have a determinant effect on the final configuration. In other words, different initial configurations may lead to distinct outcomes that differ from reality. Careful consideration is needed in building initial configurations and studying kinetic processes.

Another important direction is the development of high-level coarse-grained models that are highly concise. Systems in biological applications generally have very large length scales (μm), which exceed the capabilities of all-atom simulations and most traditional coarse-grained simulations. Thus, there are obstacles in validating hypotheses for certain phenomena. Advanced models that are highly coarse-grained yet contain critical chemical and physical information are needed. Traditional mapping methods from high-resolution models involve fitting the coarse-grained models to high-resolution models (such as all-atom) by mapping geometry (bond length, angle, dihedral) and interactions (Lennard-Jones, electrostatics). However, in a highly coarse-grained model, most information is neglected, and only critical parameters are retained. The traditional mapping methods do not prioritize any parameters, and as a result, they are insufficient on their own. Theoretical methods and experiments are required to help identify the crucial characteristics of the systems of interest and to develop a highly concise yet accurate model.

The future directions mentioned above are universally applicable to the field of polymeric material research and are not limited to the projects discussed in this dissertation. These research directions will contribute to the broader field of materials science, paving the way for new technological advancements and fostering innovative solutions to current challenges.

REFERENCES

1. Karikó, K., Buckstein, M., Ni, H. & Weissman, D. Suppression of RNA Recognition by Toll-like Receptors: The Impact of Nucleoside Modification and the Evolutionary Origin of RNA. *Immunity* **23,** 165–175. ISSN: 1074-7613 (2 Aug. 2005).

2. Becker, M. L. & Burdick, J. A. Introduction: Polymeric Biomaterials. *Chemical Reviews* **121,** 10789–10791. ISSN: 15206890. https://pubs.acs.org/doi/full/10.1021/acs.chemrev.1c00354 (18 Sept. 2021).

3. Ramachandran, S., Satapathy, S. R. & Dutta, T. Delivery Strategies for mRNA Vaccines. *Pharmaceutical Medicine* **36,** 11–20. ISSN: 11791993. https://link.springer.com/article/10.1007/s40290-021-00417-5 (1 Feb. 2022).

4. Kohane, D. S. & Langer, R. Polymeric Biomaterials in Tissue Engineering. *Pediatric Research 2008 63:5* **63,** 487–491. ISSN: 1530-0447. https://www.nature.com/articles/pr200899 (May 2008).

5. Someya, T., Bao, Z. & Malliaras, G. G. The rise of plastic bioelectronics. *Nature 2016 540:7633* **540,** 379–385. ISSN: 1476-4687. https://www.nature.com/articles/nature21004 (7633 Dec. 2016).

6. Zhang, A. *et al.* Ultraflexible endovascular probes for brain recording through micrometer-scale vasculature. *Science* **381,** 306–312. ISSN: 10959203. https://www.science.org/doi/10.1126/science.adh3916 (6655 July 2023).

7. Zhang, A. & Lieber, C. M. Nano-Bioelectronics. *Chemical Reviews* **116,** 215–257. ISSN: 15206890. https://pubs.acs.org/doi/full/10.1021/acs.chemrev.5b00608 (1 Jan. 2016).

8. Gronemeyer, P., Ditz, R. & Strube, J. Trends in Upstream and Downstream Process Development for Antibody Manufacturing. *Bioengineering 2014, Vol. 1, Pages 188-212* **1,** 188–212. ISSN: 2306-5354. https://www.mdpi.com/2306-5354/1/4/188/htmhttps://www.mdpi.com/2306-5354/1/4/188 (Oct. 2014).

9. Bolton, G. R. & Mehta, K. K. The role of more than 40 years of improvement in protein A chromatography in the growth of the therapeutic antibody industry. *Biotechnology Progress*

32, 1193–1202. ISSN: 1520-6033. https://onlinelibrary.wiley.com/doi/full/10.1002/btpr.2324https://onlinelibrary.wiley.com/doi/abs/10.1002/btpr.2324https://aiche.onlinelibrary.wiley.com/doi/10.1002/btpr.2324 (Sept. 2016).

10. Isom, D. G., Castañeda, C. A., Cannon, B. R., Velu, P. D. & García-Moreno E, B. Charges in the hydrophobic interior of proteins. *Proceedings of the National Academy of Sciences of the United States of America* **107,** 16096–16100. ISSN: 10916490. https://www.pnas.org/doi/abs/10.1073/pnas.1004213107 (Sept. 2010).

11. Tang, C., Smith, A. M., Collins, R. F., Ulijn, R. V. & Saiani, A. Fmoc-Diphenylalanine Self-ASsembly Mechanism Induces Apparent pK a Shifts. *Langmuir* **25,** 9447–9453. ISSN: 07437463. https://pubs.acs.org/doi/full/10.1021/la900653q (Aug. 2009).

12. Behanna, H. A., Donners, J. J., Gordon, A. C. & Stupp, S. I. Coassembly of amphiphiles with opposite peptide polarities into nanofibers. *Journal of the American Chemical Society* **127,** 1193–1200. ISSN: 00027863. https://pubs.acs.org/doi/full/10.1021/ja044863u (Feb. 2005).

13. Zaldivar, G., Vemulapalli, S., Udumula, V., Conda-Sheridan, M. & Tagliazucchi, M. Self-Assembled Nanostructures of Peptide Amphiphiles: Charge Regulation by Size Regulation. *Journal of Physical Chemistry C* **123,** 17606–17615. ISSN: 19327455. https://pubs.acs.org/doi/full/10.1021/acs.jpcc.9b04280 (June 2019).

14. Nap, R. J. *et al.* Acid-Base Equilibrium and Dielectric Environment Regulate Charge in Supramolecular Nanofibers. *Frontiers in Chemistry* **10,** 145. ISSN: 2296-2646. https://www.frontiersin.org/articles/10.3389/fchem.2022.852164/full (Mar. 2022).

15. Choi, S., Knoerdel, A. R., Sing, C. E. & Keating, C. D. Effect of Polypeptide Complex Coacervate Microenvironment on Protonation of a Guest Molecule. *The Journal of Physical Chemistry B.* ISSN: 1520-6106. https://pubs.acs.org/doi/full/10.1021/acs.jpcb.3c02098 (July 2023).

16. Yu, Z. *et al.* Co-assembly of Peptide Amphiphiles and Lipids into Supramolecular Nanostructures Driven by Anion-pi Interactions. *Journal of the American Chemical Society* **139,** 7823–7830. ISSN: 15205126. https://pubs.acs.org/doi/full/10.1021/jacs.7b02058 (June 2017).

17. Leung, C.-Y. *et al.* Molecular Crystallization Controlled by pH Regulates Mesoscopic Membrane Morphology. *ACS Nano* **6,** 10901–10909. ISSN: 1936-0851. https://doi.org/10.1021/nn304321w (Dec. 2012).

18. Longo, G. S., Olvera De La Cruz, M. & Szleifer, I. Molecular Theory of Weak Polyelectrolyte Gels: The Role of pH and Salt Concentration. *Macromolecules.* https://pubs.acs.org/sharingguidelines (2010).

19. Tagliazucchi, M., De La Cruz, M. O. & Szleifer, I. Self-organization of grafted polyelectrolyte layers via the coupling of chemical equilibrium and physical interactions. *Proceedings of the National Academy of Sciences of the United States of America* **107,** 5300–5305. ISSN: 00278424. https://www.pnas.org/doi/abs/10.1073/pnas.0913340107 (Mar. 2010).

20. McCourt, J. M. *et al.* Electrostatic Control of Shape Selection and Nanoscale Structure in Chiral Molecular Assemblies. *ACS Central Science* **8,** 1169–1181. ISSN: 23747951. https://pubs.acs.org/doi/full/10.1021/acscentsci.2c00447 (Aug. 2022).

21. Li, Y. *et al.* Bioinspired supramolecular engineering of self-assembling immunofibers for high affinity binding of immunoglobulin G. *Biomaterials* **178,** 448–457 (Sept. 2018).

22. Gaddam, P. & Ducker, W. Electrostatic Screening Length in Concentrated Salt Solutions. *Langmuir* **35,** 5719–5727. ISSN: 15205827. https://pubs.acs.org/doi/full/10.1021/acs.langmuir.9b00375 (Apr. 2019).

23. Cote, Y. *et al.* Mechanism of the pH-controlled self-assembly of nanofibers from peptide amphiphiles. *Journal of Physical Chemistry C* **118,** 16272–16278. ISSN: 19327455. https://pubs.acs.org/doi/full/10.1021/jp5048024 (July 2014).

24. Lee, O.-S., Cho, V. & Schatz, G. C. Modeling the Self-Assembly of Peptide Amphiphiles into Fibers Using Coarse-Grained Molecular Dynamics. *Nano Lett* **12,** 4907–4913. https://pubs.acs.org/sharingguidelines (2012).

25. Xiong, Q., Stupp, S. I. & Schatz, G. C. Molecular Insight into the β-Sheet Twist and Related Morphology of Self-Assembled Peptide Amphiphile Ribbons. *Journal of Physical Chemistry Letters* **12,** 11238–11244. ISSN: 19487185. https://pubs.acs.org/doi/full/10.1021/acs.jpclett.1c03243 (Nov. 2021).

26. Abraham, M. J. *et al.* GROMACS: High performance molecular simulations through multi-level parallelism from laptops to supercomputers. *SoftwareX* **1-2,** 19–25. ISSN: 2352-7110 (Sept. 2015).

27. Huang, J. *et al.* CHARMM36m: An improved force field for folded and intrinsically disordered proteins. *Nature Methods* **14,** 71–73. ISSN: 15487105. /pmc/articles/PMC5199616/ /pmc/articles/PMC5199616/?report=abstracthttps://www.ncbi.nlm.nih.gov/pmc/articles/PMC5199616/ (Dec. 2016).

28. Miyamoto, S. & Kollman, P. A. Settle: An analytical version of the SHAKE and RATTLE algorithm for rigid water models. *Journal of Computational Chemistry* **13,** 952–962. ISSN: 1096-987X. https://onlinelibrary.wiley.com/doi/full/10.1002/jcc.540130805https://onlinelibrary.wiley.com/doi/abs/10.1002/jcc.540130805https://onlinelibrary.wiley.com/doi/10.1002/jcc.540130805 (Oct. 1992).

29. Humphrey, W., Dalke, A. & Schulten, K. VMD: Visual molecular dynamics. *Journal of Molecular Graphics* **14,** 33–38. ISSN: 02637855. https://pubmed.ncbi.nlm.nih.gov/8744570/ (1996).

30. Michaud-Agrawal, N., Denning, E. J., Woolf, T. B. & Beckstein, O. MDAnalysis: A toolkit for the analysis of molecular dynamics simulations. *Journal of Computational Chemistry* **32,** 2319–2327. ISSN: 01928651 (2011).

31. Hanwell, M. D. *et al.* Avogadro: An advanced semantic chemical editor, visualization, and analysis platform. *Journal of Cheminformatics* **4,** 1–17. ISSN: 17582946. https://jcheminf.biomedcentral.com/articles/10.1186/1758-2946-4-17 (Aug. 2012).

32. Martinez, L., Andrade, R., Birgin, E. G. & Martínez, J. M. PACKMOL: A package for building initial configurations for molecular dynamics simulations. *Journal of Computational Chemistry* **30,** 2157–2164. ISSN: 1096-987X. https://onlinelibrary.wiley.com/doi/full/10.1002/jcc.21224https://onlinelibrary.wiley.com/doi/abs/10.1002/jcc.21224https://onlinelibrary.wiley.com/doi/10.1002/jcc.21224 (Oct. 2009).

33. Lee, O. S., Stupp, S. I. & Schatz, G. C. Atomistic molecular dynamics simulations of peptide amphiphile self-assembly into cylindrical nanofibers. *Journal of the American Chemical Society* **133,** 3677–3683. ISSN: 00027863. https://pubs.acs.org/doi/full/10.1021/ja110966y (Mar. 2011).

34. Souza, P. C. *et al.* Martini 3: a general purpose force field for coarse-grained molecular dynamics. *Nature Methods 2021 18:4* **18,** 382–388. ISSN: 1548-7105. https://www.nature.com/articles/s41592-021-01098-3 (Mar. 2021).

35. Li, Y. *et al.* Selective Capture and Recovery of Monoclonal Antibodies by Self-Assembling Supramolecular Polymers of High Affinity for Protein Binding. *Nano Letters* **20,** 6957–6965. ISSN: 15306992. https://pubs.acs.org/doi/full/10.1021/acs.nanolett.0c01297 (Oct. 2020).

36. Wang, J., Liu, K., Xing, R. & Yan, X. Peptide self-assembly: thermodynamics and kinetics. *Chemical Society Reviews* **45,** 5589–5604. ISSN: 1460-4744. https://pubs.rsc.org/en/content/articlehtml/2016/cs/c6cs00176ahttps://pubs.rsc.org/en/content/articlelanding/2016/cs/c6cs00176a (Oct. 2016).

37. Dasgupta, A. & Das, D. Designer Peptide Amphiphiles: Self-Assembly to Applications. *Langmuir* **35,** 10704–10724. ISSN: 15205827. https://pubs.acs.org/doi/full/10.1021/acs.langmuir.9b01837 (Aug. 2019).

38. Qi, R. *et al.* Peptide Amphiphiles with Distinct Supramolecular Nanostructures for Controlled Antibacterial Activities. *ACS Applied Bio Materials* **1,** 21–26. ISSN: 25766422. https://pubs.acs.org/doi/full/10.1021/acsabm.8b00005 (July 2018).

39. Chen, C. *et al.* High Selective Performance of Designed Antibacterial and Anticancer Peptide Amphiphiles. *ACS Applied Materials and Interfaces* **7,** 17346–17355. ISSN: 19448252. https://pubs.acs.org/doi/full/10.1021/acsami.5b04547 (Aug. 2015).

40. Hartgerink, J. D., Beniash, E. & Stupp, S. I. Self-Assembly and Mineralization of Peptide-Amphiphile Nanofibers. *Science* **294,** 1684–1688. ISSN: 0036-8075. https://www.science.org/doi/10.1126/science.1063187 (Nov. 2001).

41. Palmer, L. C., Newcomb, C. J., Kaltz, S. R., Spoerke, E. D. & Stupp, S. I. Biomimetic systems for hydroxyapatite mineralization inspired by bone and enamel. *Chemical Reviews* **108,** 4754–4783. ISSN: 00092665. https://pubs.acs.org/doi/full/10.1021/cr8004422 (Nov. 2008).

42. Li, L.-L. *et al.* An Adaptive Biointerface from Self-Assembled Functional Peptides for Tissue Engineering. *Advanced Materials* **27,** 3181–3188. ISSN: 1521-4095. https://onlinelibrary.wiley.com/doi/full/10.1002/adma.201500658https:

//onlinelibrary.wiley.com/doi/abs/10.1002/adma.201500658https://onlinelibrary.wiley.com/doi/10.1002/adma.201500658 (May 2015).

43. Kumar, D. *et al.* Peptide Hydrogels—A Tissue Engineering Strategy for the Prevention of Oesophageal Strictures. *Advanced Functional Materials* **27,** 1702424. ISSN: 1616-3028. https://onlinelibrary.wiley.com/doi/full/10.1002/adfm.201702424https://onlinelibrary.wiley.com/doi/abs/10.1002/adfm.201702424https://onlinelibrary.wiley.com/doi/10.1002/adfm.201702424 (Oct. 2017).

44. Preslar, A. T. *et al.* 19F Magnetic Resonance Imaging Signals from Peptide Amphiphile Nanostructures Are Strongly Affected by Their Shape. *ACS Nano* **10,** 7376–7384. ISSN: 1936086X. https://pubs.acs.org/doi/full/10.1021/acsnano.6b00267 (Aug. 2016).

45. Bull, S. R. *et al.* Magnetic resonance imaging of self-assembled biomaterial scaffolds. *Bioconjugate Chemistry* **16,** 1343–1348. ISSN: 10431802. https://pubs.acs.org/doi/full/10.1021/bc050153h (2005).

46. Sai, H. *et al.* Imaging Supramolecular Morphogenesis with Confocal Laser Scanning Microscopy at Elevated Temperatures. *Nano Letters* **20,** 4234–4241. ISSN: 15306992. https://pubs.acs.org/doi/full/10.1021/acs.nanolett.0c00662 (June 2020).

47. Peters, E. B. *et al.* Self-Assembled Peptide Amphiphile Nanofibers for Controlled Therapeutic Delivery to the Atherosclerotic Niche. *Advanced Therapeutics* **4,** 2100103. ISSN: 2366-3987. https://onlinelibrary.wiley.com/doi/full/10.1002/adtp.202100103https://onlinelibrary.wiley.com/doi/abs/10.1002/adtp.202100103https://onlinelibrary.wiley.com/doi/10.1002/adtp.202100103 (Sept. 2021).

48. Martin, S. *et al.* Peptide amphiphile nanofiber hydrogel delivery of Sonic hedgehog protein to the penis and cavernous nerve suppresses intrinsic and extrinsic apoptotic signaling mechanisms, which are an underlying cause of erectile dysfunction. *Nanomedicine: Nanotechnology, Biology, and Medicine* **37.** ISSN: 15499642 (Oct. 2021).

49. Barrett, J. C. & Tirrell, M. V. in *Methods in Molecular Biology* 277–292 (Humana Press Inc., 2018). https://link.springer.com/protocol/10.1007/978-1-4939-7893-9_21http://link.springer.com/10.1007/978-1-4939-7893-9_21.

50. Singha, N. *et al.* Hydrogelation of a Naphthalene Diimide Appended Peptide Amphiphile and Its Application in Cell Imaging and Intracellular pH Sensing. *Biomacromolecules* **18,** 3630–3641. ISSN: 15264602. https://pubs.acs.org/doi/full/10.1021/acs.biomac.7b01048 (Nov. 2017).

51. Niece, K. L., Hartgerink, J. D., Donners, J. J. & Stupp, S. I. Self-assembly combining two bioactive peptide-amphiphile molecules into nanofibers by electrostatic attraction. *Journal of the American Chemical Society* **125,** 7146–7147. ISSN: 00027863. https://pubs.acs.org/doi/full/10.1021/ja028215r (June 2003).

52. Braisted, A. C. & Wells, J. A. Minimizing a binding domain from protein A. *Proceedings of the National Academy of Sciences* **93,** 5688–5692. ISSN: 00278424. https://www.pnas.org/doi/abs/10.1073/pnas.93.12.5688 (June 1996).

53. Van Eldijk, M. B., Smits, F. C., Thies, J. C., Mecinović, J. & Van Hest, J. C. Thermodynamic investigation of Z33-antibody interaction leads to selective purification of human antibodies. *Journal of Biotechnology* **179,** 32–41. ISSN: 0168-1656 (June 2014).

54. Cook, M. A. & Wright, G. D. The past, present, and future of antibiotics. *Science Translational Medicine* **14,** 7793. ISSN: 19466242. https://www.science.org/doi/10.1126/scitranslmed.abo7793 (Aug. 2022).

55. Canepa, E. *et al.* Amphiphilic gold nanoparticles perturb phase separation in multidomain lipid membranes. *Nanoscale* **12,** 19746–19759. ISSN: 2040-3372. https://pubs.rsc.org/en/content/articlehtml/2020/nr/d0nr05366jhttps://pubs.rsc.org/en/content/articlelanding/2020/nr/d0nr05366j (Oct. 2020).

56. Dongsheng, Z. & De La Cruz, M. O. Nanopatterns in tethered membranes of weakly charged chains with hydrophobic backbones. *Macromolecules* **41,** 6612–6614. ISSN: 00249297. https://pubs.acs.org/doi/full/10.1021/ma8011619 (Sept. 2008).

57. Lamar, C., Liu, Y., Yi, C. & Nie, Z. Entropy-driven segregation and budding in hybrid vesicles of binary nanoparticle amphiphiles. *Giant* **1,** 100010. ISSN: 2666-5425 (Mar. 2020).

58. Lu, M. *et al.* Phase-Separation-Induced Porous Hydrogels from Amphiphilic Triblock Copolymer with High Permeability and Mechanical Strength. *Chemistry of Materials* **34,** 10995–11006. ISSN: 15205002. https://pubs.acs.org/doi/full/10.1021/acs.chemmater.2c03004 (Dec. 2022).

59. Hebbeker, P., Steinschulte, A. A., Schneider, S. & Plamper, F. A. Balancing Segregation and Complexation in Amphiphilic Copolymers by Architecture and Confinement. *Langmuir* **33,** 4091–4106. ISSN: 15205827. https://pubs.acs.org/doi/full/10.1021/acs.langmuir.6b04602 (May 2017).

60. Honda, S., Koga, M., Tokita, M., Yamamoto, T. & Tezuka, Y. Phase separation and self-assembly of cyclic amphiphilic block copolymers with a main-chain liquid crystalline segment. *Polymer Chemistry* **6,** 4167–4176. ISSN: 1759-9962. https://pubs.rsc.org/en/content/articlehtml/2015/py/c5py00346fhttps://pubs.rsc.org/en/content/articlelanding/2015/py/c5py00346f (May 2015).

61. Solis, F. J., Stupp, S. I. & De La Cruz, M. O. Charge induced pattern formation on surfaces: Segregation in cylindrical micelles of cationic-anionic peptide-amphiphiles. *Journal of Chemical Physics* **122,** 54905. ISSN: 00219606. /aip/jcp/article/122/5/054905/186770/Charge-induced-pattern-formation-on-surfaces (Feb. 2005).

62. Kohlstedt, K. L., Solis, F. J., Vernizzi, G. & De La Cruz, M. O. Spontaneous chirality via long-range electrostatic forces. *Physical Review Letters* **99,** 030602. ISSN: 00319007. https://journals.aps.org/prl/abstract/10.1103/PhysRevLett.99.030602 (July 2007).

63. Solis, F. J., Vernizzi, G. & Olvera De La Cruz, M. Electrostatic-driven pattern formation in fibers, nanotubes and pores. *Soft Matter* **7,** 1456–1466. ISSN: 1744-6848. https://pubs.rsc.org/en/content/articlehtml/2011/sm/c0sm00706dhttps://pubs.rsc.org/en/content/articlelanding/2011/sm/c0sm00706d (Feb. 2011).

64. Da Silva, R. M. *et al.* Super-resolution microscopy reveals structural diversity in molecular exchange among peptide amphiphile nanofibres. *Nature Communications 2016 7:1* **7,** 1–10. ISSN: 2041-1723. https://www.nature.com/articles/ncomms11561 (May 2016).

65. Li, Y. *et al.* Aggregation-Induced Asymmetric Charge States of Amino Acids in Supramolecular Nanofibers. *Journal of Physical Chemistry B* **127,** 8176–8184. ISSN: 15205207. https://pubs.acs.org/doi/full/10.1021/acs.jpcb.3c05598 (Sept. 2023).

66. Jarin, Z., Agolini, O. & Pastor, R. W. Finite-Size Effects in Simulations of Peptide/Lipid Assembly. *Journal of Membrane Biology* **255,** 437–449. ISSN: 14321424. https://link.springer.com/article/10.1007/s00232-022-00255-9 (Oct. 2022).

67. Majumder, A. & Straub, J. E. Addressing the Excessive Aggregation of Membrane Proteins in the MARTINI Model. *Journal of Chemical Theory and Computation* **17,** 2513–2521. ISSN: 15499626. https://pubs.acs.org/doi/full/10.1021/acs.jctc.0c01253 (Apr. 2021).

68. Smit, B. *et al.* Computer Simulations of Surfactant Self-Assembly. *Langmuir* **9,** 9–11. ISSN: 15205827. https://pubs.acs.org/doi/abs/10.1021/la00025a003 (1993).

69. Behjatmanesh-Ardakani, R. & Farsad, M. On the Difference between Self-Assembling Process of Monomeric and Dimeric Surfactants with the Same Head to Tail Ratio: A Lattice Monte Carlo Simulation. *Journal of Chemistry* **2013,** 525948. ISSN: 2090-9071. https://onlinelibrary.wiley.com/doi/full/10.1155/2013/525948https://onlinelibrary.wiley.com/doi/abs/10.1155/2013/525948https://onlinelibrary.wiley.com/doi/10.1155/2013/525948 (Jan. 2013).

70. Zhang, X., Arce Nunez, J. G. & Kindt, J. T. Derivation of micelle size-dependent free energies of aggregation for octyl phosphocholine from molecular dynamics simulation. *Fluid Phase Equilibria* **485,** 83–93. ISSN: 0378-3812 (Apr. 2019).

71. Srebnik, S. & Douglas, J. F. Self-assembly of charged particles on nanotubes and the emergence of particle rings, chains, ribbons and chiral sheets. *Soft Matter* **7,** 6897–6905. ISSN: 1744-6848. https://pubs.rsc.org/en/content/articlehtml/2011/sm/c1sm05168ghttps://pubs.rsc.org/en/content/articlelanding/2011/sm/c1sm05168g (July 2011).

72. Chakraborty, K., Khatua, P., Shinoda, W. & Loverde, S. M. Domain Formation in Charged Polymer Vesicles. *Macromolecules* **54,** 9258–9267. ISSN: 15205835. https://pubs.acs.org/doi/full/10.1021/acs.macromol.1c00762 (Oct. 2021).

73. Miliou, K., Gergidis, L. N. & Vlahos, C. Mixed brushes consisting of oppositely charged Y-shaped polymers in salt free, monovalent, and divalent salt solutions. *Journal of Polymer Science* **58,** 1757–1770. ISSN: 2642-4169. https://onlinelibrary.wiley.com/doi/full/10.1002/pol.20200141https://onlinelibrary.wiley.com/doi/abs/10.1002/pol.20200141https://onlinelibrary.wiley.com/doi/10.1002/pol.20200141 (July 2020).

74. Alessandri, R. *et al.* Martini 3 Coarse-Grained Force Field: Small Molecules. *Advanced Theory and Simulations* **5,** 2100391. ISSN: 2513-0390. https://onlinelibrary.wiley.com/doi/full/10.1002/adts.202100391https://onlinelibrary.

wiley.com/doi/abs/10.1002/adts.202100391https://onlinelibrary.wiley.com/doi/10.1002/adts.202100391 (Jan. 2022).

75. Kroon, P. C. *et al.* Martinize2 and Vermouth: Unified Framework for Topology Generation. arXiv: 2212.01191 (2022).

76. Stukowski, A. Visualization and analysis of atomistic simulation data with OVITO–the Open Visualization Tool. *Modelling and Simulation in Materials Science and Engineering* **18,** 015012. ISSN: 0965-0393. https://iopscience.iop.org/article/10.1088/0965-0393/18/1/015012https://iopscience.iop.org/article/10.1088/0965-0393/18/1/015012/meta (Dec. 2009).

77. Tirado, M. M., Martínez, C. L., Torre, J. G. D. L., Martfnez, C. L. & Torre, J. G. D. L. Comparison of theories for the translational and rotational diffusion coefficients of rod-like macromolecules. Application to short DNA fragments. *The Journal of Chemical Physics* **81,** 2047–2052. ISSN: 0021-9606. /aip/jcp/article/81/4/2047/452506/Comparison-of-theories-for-the-translational-and (4 Aug. 1984).

78. Broersma, S. Viscous force and torque constants for a cylinder. *The Journal of Chemical Physics* **74,** 6989–6990. ISSN: 0021-9606. /aip/jcp/article/74/12/6989/767471/Viscous-force-and-torque-constants-for-a-cylinder (12 June 1981).

79. Ramsey, A., Bischoff, A. & Francis, M. Enzyme Activated Gold Nanoparticles for Versatile Site-Selective Bioconjugation. *Journal of the American Chemical Society* **143,** 7342–7350 (19 2021).

80. Chen, J. *et al.* Tocilizumab–Conjugated Polymer Nanoparticles for NIR-II Photoacoustic-Imaging-Guided Therapy of Rheumatoid Arthritis. *Advanced Materials* **32** (37 2020).

81. Wang, X.-D. *et al.* Multifunctional Silica Nanoparticles for Covalent Immobilization of Highly Sensitive Proteins. *Advanced Materials* **27,** 7945–7950. ISSN: 1521-4095. https://onlinelibrary.wiley.com/doi/full/10.1002/adma.201503935https://onlinelibrary.wiley.com/doi/abs/10.1002/adma.201503935https://onlinelibrary.wiley.com/doi/10.1002/adma.201503935 (48 Dec. 2015).

82. Nel, A. *et al.* Understanding biophysicochemical interactions at the nano-bio interface. *Nature Materials* **8,** 543–557 (7 2009).

83. Walkey, C. & Chan, W. Understanding and controlling the interaction of nanomaterials with proteins in a physiological environment. *Chemical Society Reviews* **41,** 2780–2799 (7 2012).

84. Rabe, M., Verdes, D. & Seeger, S. Understanding protein adsorption phenomena at solid surfaces. *Advances in Colloid and Interface Science* **162,** 87–106 (1-2 2011).

85. Cao, Z.-T. *et al.* Protein Binding Affinity of Polymeric Nanoparticles as a Direct Indicator of Their Pharmacokinetics. *ACS Nano* **14,** 3563–3575 (3 2020).

86. Estephan, Z., Jaber, J. & Schlenoff, J. Zwitterion-stabilized silica nanoparticles: Toward nonstick nano. *Langmuir* **26,** 16884–16889 (22 2010).

87. Debayle, M. *et al.* Zwitterionic polymer ligands: an ideal surface coating to totally suppress protein-nanoparticle corona formation? *Biomaterials* **219** (2019).

88. Vincent, M., Navidzadeh, J., Bobbala, S. & Scott, E. Leveraging self-assembled nanobiomaterials for improved cancer immunotherapy. *Cancer Cell* **40,** 255–276 (3 2022).

89. Vincent, M. *et al.* Surface chemistry-mediated modulation of adsorbed albumin folding state specifies nanocarrier clearance by distinct macrophage subsets. *Nature Communications* **12** (1 2021).

90. Vincent, M. *et al.* The Combination of Morphology and Surface Chemistry Defines the Immunological Identity of Nanocarriers in Human Blood. *Advanced Therapeutics* **4** (8 2021).

91. Duan, S. *et al.* Nanoparticles displaying allergen and siglec-8 ligands suppress IgE-FceRIMediated anaphylaxis and desensitize mast cells to subsequent antigen challenge. *Journal of Immunology* **206,** 2290–2300 (10 2021).

92. Duan, S. *et al.* CD33 recruitment inhibits IgE-mediated anaphylaxis and desensitizes mast cells to allergen. *Journal of Clinical Investigation* **129,** 1387–1401 (3 2019).

93. Albert, C. *et al.* Monobody adapter for functional antibody display on nanoparticles for adaptable targeted delivery applications. *Nature Communications* **13** (1 2022).

94. Tonigold, M. *et al.* Pre-adsorption of antibodies enables targeting of nanocarriers despite a biomolecular corona. *Nature Nanotechnology* **13,** 862–869 (9 2018).

95. Schöttler, S. *et al.* Protein adsorption is required for stealth effect of poly(ethylene glycol)- and poly(phosphoester)-coated nanocarriers. *Nature Nanotechnology* **11,** 372–377 (4 2016).

96. Kocbek, P., Obermajer, N., Cegnar, M., Kos, J. & Kristl, J. Targeting cancer cells using PLGA nanoparticles surface modified with monoclonal antibody. *Journal of Controlled Release* **120,** 18–26 (1-2 2007).

97. Du, F. *et al.* Homopolymer self-assembly of poly(propylene sulfone) hydrogels via dynamic noncovalent sulfone–sulfone bonding. *Nature Communications 2020 11:1* **11,** 1–9. ISSN: 2041-1723. https://www.nature.com/articles/s41467-020-18657-5 (Sept. 2020).

98. Sun, H. *et al.* Origin of Proteolytic Stability of Peptide-Brush Polymers as Globular Proteomimetics. *ACS Central Science* **7,** 17. ISSN: 23747951. https://pubs.acs.org/doi/abs/10.1021/acscentsci.1c01149 (Dec. 2021).

99. Panganiban, B. *et al.* Random heteropolymers preserve protein function in foreign environments. *Science* **359,** 1239–1243. ISSN: 10959203 (2018).

100. Qiao, B., Jiménez-Ángeles, F., Nguyen, T. & Cruz, M. D. L. Water follows polar and nonpolar protein surface domains. *Proceedings of the National Academy of Sciences of the United States of America* **116,** 19274–19281 (39 2019).

101. Kolkhir, P., Elieh-Ali-Komi, D., Metz, M., Siebenhaar, F. & Maurer, M. Understanding human mast cells: lesson from therapies for allergic and non-allergic diseases. *Nature Reviews Immunology* **22,** 294–308 (5 2022).

102. Valent, P. *et al.* Drug-induced mast cell eradication: A novel approach to treat mast cell activation disorders? *Journal of Allergy and Clinical Immunology* **149,** 1866–1874 (6 2022).

103. Balbino, B. *et al.* The anti-IgE mAb omalizumab induces adverse reactions by engaging Fcγ receptors. *Journal of Clinical Investigation* **130,** 1330–1335 (3 2020).

104. Galli, S., Gaudenzio, N. & Tsai, M. *Mast Cells in Inflammation and Disease: Recent Progress and Ongoing Concerns* 49–77 (2020).

105. Gotlib, J. *et al.* Proceedings from the Inaugural American Initiative in Mast Cell Diseases (AIM) Investigator Conference. *Journal of Allergy and Clinical Immunology* **147,** 2043–2052 (6 2021).

106. Dispenza, M. *et al.* Bruton's tyrosine kinase inhibition effectively protects against human IgE-mediated anaphylaxis. *Journal of Clinical Investigation* **130,** 4759–4770 (9 2020).

107. Robida, P. *et al.* Functional and Phenotypic Characterization of Siglec-6 on Human Mast Cells. *Cells* **11** (7 2022).

108. Crocker, P., Paulson, J. & Varki, A. Siglecs and their roles in the immune system. *Nature Reviews Immunology* **7,** 255–266 (4 2007).

109. MacAuley, M., Crocker, P. & Paulson, J. Siglec-mediated regulation of immune cell function in disease. *Nature Reviews Immunology* **14,** 653–666 (10 2014).

110. Avril, T., Floyd, H., Lopez, F., Vivier, E. & Crocker, P. The membrane-proximal immunoreceptor tyrosine-based inhibitory motif is critical for the inhibitory signaling mediated by siglecs-7 and -9, CD33-related siglecs expressed on human monocytes and NK cells. *Journal of Immunology* **173,** 6841–6849 (11 2004).

111. Neuberger, M. *et al.* A hapten-specific chimaeric IgE antibody with human physiological effector function. *Nature* **314,** 268–270 (6008 1985).

112. Caslin, H. *et al. The use of human and mouse mast cell and basophil cultures to assess type 2 inflammation* 81–92 (2018).

113. Bryce, P. *et al.* Humanized mouse model of mast cell–mediated passive cutaneous anaphylaxis and passive systemic anaphylaxis. *Journal of Allergy and Clinical Immunology* **138,** 769–779 (3 2016).

114. Bao, C. *et al.* A mast cell–thermoregulatory neuron circuit axis regulates hypothermia in anaphylaxis. *Science Immunology* **8** (81 2023).

115. Schanin, J. *et al.* Discovery of an agonistic Siglec-6 antibody that inhibits and reduces human mast cells. *Communications Biology* **5** (1 2022).

116. Liang, W. *et al.* Enhanced Activity of Enzymes Encapsulated in Hydrophilic Metal-Organic Frameworks. *Journal of the American Chemical Society* **141,** 2348–2355. ISSN: 15205126. https://pubs.acs.org/doi/full/10.1021/jacs.8b10302 (6 Feb. 2019).

117. Chapman, R. & Stenzel, M. H. All Wrapped up: Stabilization of Enzymes within Single Enzyme Nanoparticles. *Journal of the American Chemical Society* **141,** 2754–2769. ISSN: 15205126. https://pubs.acs.org/doi/full/10.1021/jacs.8b10338 (7 Feb. 2019).

118. Eggers, D. K. & Valentine, J. S. Molecular confinement influences protein structure and enhances thermal protein stability. *Protein Science* **10,** 250–261. ISSN: 1469-896X. https://onlinelibrary.wiley.com/doi/full/10.1110/ps.36201https://onlinelibrary.wiley.com/doi/abs/10.1110/ps.36201https://onlinelibrary.wiley.com/doi/10.1110/ps.36201 (2 Feb. 2001).

119. Montoya, N. A. *et al.* Review on porous materials for the thermal stabilization of proteins. *Microporous and Mesoporous Materials* **333,** 111750. ISSN: 1387-1811 (Mar. 2022).

120. Wu, Y. *et al.* Nanobiocatalysis: a materials science road to biocatalysis. *Chemical Society Reviews* **51,** 6948–6964. ISSN: 1460-4744. https://pubs.rsc.org/en/content/articlehtml/2022/cs/d1cs01106ehttps://pubs.rsc.org/en/content/articlelanding/2022/cs/d1cs01106e (16 Aug. 2022).

121. Montoya, N. A. *et al.* Protein Stabilization and Delivery: A Case Study of Invasion Plasmid Antigen D Adsorbed on Porous Silica. *Langmuir* **36,** 14276–14287. ISSN: 15205827. https://pubs.acs.org/doi/full/10.1021/acs.langmuir.0c02400 (47 Dec. 2020).

122. Navarro-Sánchez, J. *et al.* Translocation of enzymes into a mesoporous MOF for enhanced catalytic activity under extreme conditions. *Chemical Science* **10,** 4082–4088. ISSN: 2041-6539. https://pubs.rsc.org/en/content/articlehtml/2019/sc/c9sc00082hhttps://pubs.rsc.org/en/content/articlelanding/2019/sc/c9sc00082h (14 Apr. 2019).

123. Bhatia, R. B., Brinker, C. J., Gupta, A. K. & Singh, A. K. Aqueous sol-gel process for protein encapsulation. *Chemistry of Materials* **12,** 2434–2441. ISSN: 08974756. https://pubs.acs.org/doi/full/10.1021/cm000260f (8 2000).

124. Chen, Y. C. *et al.* Thermal stability, storage and release of proteins with tailored fit in silica. *Scientific Reports 2017 7:1* **7,** 1–8. ISSN: 2045-2322. https://www.nature.com/articles/srep46568 (1 Apr. 2017).

125. Liang, W. *et al.* Metal-Organic Framework-Based Enzyme Biocomposites. *Chemical Reviews* **121,** 1077–1129. ISSN: 15206890. https://pubs.acs.org/doi/full/10.1021/acs.chemrev.0c01029 (3 Feb. 2021).

126. Yang, X. G. *et al.* Enhanced Activity of Enzyme Immobilized on Hydrophobic ZIF-8 Modified by Ni2+ Ions. *Angewandte Chemie International Edition* **62,** e202216699. ISSN: 1521-3773. https://onlinelibrary.wiley.com/doi/full/10.1002/anie.

202216699https://onlinelibrary.wiley.com/doi/abs/10.1002/anie.202216699https://onlinelibrary.wiley.com/doi/10.1002/anie.202216699 (7 Feb. 2023).

127. Del Castillo, G. F. D. *et al.* Electrically Switchable Polymer Brushes for Protein Capture and Release in Biological Environments**. *Angewandte Chemie International Edition* **61,** e202115745. ISSN: 1521-3773. https://onlinelibrary.wiley.com/doi/full/10.1002/anie.202115745https://onlinelibrary.wiley.com/doi/abs/10.1002/anie.202115745https://onlinelibrary.wiley.com/doi/10.1002/anie.202115745 (22 May 2022).

128. Ruan, Z. *et al.* Population-based heteropolymer design to mimic protein mixtures. *Nature 2023 615:7951* **615,** 251–258. ISSN: 1476-4687. https://www.nature.com/articles/s41586-022-05675-0 (7951 Mar. 2023).

129. Jiang, T. *et al.* Single-chain heteropolymers transport protons selectively and rapidly. *Nature 2020 577:7789* **577,** 216–220. ISSN: 1476-4687. https://www.nature.com/articles/s41586-019-1881-0 (7789 Jan. 2020).

130. DelRe, C. *et al.* Near-complete depolymerization of polyesters with nano-dispersed enzymes. *Nature 2021 592:7855* **592,** 558–563. ISSN: 1476-4687. https://www.nature.com/articles/s41586-021-03408-3 (7855 Apr. 2021).

131. Du, F. *et al.* Controlled adsorption of multiple bioactive proteins enables targeted mast cell nanotherapy. *Nature Nanotechnology 2024 19:5* **19,** 698–704. ISSN: 1748-3395. https://www.nature.com/articles/s41565-023-01584-z (5 Jan. 2024).

132. Burke, J. A. *et al.* Subcutaneous nanotherapy repurposes the immunosuppressive mechanism of rapamycin to enhance allogeneic islet graft viability. *Nature Nanotechnology 2022 17:3* **17,** 319–330. ISSN: 1748-3395. https://www.nature.com/articles/s41565-021-01048-2 (3 Jan. 2022).

133. Karabin, N. B. *et al.* Sustained micellar delivery via inducible transitions in nanostructure morphology. *Nature Communications 2018 9:1* **9,** 1–13. ISSN: 2041-1723. https://www.nature.com/articles/s41467-018-03001-9 (1 Feb. 2018).

134. Yi, S. *et al.* Tailoring Nanostructure Morphology for Enhanced Targeting of Dendritic Cells in Atherosclerosis. *ACS Nano* **10,** 11290–11303. ISSN: 1936086X. https://pubs.acs.org/doi/full/10.1021/acsnano.6b06451 (12 Dec. 2016).

135. Yi, S. *et al.* Surface Engineered Polymersomes for Enhanced Modulation of Dendritic Cells During Cardiovascular Immunotherapy. *Advanced Functional Materials* **29,** 1904399. ISSN: 1616-3028. https://onlinelibrary.wiley.com/doi/full/10.1002/adfm.201904399https://onlinelibrary.wiley.com/doi/abs/10.1002/adfm.201904399https://onlinelibrary.wiley.com/doi/10.1002/adfm.201904399 (42 Oct. 2019).

136. Hirose, T., Ninomiya, K., Nakagawa, S. & Yamazaki, T. A guide to membraneless organelles and their various roles in gene regulation. *Nature Reviews Molecular Cell Biology 2022 24:4* **24,** 288–304. ISSN: 1471-0080. https://www.nature.com/articles/s41580-022-00558-8 (4 Nov. 2022).

137. Liu, J., Spruijt, E., Miserez, A. & Langer, R. Peptide-based liquid droplets as emerging delivery vehicles. *Nature Reviews Materials 2023 8:3* **8,** 139–141. ISSN: 2058-8437. https://www.nature.com/articles/s41578-022-00528-8 (3 Jan. 2023).

138. Komatsu, S., Tago, M., Ando, Y., Asoh, T. A. & Kikuchi, A. Facile preparation of multi-stimuli-responsive degradable hydrogels for protein loading and release. *Journal of Controlled Release* **331,** 1–6. ISSN: 0168-3659 (Mar. 2021).

139. Gowers, R. *et al. MDAnalysis: A Python Package for the Rapid Analysis of Molecular Dynamics Simulations* in *Proceedings of the 15th Python in Science Conference* (2016), 98–105.

140. Essmann, U. *et al.* A smooth particle mesh Ewald method. *The Journal of Chemical Physics* **103,** 8577. ISSN: 0021-9606. https://aip.scitation.org/doi/abs/10.1063/1.470117 (Aug. 1995).

141. Hess, B., Bekker, H., Berendsen, H. J. C. & Fraaije, J. G. E. M. LINCS: A Linear Constraint Solver for Molecular Simulations. *J Comput Chem* **18,** 14631472 (1997).

142. Hoover, W. G. Canonical dynamics: Equilibrium phase-space distributions. *PHYSICAL REVIEW A* **31** (1985).

143. Parrinello, M. & Rahman, A. Polymorphic transitions in single crystals: A new molecular dynamics method. *Journal of Applied Physics* **52,** 7182. ISSN: 0021-8979. https://aip.scitation.org/doi/abs/10.1063/1.328693 (Aug. 1981).

144. Qiao, B., Demars, T., Olvera De La Cruz, M. & Ellis, R. J. How hydrogen bonds affect the growth of reverse micelles around coordinating metal ions. *Journal of Physical Chemistry*

Letters **5,** 1440–1444. ISSN: 19487185. https://pubs.acs.org/doi/full/10.1021/jz500495p (Apr. 2014).

145. Li, Y., Qiao, B. & Olvera de la Cruz, M. Protein Surface Printer for Exploring Protein Domains. *Journal of Chemical Information and Modeling* **60,** 5255–5264. ISSN: 15205142. https://dx.doi.org/10.1021/acs.jcim.0c00582 (Oct. 2020).

APPENDIX A

HIGH-AFFINITY SUPRAMOLECULAR PEPTIDE MATERIALS FOR SELECTIVE CAPTURE AND RECOVERY OF PROTEINS

A.1 Aggregation-Induced Asymmetric Charge States of Amino Acids in Supramolecular Nanofibers

A.1.1 Peptide amphiphile synthesis and characterization

Materials: Lauric acid (C12) was purchased from MilliporeSigma (St. Louis, MO, USA). All Fmoc amino acids and resins utilized were obtained from Advanced Automated Peptide Protein Technologies (AAPPTEC, Louisville, KY). Unless otherwise noted, all other reagents and solvents were purchased from Thermo Fisher Scientific (Waltham, MA), Sigma-Aldrich (St. Louis, MO), or VWR (Radnor, PA)

Synthesis of Peptide Amphiphiles: All peptides were synthesized using standard 9- fluorenylmethoxycarbonyl (Fmoc) solid phase peptide synthesis techniques using a Rink Amide MBHA resin. The Fmoc group on each amino acid was deprotected twice using 20% 4-methylpiperidine in dimethylformamide (DMF). Following deprotection, another amino acid was conjugated to the peptide chain using a 4:4:6 molar ratio of the Fmoc amino acid to be added, O-benzotriazole-N,N,N',N'- tetramehtyluronium-hexafluorophosphate (HBTU), and diisopropylethylamine (DIEA) to resin in DMF and allowed to react for 2 hours. Upon conjugation of all amino acids, the C12 alkyl chain (lauric acid) was conjugate using a similar 4:4:6 molar ratio of C12, HBTU, and DIEA in DMF and allowed to react overnight. The peptides were then cleaved using a 92.5:5:2.5 volumetric ratio of trifluoroacetic acid (TFA), triisopropylsilane (TIS), and water in a 10 mL total

solution after which excess TFA was evaporated under air. The peptides were then precipitated three times via centrifugation in cold diethyl ether. To evaporate any remaining ether, the resulting precipitate was then left uncapped overnight in a fume hood.

Purification of Peptide Amphiphiles: Crude peptide amphiphiles were dissolved in a mixture of water and acetonitrile (ACN) containing 0.1% ammonium hydroxide (NH4OH) by volume before being purified using a Varian ProStar Model 325 high-performance liquid chromatography (HPLC) (Agilent Technologies, Santa Clara, CA) and a Varian PLRP-S column (100 Å, 10 μm, 150 × 25 mm). The HPLC was operated using reverse phase (RP-HPLC) with water and acetonitrile as the mobile phases at a flow rate of 16 mL/min with 10 mL injections (Fig. S1a). Intensity at 220 nm wavelength was monitored. Collected fractions were analyzed for the target product using a Bruker AutoFlex Max Maldi ToF/ToF (MALDI-TOF) instrument (Billerica, MA), and fractions containing the target product were combined (Fig. S1b). The combined fractions then underwent rotary evaporation to remove excess ACN before being lyophilized with a FreeZone -105°C 4.5L freeze dryer (Labconco, Kansas City, MO). The lyophilized peptides were then re-characterized using the aforementioned MALDI-TOF and an Agilent 1260 Infinity II in reverse phase using water and acetonitrile as the mobile phases (see Fig. S1) before the purified powders were stored in a -30∘C freezer.

Mass Spectroscopy: Matrix-assisted laser desorption/ionization time of flight (MALDI-TOF) mass spectra were obtained using a Bruker AutoFlex Max Maldi ToF/ToF instrument (Billerica, MA) (Fig. S1b). Water with 0.1% NH_4OH was used to dissolve the peptide amphiphiles before being mixed with a 10 mg/mL sinapic acid matrix in 50:50 water:ACN mixture with 0.1% formic acid, which was then pipetted onto the target plate. A 355 nm UV laser was used to irradiate the samples before being analyzed in the reflection/linear mode.

A.1.2 Peptide amphiphile self-assembly, titration, and characterization

Self-Assembly of Peptide Amphiphiles: The lyophilized peptide amphiphile powders were first pretreated with hexafluoro-2-propanol (HFIP) to eliminate any pre-existing structures before assembly. After evaporating off the HFIP, enough Nanopure water was added to reach a final concentration of 2.5 mM. The peptide amphiphile solutions were sonicated in a 45°C water bath for 40 minutes to aid in dissolution before being left overnight at room temperature to allow for complete assembly.

Titration of Peptide Amphiphiles: Titration curves were determined by adding 10 μL of 0.1M NaOH or HCl at a time to 5 mL of the assembled peptide amphiphile solutions. After each addition of NaOH or HCl, the pH was measured using a Mettler Toledo SevenMulti with an InLab Micro electrode, which was calibrated prior to experiments using pH 4, 7, and 10 buffers.

Dynamic Light Scattering (DLS): 100 mM C12-VVEE dissolved in Nanopure water were tuned to the appropriate pH before being allowed to assemble at room temperature overnight. The next day, the peptide amphiphile solutions were placed into UV-Transparent Disposable Cuvettes ZEN0118 made of polystyrene latex (Sarstedt, Germany) and analyzed for size using a Zetasizer Nano ZS90 (Malvern Instruments, UK) at 25.0∘C. The experiments were performed in triplicate and the mean of three measurements is presented.

Transmission Electron Microscopy (TEM): After assembly, 10 μL of 10 fold diluted peptide amphiphile solutions were spotted onto a carbon-coated copper grid with 400 square mesh (Electron Microscopy Services, Hatfield, PA, USA), and the resulting droplet was left for 1 minute before the excess was wicked away with filter paper. After allowing the sample to dry for at least 2 minutes, 10 μL of 2 wt% uranyl acetate was spotted onto the grid as a negative stain. The stain droplet was left for 30 seconds before the excess was similarly wicked away using filter paper. The grids were then allowed to fully dry for a minimum of 3 hours before Bright-field TEM imaging

was conducted using an FEI Tecnai 12 TWIN Transmission Electron Microscope with an EMSIS MegaView G3 (CCD). Images as presented have been cropped for clarity.

A.1.3 Fitting of the titration curve

For simplicity, here C12VVEE is denoted as H2A, a diprotonic acid. Besides, it can act as a base and undergoes a hydrolysis reaction due to the existence of the amine group. Hence, the acid-base equilibrium of H2A is given by the following chemical equations:

$$\mathrm{H_2A} + \mathrm{H_2O} \rightleftharpoons \mathrm{H_3A^+} + \mathrm{OH^-} \qquad K_b \tag{A.1}$$

$$\mathrm{H_2A} \rightleftharpoons \mathrm{HA^-} + \mathrm{H^+} \qquad K_{a_1} \tag{A.2}$$

$$\mathrm{HA^-} \rightleftharpoons \mathrm{A^{2-}} + \mathrm{H^+} \qquad K_{a_2} \tag{A.3}$$

Here, Kb is the chemical equilibrium constant for the hydrolysis reaction. It is required that

$$\frac{K_w}{K_b} > K_{a_1} > K_{a_2}$$

to avoid self acid-base reactions, which is later adopted in our fitting. The dissociation constant of water, Kw, is assumed to be a constant of $10^{-}14$.

Let $w = [\mathrm{H_3A^+}]$, $x = [\mathrm{H_2A}]$, $y = [\mathrm{HA^-}]$, $z = [\mathrm{A^{2-}}]$. Here, [...] represents the concentration of each species in the solution. From Eq. (A.1), (A.2), (A.3), we have

$$x = \frac{wK_w}{[\mathrm{H_3A^+}]\,K_b} \tag{A.4}$$

$$y = \frac{wK_wK_{a_1}}{[\mathrm{H^+}]^2 K_b} \tag{A.5}$$

$$z = \frac{wK_wK_{a_1}K_{a_2}}{[\mathrm{H^+}]^3 K_b} \tag{A.6}$$

For the titration, let c_0 and V_0 be the concentration and the volume of the original acid solution, respectively, c_B and V_B be the concentration and the added volume of NaOH used for the titration. Let c_A be the total concentration of $\mathrm{H_2A}$ and its derivatives. In our work, c_0 = 2.5 mM, V_0 = 5 mL, c_B = 0.1 M. The charge equilibrium and the material equilibrium give

$$\left[\mathrm{H_3A^+}\right] + \left[\mathrm{H^+}\right] + \left[\mathrm{Na^+}\right] = \left[\mathrm{HA^-}\right] + 2\left[\mathrm{A^{2-}}\right] + \left[\mathrm{OH^-}\right] \tag{A.7}$$

$$\left[\mathrm{H_3A^+}\right] + [\mathrm{H_2A}] + \left[\mathrm{HA^-}\right] + \left[\mathrm{A^{2-}}\right] = c_A \tag{A.8}$$

where

$$c_A = \frac{c_0V_0}{V_B + V_0}$$

$$\left[\mathrm{Na^+}\right] = \frac{c_BV_B}{V_B + V_0}$$

By substituting Eq. (A.4), (A.5), (A.6) into Eq. (A.7), (A.8), we obtain 2 equations for variables w and p

$$w + \left[\mathrm{H}^+\right] + \frac{c_B V_B}{V_B + V_0} = \frac{K_w}{[\mathrm{H}^+]} + \frac{w K_w K_{a_1}}{[\mathrm{H}^+]^2 K_b} + 2\frac{w K_w K_{a_1} K_{a_2}}{[\mathrm{H}^+]^3 K_b} \tag{A.9}$$

$$w + \frac{w K_w}{[\mathrm{H}^+] K_b} + \frac{w K_w K_{a_1}}{[\mathrm{H}^+]^2 K_b} + \frac{w K_w K_{a_1} K_{a_2}}{[\mathrm{H}^+]^3 K_b} = \frac{c_0 V_0}{V_B + V_0} \tag{A.10}$$

which allow us to solve $[\mathrm{H}^+]$, hence pH, as a function of V_B. The same procedure was adopted for the titration with HCl, shown in the titration plot with negative V_B. Using Mathematica, we tune K_b,K_{a_1}, and K_{a_2} to find the best fit of the experimental titration curve.

A.1.4 Atomistic Simulations

All simulations in this study were performed with GROMACS 2021.5[26], an MD package mainly designed for simulations of large biomolecules. The CHARMM36[27] force field was used for all-atom simulations. The recommended CHARMM TIP3P water model was applied with the structures constrained using the SETTLE algorithm[28]. All visual analyses were performed with VMD[29] and MDAnalysis[139].

The PA molecule is initialized with Avogadro[31] and Packmol[32]. On the x-y plane, 9 PAs were distributed radially with an angle of 40° between each other to form the first layer. The second layer of 9 PAs was placed 0.5 nm above the first layer with a 20° shift. A total of 18 layers were created to initialize the fiber[33]. The fiber was solvated in water with 0.1 M of ions except for the counterions. The initial structure is shown in Fig. 1 in the main text. For the fiber system, the potential energy was first minimized using the steepest descent algorithm for 10000 steps with a time step of 1 fs and a tolerance of 1000 N. A subsequent NVT ensemble (constant number of particles, volume, and temperature) equilibration of 1 ps was performed. Position restraints were

placed on the C12 hydrocarbon tail. Subsequently, the NPT ensemble (constant number of particles, pressure, and temperature) was applied for 4 sequent equilibrations of 5 ns each using the time step of 2 fs. For each NPT ensemble equilibration, the position restraint force constant decreases (1000 kJ/mol, 600 kJ/mol, 300 kJ/mol, and 0) to fully relax the structure. The pressure was coupled semi-isotropically in the x-y plane and the z direction separately. Subsequently, long MD production simulations were performed. Periodic boundary conditions were applied in all three dimensions. Neighbor searching was performed up to a cut-off distance of 1.2 nm by means of the Verlet particle-based approach and was updated every 20 timesteps. The potential-switch method was applied for the short-range Lennard-Jones (LJ) 12-6 interactions from 1 nm to 1.2 nm. The short-range electrostatic interactions were calculated up to 1.2 nm, and the long-range electrostatic interactions were calculated by means of the Particle Mesh Ewald algorithm. A time step of 2.5 fs was employed byconstraining all the covalent bonds using the LINCS algorithm in the water system. The temperatures of the fiber solute and the solvent molecules were separately coupled using the Nosé-Hover algorithm (reference temperature 298 K, characteristic time 1 ps). The semi-isotropic Parrinello-Rahman barostat was utilized with the reference pressure of 1 bar, the characteristic time of 4 ps, and the compressibility of $4.5 \times 10^{-5} mathrmbar^{-1}$ in x-y plane, and z direction. Each simulation ran for 200 ns. The final simulation snapshots are shown in Fig. 2 in the main text. Same procedures were performed for C16-VVEE PA systems.

A.1.5 Coarse-grained Simulations

GROMACS 2021.5 and MARTINI 3 force field[34] were combined for coarse-grained simulation. The details of the PA bead mapping are provided in Fig. S3. We solvated 150 PAs in an aqueous solution at 0.1M NaCl salt concentration in addition to PAs counterions in a $9 \times 9 \times 9\mathrm{nm}^3$ box. The potential energy was first minimized using the steepest descent algorithm for 5000 steps.

An NVT ensemble equilibration was performed for 1000 steps with a timestep of 10 fs. The v-rescale thermostat was utilized to keep the temperature constant. Subsequently, an NPT ensemble equilibration was carried out for 1000 steps with a timestep of 20 fs. The v-rescale thermostat and Berendsen barostat were utilized. Finally, a long MD production run was performed for 50,000,000 steps with a timestep of 20 fs (total for 1 μs). Neighbor searching was performed up to a cut-off distance of 1.2 nm by means of the Verlet particle-based approach and was updated every 20 timesteps. The potential-shift method was applied for the short-range Lennard-Jones (LJ) 12-6 interactions at a cut-off of 1.1 nm. The reaction-field type Coulombic interaction was adopted with a Coulombic distance of 1.1 nm. The dielectric constant was set to infinity beyond that distance. The temperature of the PAs and solvent/ion molecules were separately coupled using the v-rescale algorithm (reference temperature 298 K, characteristic time 1 ps). The isotropic Parrinello-Rahman barostat was utilized with the reference pressure of 1 bar, the characteristic time of 12 ps, and the compressibility of $3 \times 10^{-4}\mathrm{bar}^{-1}$ in all directions. The final snapshots are given in Fig. 4 in the main text.

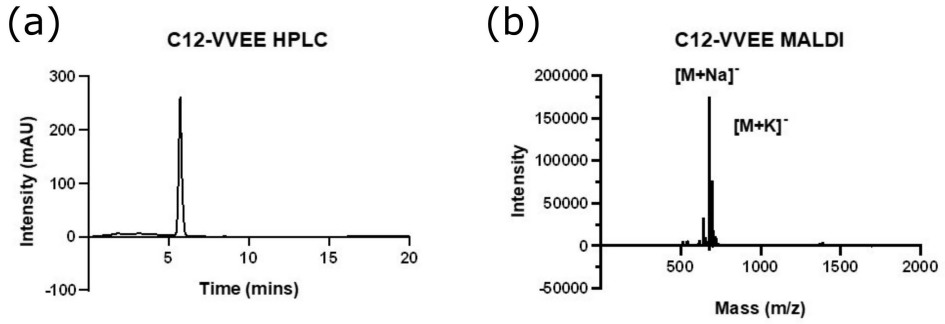

Figure A.1: Analytical RP-HPLC chromatogram (a) and MALDI-TOF mass spectra (b) for C12-VVEE (MW:655.4).

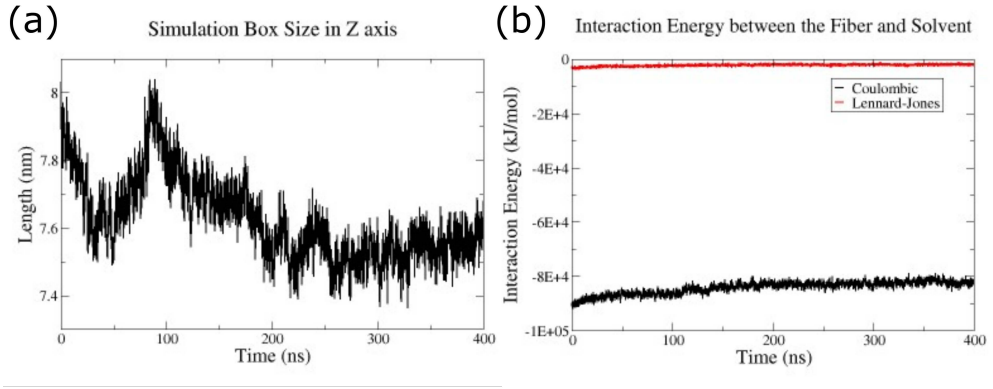

Figure A.2: Simulation results of C_{12}-VVEE fiber. (a) The length of the simulation box Z axis. (b) The interaction energy between the fiber and the solvent. The convergence of both Z length and energies indicates the equilibrium of the fiber simulation.

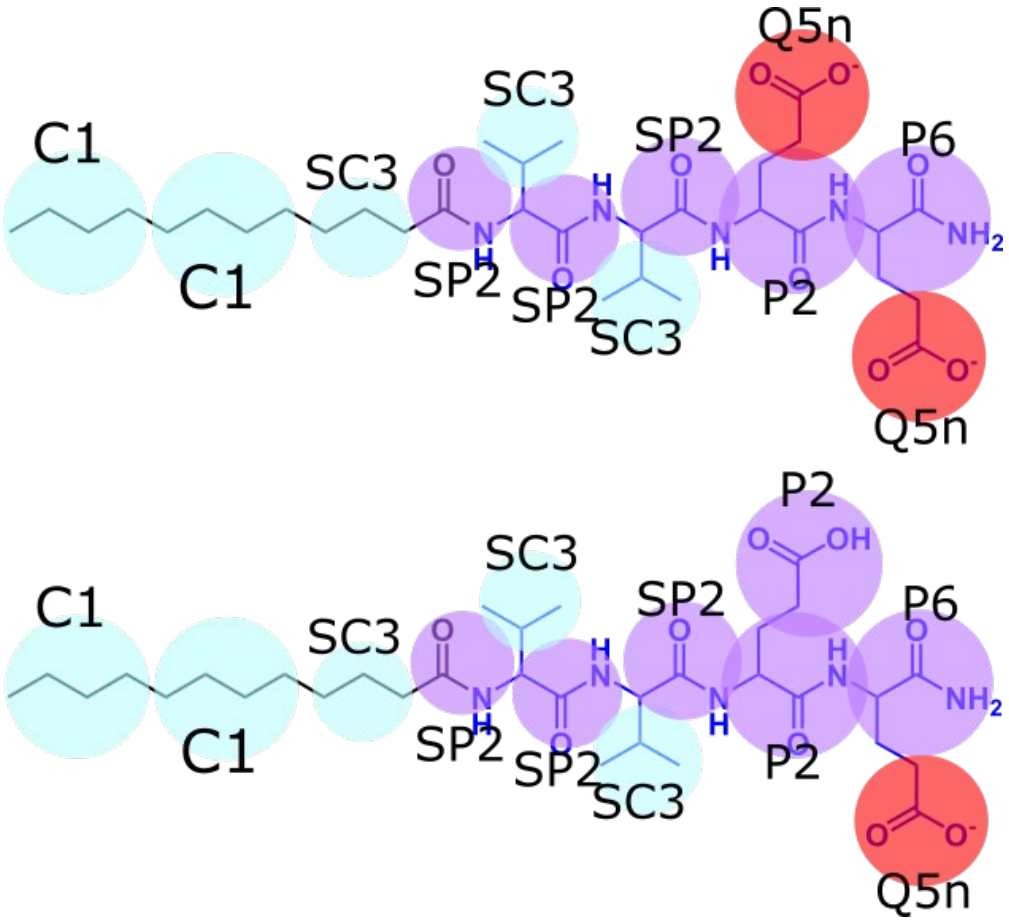

Figure A.3: The MARTINI 3 mapping of the PA molecules. The only difference between the half-protonated PA molecules and the fully deprotonated molecules is the bead type of the inner GLU carboxylic group. Cyan stands for hydrophobic beads, purple for hydrophilic beads, and red for charged beads.

A.2 Microscopically segregated ligand distribution in co-assembled peptide-amphiphile nanofibers

A.2.1 Simulation details

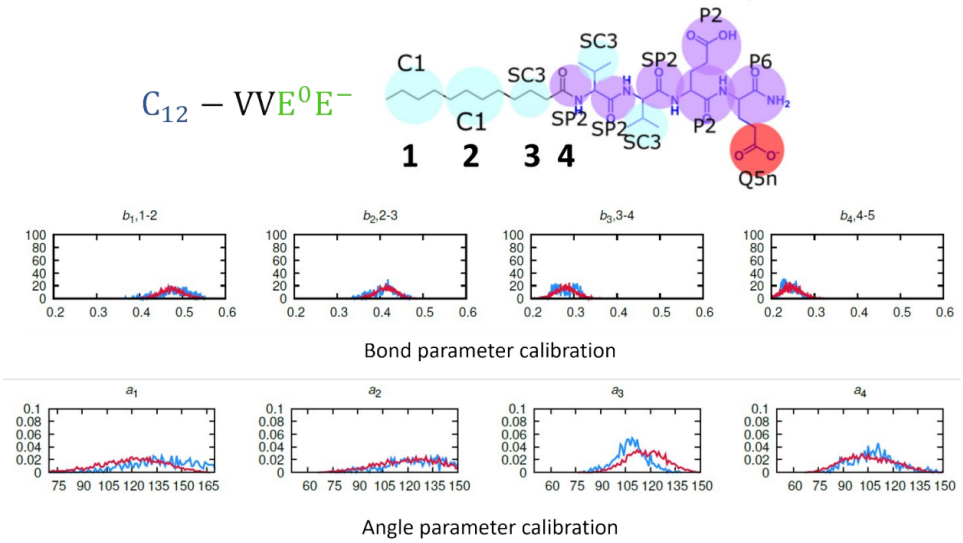

Figure A.4: Definition of Martini3 beads of $C_1$2VVEE and parameter calibrations.

As non-amino acid parameters are not provided by martini3[34] or martinize2[75], we followed the small molecule modeling techniques for bead definitions[74]. As bond angle parameters are not provided for C12, we have performed simulations to iteratively adjust the bond distance, bond strength, angle, and angle strength by following martini3 parameterizing-small-molecules tutorial. In Figure S1, we are showing the bond and angle distribution where the blue curves show the all-atom distribution and red curve show our coarse-grain distribution. Our surface accessible surface area was also in between 8% of the all-atom value. Z33 is made of 33 amino acids which forms a double alpha helix structure. We used martinize2[75] to directly get bead definitions, bond, angle, dihedral and constrain parameters. All-atom to Martini3 mapping is shown in Figure S2.

The chemical structure and single letter description of Z33 is also shown. The hydrophobic amino acids are indicated with green letters.

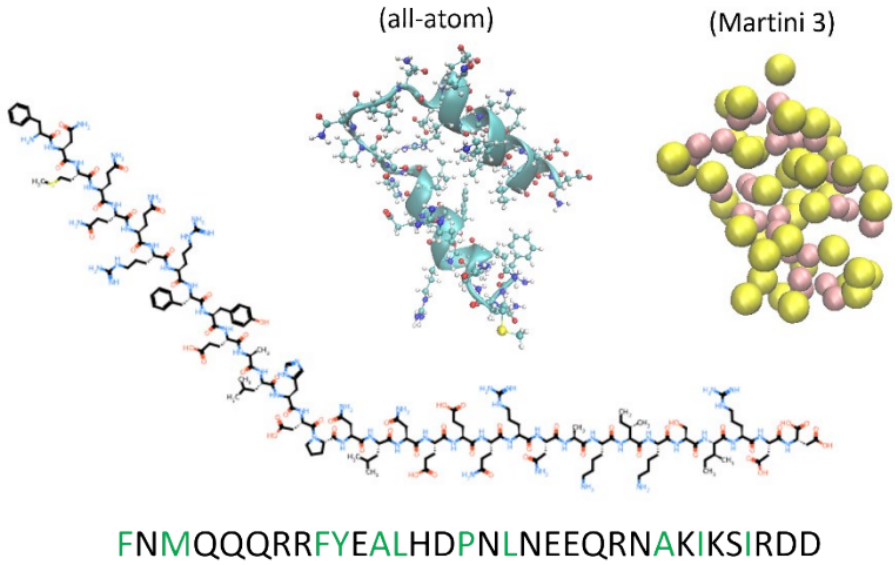

Figure A.5: Definition of Z33 and its chemical structure. All-atom and Martini 3 depiction of Z33 is also shown.

In Martini3 simulations, the potential energy was first minimized using the steepest descent algorithm for 5000 steps. An NVT ensemble equilibration was performed for 1000 steps with a timestep of 10 fs. The vrescale thermostat was utilized to keep the temperature constant. Subsequently, an NPT ensemble equilibration was carried out for 1000 steps with a timestep of 10 fs. The v-rescale thermostat and Berendsen barostat were utilized. Finally, a long MD production run was performed with a timestep of 20 fs until the co-assembly process is finished. Neighbor searching was performed up to a cut-off distance of 1.2 nm by means of the Verlet particle-based approach and was updated every 20 timesteps. The potential-shift method was applied for the short-range

Lennard-Jones (LJ) 12-6 interactions at a cut-off of 1.2nm. The Particle Mesh Ewald method was used for calculations of the non-bonded interactions between charge beads (cut-off 1.2 nm). The dielectric constant was fixed at 15. The bonds were constrained with the LINCS algorithm. The temperature of the PAs and solvent/ion molecules were separately coupled using the v-rescale algorithm (reference temperature 298 K, characteristic time 1 ps). The isotropic Parrinello-Rahman barostat was utilized with the reference pressure of 1 bar, the characteristic time of 12 ps, and the compressibility of 4.5 $\times$ 10-4 bar-1 in all directions. After initial coassembly, isotropic barostat is changed into semi-isotropic along the fiber axial direction. Periodic boundary conditions were applied in all three dimensions. We run simulations for 10μs after the co-assembly process is completed and analyzed last 3μs data. As Martini3 is not an all-atom model, the dynamics is fast, so we are assuming we have performed enough production run. We have also checked how the number-average cluster size changed with time for the simulation with a ligand-filler ratio of 1/5 (no salt), as this should be most crowded. The number-average cluster size is defined as

$$CSN = \frac{\sum N \times M}{\sum M}$$

where N is the cluster size and M is the concentration of the cluster. We can see from Figure S3, CSN reduces quickly in few hundred ns, probably breaking up micelles which were created during the co-assembly process.

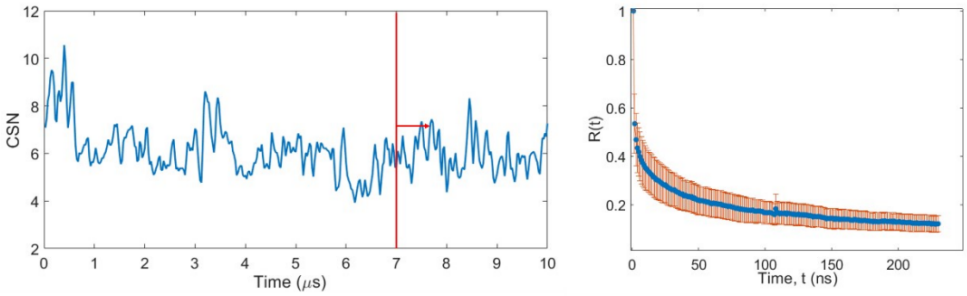

Figure A.6: (left) CSN variation with time for the simulation of a ligand-filler ratio of 1/5, with no salt. (right) Residence time correlation function for the equilibrated system.

To check if the system is equilibrated and peptides are not stuck in a local minimum, we have calculated the residence time correlation function for inner Valine (SP2 bead) of simulations with ligand-filler ratio of 1/5 (no salt). The residence time correlation function is defined as

$$R(t) = \frac{1}{N} \sum_{i=1}^{N} \theta_i(t_0)\theta_i(t_0 + t)$$

Here θ_i is the Heaviside unit step function (if one Valine SP2 bead i resides inside the first solvation shell of another Valine SP2 bead, $\theta_i = 1$; otherwise, $\theta_i = 0$), N is the number of SP2 beads in the first solvation shell and t_0 is the initial time step. We used the inner Valine as it should be the least mobile among other peptide groups. This residence time is averaged for all beads and over 50 different initial time steps after equilibration. Error bar is obtained from 3 different simulations. $R(t)$ indicates how long the beads stay together. A larger $R(t)$ with time indicates that beads are hardly diffusing and probably stuck in a local environment. For our case, we can see that $R(t)$ values go below in $1/e$ few nanoseconds, which indicates that our peptides in the fiber are vary mobile and not stuck in a local minimum. This also says that our production period of 3 μs is more

than enough to sampling the equilibrated system.

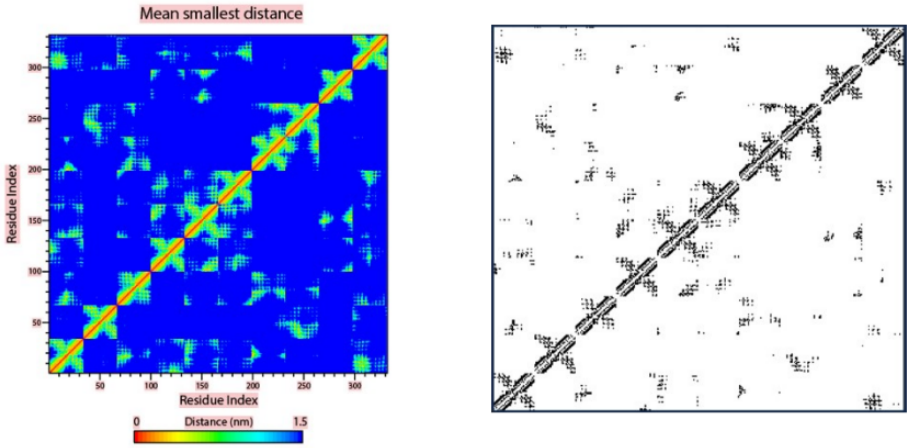

Figure A.7: A visual representation of the contact map matrix for 10 amino acids in all-atom simulation. Both shows the same matrix values but with different color scheme. Different color represents different minimum distance among amino acid residues.

We have performed the martini bulk simulation for 5μs after the initial formation of large aggregates and the full 5μs data was used as production run. All the simulation procedures remain same for Martini3 case. For all-atom, the potential energy was first minimized using the steepest descent algorithm for 10000 steps with a time step of 1 fs and a tolerance of 1000 N. A subsequent NVT ensemble equilibration of 1 ps was performed. Then, the NPT ensemble was applied for 4 sequent equilibrations of 5 ns each using the time step of 2 fs. For each NPT ensemble equilibration, the position restraint force constant decreases (1000 kJ/mol, 600 kJ/mol, 300 kJ/mol, and 0) to fully relax the structure. The pressure was coupled isotopically. Periodic boundary conditions were applied in all three dimensions. Neighbor searching was performed up to a cut-off distance of 1.2 nm by means of the Verlet particle-based approach and was updated every 20 timesteps. The

potential-switch method was applied for the shortrange Lennard-Jones(LJ) 12-6 interactionsfrom 1 nm to 1.2 nm. The short-range electrostatic interactions were calculated up to 1.2 nm, and the long-range electrostatic interactions were calculated by means of the Particle Mesh Ewald algorithm. A time step of 2.5 fs was employed by constraining all the covalent bonds in amino acid using the LINCS algorithm. We have performed the production period for 2μs in allatom simulations after initial aggregate formation.

We have used VMD contact map plugin to calculate nearest neighbor number. This analysis provides a contact map for all the amino acids present in the simulation system. In Figure S4, we are showing a graphical representation of the contact map matrix for all-atom bulk simulation, no salt case. This matrix provides the shortest distance between all amino acid residues, and we have used a cut-off 0.7 nm to calculate the nearest neighbor.

A.2.2 Co-assembly of similarly charged ligands and fillers.

Figure S5(a) shows the destabilized region in the fiber with negatively charged fillers andnegatively charged ligands. We did not observe a breakout of micelles from the fiber during our totalsimulation time. In Figure S5(b), we show the difference between positive (upper panel) and negative (lower panel) ligands co-assembling into an already formed fiber of negative fillers. It is obvious from the snapshots that, all the positive ligands enter the fiber in 1μs. But only a fraction of negative ligands enters the fiber.

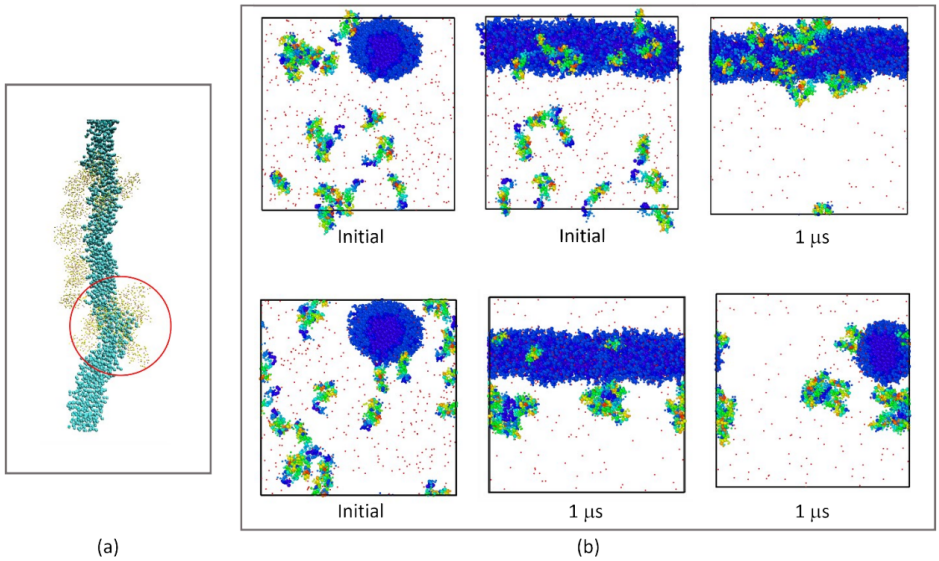

Figure A.8: (a) A destabilized region in fiber where negative ligands are crowding. (b) Initial and final snapshots of the simulation systems where we tried to observe how many of the positively charged (upper panel) and negative charged (lower panel) enter a negatively charged fiber.

A.3 Crosslinks and self-loops between IgG and nanofibers

A.3.1 Diffusion coefficients of rod-like nanofiber and IgG

The diffusion coefficient of IgG and nanofiber is calculated with Stokes-Einstein-Sutherland equation and rod-like macromolecule diffusion equation respectively[77,78].

$$D = \frac{k_B T}{6\pi\eta r} \tag{A.11}$$

$$3\pi\eta_0 L D_t / k_B T = \ln p + v \tag{A.12}$$

where η is the viscosity of the solution, r is the radius of the sphere, L is the rod length, p is the ratio of rod length and diameter, v is the end-effect corrections, which is the average of lengthwise $v_\parallel$ and the sidewise $v_\perp$ correction.

$$v_\parallel = -0.114 - 0.15/\log 2p - 13.5/\log 2p^2 + 37/\log 2p^3 - 22/\log 2p^4 \tag{A.13}$$

$$v_\perp = 0.866 - 0.15/\log 2p - 8.1/\log 2p^2 + 18/\log 2p^3 - 9/\log 2p^4 \tag{A.14}$$

In MD simulations, the diffusion coefficient can be calculated with mean squared displacement (MSD),

$$\left\langle (x(t) - x_0)^2 \right\rangle = 2D\tau \tag{A.15}$$

A.3.2 Coarse grained model beads definition and geometry

The coarse grained models for the fiber and IgG are shown below (**Fig. A.9a**). The fiber is modeled as a rigid rod, with a diameter of 7 nm. The filler and ligand beads do not participate in interaction except hard core repulsion. The ratio of filler:ligand is 10:1. Each ligand bead is connected with a Z33 bead via a flexible bond as the linker in the all-atom model. The IgG is a Y-shaped molecule. For simplicity, IgG is modeled as a rigid molecule. Each Fab/Fc domain is modeled as a single bead connected to a center bead. The center bead and Fab bead do not interaction except hard core repulsion. Each bead has a van der Waals radius of 5.1 nm and the radius of gyration of the IgG is 14 nm. The Fc bead has 2 binding site, which form a $3/4\pi$ angle with the Fc bead to correctly represent the geometry when IgG bind with 2 Z33. The binding between Fc and Z33 beads are modeled as a bond-formation reaction. A bond forms once the beads diffuse within a cutoff distance (the high affinity between Z33 and IgG). Due to the computational cost, the fiber is modeled with a length of 200 nm.

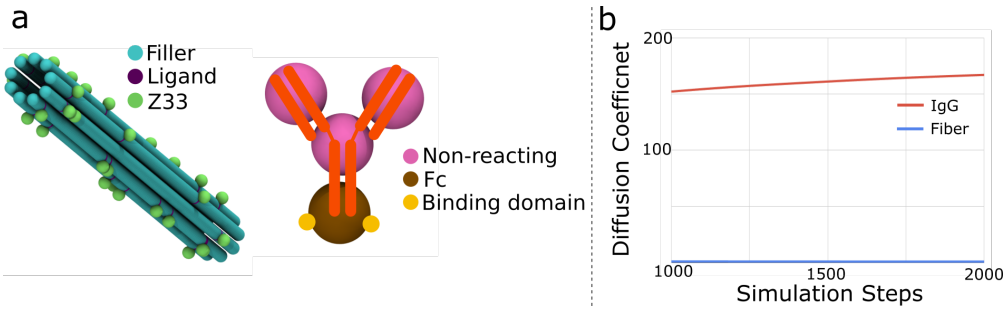

Figure A.9: (a) The coarse grained models of fibers and IgG. (b) Benchmark of the diffusion coefficients of fibers and IgG.

A.3.3 System setup and simulation

LAMMPS 2023.11 is used for the simulation. The simulation is performed in reduced units, with a unit length $\sigma = 7nm$, a unit energy $e = 1k_BT = 2.5kJ/mol$, a unit mass $m = 600g/mol$. The unit time τ can be calculated as

$$\tau = \sqrt{m * \sigma^2/e} = 1.0 \times 10^{-10}s = 0.1ns \tag{A.16}$$

The system contains 108 fibers and 6480 IgG in a $630 \times 630 \times 630nm^3$ box ($2.5mM$ of fillers, $250\mu M$ of ligands and $40\mu M$ of IgG). The system was first energy minimized, followed by a production run. The production run was performed under the NVE ensemble (constant number of particles, constant volume, and constant energy) with Langevin dynamics. The fibers and IgG are coupled separately. The Langevin damping coefficients are benchmarked such that the ratio corresponding diffusion coefficients is $D_{fiber}/D_{IgG} = 1/100$ (**Fig. A.9b**). The simulation is run for $10^7\tau$. The number of loops and bridges are analyzed with an in-house python program.

APPENDIX B

POLY(PROPYLENE SULFONE) SUPERSTRUCTURES AS PROTEIN ANCHORS

B.1 Controlled adsorption of multiple bioactive proteins enables targeted mast cell nanotherapy

B.1.1 Methods

Chemicals and materials. All chemical reagents were purchased from Sigma-Aldrich and were used without further purification unless otherwise indicated. Antibodies were acquired from BioLegend. Pooled human plasma was used after nanofiltration (100 nm). Recombinant A. victoria GFP protein (from the Jewett Lab). Goat Anti-Mouse IgG (10nm Gold, Abcam) was used for immunogold labelling.

Dynamic light scattering (DLS). Size distribution and zeta potential of NPs were analyzed by Zetasizer Nano (Malvern Instruments) with a 4 mW He-Ne 633 nm laser at 22 °C. The polydispersity index (PDI) was calculated using a two-parameter fit to the DLS correlation data.

Transmission electron microscopy (TEM). Formvar carbon film copper grids (400 mesh, Electron Microscopy Sciences, Inc.) were used immediately after glow-discharging (25 W, 20 s). Samples were applied to the grids, followed by negative staining (1.5% uranyl formate, two times). Excess stained was removed by blotting each sample with Whatman filter paper. TEM images were acquired on a JOEL 1400 Transmission Electron Microscope operating at 120 kV. Any further image processing conducted on the aligned frames was completed in ImageJ.

Cryo-transmission electron microscopy (cryo-TEM). Samples were prepared by applying 3 μL of suspension on pretreated holey lacey carbon 400 mesh TEM copper grids (Electron Microscopy

Sciences). Following a blot of 3 s, samples were plunge-frozen (Gatan Cryoplunge 3 freezer). Images of samples entrapped in vitreous ice were acquired using a field emission transmission electron microscope (JEOL 3200FS) operating at 300 keV. Digital Micrograph software (Gatan) was used to align the individual frames of each micrograph to compensate for stage and beam-induced drift. Any further image processing conducted on the aligned frames was completed in ImageJ.

Fluorescence and UV-Visible spectroscopy. Fluorescence spectra were recorded by RF-6000 using LabSolutions RF software. UV-Visible absorbance and transmittance were measured by Perkin Elmer LAMBDA 1050. **Protein quantification.** The concentrations of proteins were quantified by UV-Visible absorbance or fluorescence depending on protein type and equipment availability. NanoDrop Abs was used for testing trace samples.

All atom explicit solvent molecular dynamics simulations.

The analysis of the 6-chain $PPSU_{20}$ aggregate system was based on the simulations reported in our previous work[97]. For the 125-chain NP system, 125 $PPSU_{20}$ chains were distributed spherically with a vacancy in the center of the NP using PACKMOL[32]. The NP has an initial outer radius of 7.5 nm and an initial vacancy radius of 2.5 nm. For the 600-chain NP system, 600 $PPSU_{20}$ chains were distributed spherically with a vacancy in the center of the NP using PACKMOL. The NP has an initial outer radius of 8 nm and an initial vacancy radius of 4.5 nm. Each NP is dissolved in a water solvent box with a dimension of $20 \times 20 \times 20\mathrm{nm}^3$. For each NP-water system, the potential energy was first minimized using the steepest descent algorithm for 1,000 steps with a time step of 1 fs. A subsequent NVT ensemble (constant number of particles, volume, and temperature) equilibration of 1 ps was performed. Subsequently, the NPT ensemble (constant number of particles, pressure, and temperature) was applied for equilibration of 1 ns using the time step of 2 fs. Subsequently, long MD production simulations were performed. The periodic boundary

conditions were applied in all three dimensions. The neighbor searching was performed up to a cut-off distance of 1.2 nm utilizing the Verlet particle-based approach and was updated every 20 timesteps. The potential-switch method was applied for the short-range Lennard-Jones (LJ) 12-6 interactions from 1 nm to 1.2 nm. The short-range electrostatic interactions were calculated up to 1.2 nm, and the long-range electrostatic interactions were calculated employing the Particle Mesh Ewald algorithm[140]. A time step of 2.5 fs was employed by constraining all the covalent bonds using the LINCS algorithm[141]. The temperatures of the $PPSU_{20}$ solute and the solvent molecules were separately coupled using the Nosé-Hoover algorithm[142] (reference temperature 298 K, characteristic time 1 ps). The isotropic Parrinello-Rahman barostat[143] was utilized with the reference pressure of 1 bar, the characteristic time of 4 ps, and the compressibility of $4.5 \times 10^{-5}\mathrm{bar}^{-1}$. Each of the simulations run 200 ns. The final simulation snapshots are presented in Fig. 1b. The interaction energies were calculated with gmx energy integrated within the GROMACS 2021.5 package.

The structure of trypsin was downloaded from Protein Data Bank (www.rcsb.com) with the PDB ID of 1S0Q. After the simulation of 600-chain NP approached equilibrium, the simulation box was enlarged to $22 \times 22 \times 22\mathrm{nm}^3$. Subsequently, 6 trypsin molecules were solvated in the system, along with counter ions (60 Cl^-) to balance the charge of the 6 trypsin molecules. The trypsin molecules were distributed randomly and close to the NP surface. Energy minimization, NVT equilibration, NPT equilibration, and 200 ns MD production run were performed with the same simulation parameters aforementioned. Subsequently, the number of -SO_2- groups on the NP surface was counted. In this work, the -SO_2- groups that are within 2.5 Åof the water solvent molecules or protein molecules are considered as surface groups. The number of hydrogen bonds formed between trypsin and water was calculated with a criteria of $\theta_{\mathrm{HDA}} \leq 30^\circ$ and $r_{\mathrm{DA}} \leq 3.5$ Åbetween the hydrogen (H), donor (D), and acceptor (A)[144] The binding energy between trypsin

molecules and the NP was calculated with the *gmx energy* tool. The compositions of the trypsin binding domains were analyzed with our recently developed program Protein Surface Printer[145]. The results indicated there were no preference for binding orientations of trypsin.

The protein structure of Bovine Serum Albumin (BSA) was downloaded from Protein Data Bank with the PDB ID of 4F5S. After the simulation of 600-chain NP approached equilibrium, the simulation box was enlarged to 20 $\times$ 19 $\times$ 24 nm3. Subsequently, 2 molecules of BSA were solvated in the system, along with counter-ions (32 Na+) to neutralize the net charge of the system. The BSA molecules were distributed randomly in the simulation box. Energy minimization, NVT equilibration, NPT equilibration, and 200 ns MD production run were performed with the same simulation parameters aforementioned. During the simulation, one of the BSA molecules diffused slowly in solvent and was adsorbed onto the NP near the end of the simulation. Therefore, quantitative analysis was only carried out on the BSA that stably bound to the NP. The number of surface -SO_2- groups of the NP was counted in the similar manner as that in the NP-trypsin system. The number of hydrogen bonds formed between BSA and water was calculated using the same structural criteria as those in the NP-trypsin system. The binding energy between BSA and the NP was calculated with the gmx energy tool.

The structure of IgG1 human antibody was downloaded from Protein Data Bank with the PDB ID of 1IGY. For IgG1-PPSU complex system, 3 parallel simulation runs were performed. After the simulation of 600-chain NP approached equilibrium, the simulation box was enlarged to 30 $\times$ 30 $\times$ 30 nm3. Subsequently, 1 molecule of IgG was solvated in the system, along with counter-ions (20 Cl-) to neutralize the net charge of the system. The IgG1 molecules were distributed such that in the first simulation, the Fc domain was facing the PPSU NP, in the second simulation, one of the Fab domains was facing PPSU NP, and in the last simulation, the IgG1 molecule lay flat on the PPSU NP surface. Energy minimization, NVT equilibration, NPT equilibration, and 200 ns MD

production run were performed with the same simulation parameters aforementioned. The number of surface -SO_2- groups of the NP was counted in the similar manner as that in the NPtrypsin system. The number of hydrogen bonds formed between IgG1 molecule and water was calculated using the same structural criteria as those in the NP-trypsin system. The binding energy between IgG1 and the NP was calculated with the gmx energy tool.

Dye adsorption. PPSU NPs were mixed and incubated with 1 wt.% of dye in water or in PBS at 23 °C for 5 min. They were centrifuged, and the NP pellet was washed by the buffer (water or PBS) for three times. All the supernatants were combined for quantitative fluorescence or absorbance analysis.

AMC fluorometric assay. Trypsin activity assay kit (Abcam; ab282916) was used to assess trypsin desorption and its displacement by BSA during the proteolysis. In this kit, trypsin cleaves a synthetic substrate thereby releasing a fluorophore (AMC), which can be easily quantified at Ex/Em = 380/460 nm. 100 μL of trypsin@NP (1 mg/mL of PPSU; 80 μg/mL of trypsin) was incubated with BSA (1 mg/mL) at 37 °C for 90 min. After the proteolysis, the suspension was centrifuged at 10,000 g for 5 min. 10 μL of supernatant was collected, and the pellet was resuspended using the remaining 90 μL of supernatant. Into each well of a 96-well clear plate, 10 μL of the supernatant, or the pellet suspension (or one of its dilutions), or blank PPSU NPs, or trypsin buffer was mixed with 85 μL of trypsin buffer. 5 μL of trypsin substrate (100-fold dilution of the original stock solution) was added (the total volume/well was 100 μL), followed by fluorescence measurement in kinetic mode for 90 min using a fluorescence microtiter plate reader.

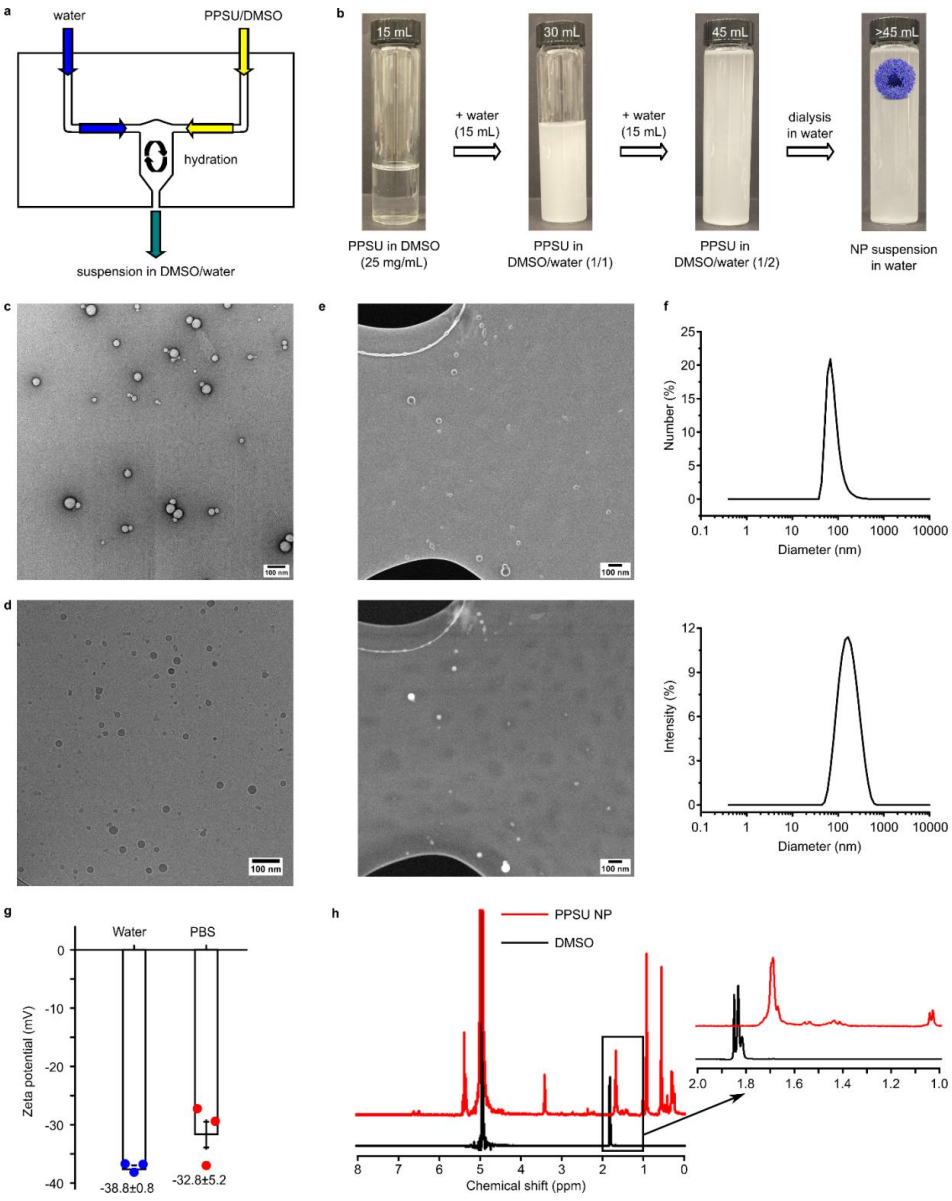

Figure B.1: Preparation and characterization of PPSU NPs. (a) Schematic illustration of the confined impingement jets mixer used for thorough hydration. (b) Typical process for the producing of PPSU NPs. (c) A representative TEM image of PPSU NPs in water (0.7 mg/mL). (d) A representative Cryo-TEM image of PPSU NPs in water (5 mg/mL). (e) Simultaneously recorded cryo-STEM (top) and cryo-SEM (below) images showing PPSU NPs (3 mg/mL in water) and their surfaces, respectively. (f) DLS size distribution of PPSU NPs by number (top) and intensity (below) in water (1 mg/mL). (g) Zeta potential of PPSU NPs measured in water and in phosphate buffered saline (PBS). Suspensions of PPSU NPs were prepared by mixing NPs in water with 10 vol.% of PBS (10×), followed by zeta potential measurements immediately. Data were obtained from 3 parallel samples (n = 3), and they are presented as mean values ± standard error. (h) Chemical degradation of PPSU NPs showing undetectable DMSO residual. The NPs were dialyzed in D2O instead of in H2O, then resuspended in D2O with 40 wt.% of NaOD for 1H NMR measurement. DMSO in D2O with 40 wt.% of NaOD was included as a control. Scale bar = 100 nm.

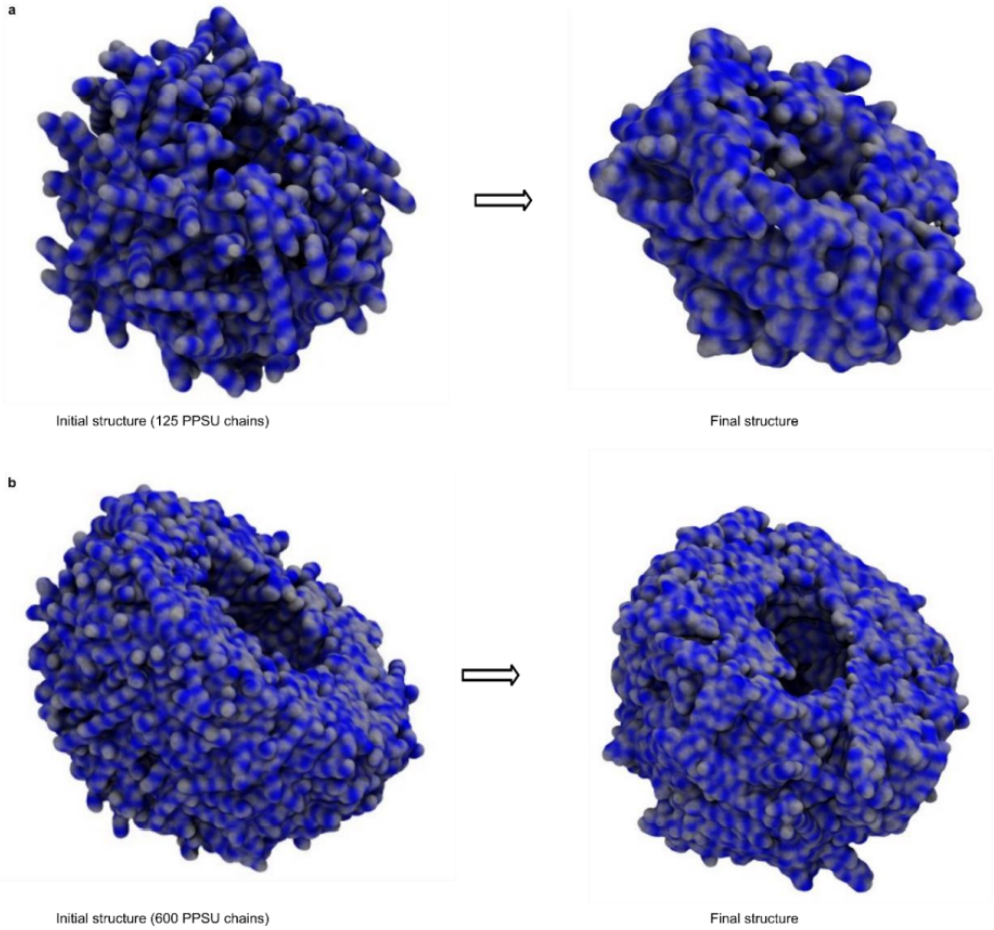

Figure B.2: Constructing hollow NPs in atomistic MD simulations. (a) The initial and the final structures of the 125-chain NP. (b) The initial and the final structures of the 600-chain NP. To illustrate the hollow structures, only around a half of the NPs is displayed in the snapshots. Blue: Oxygen and sulfur atoms; Grey: Carbon and hydrogen atoms. Water molecules are omitted for display.

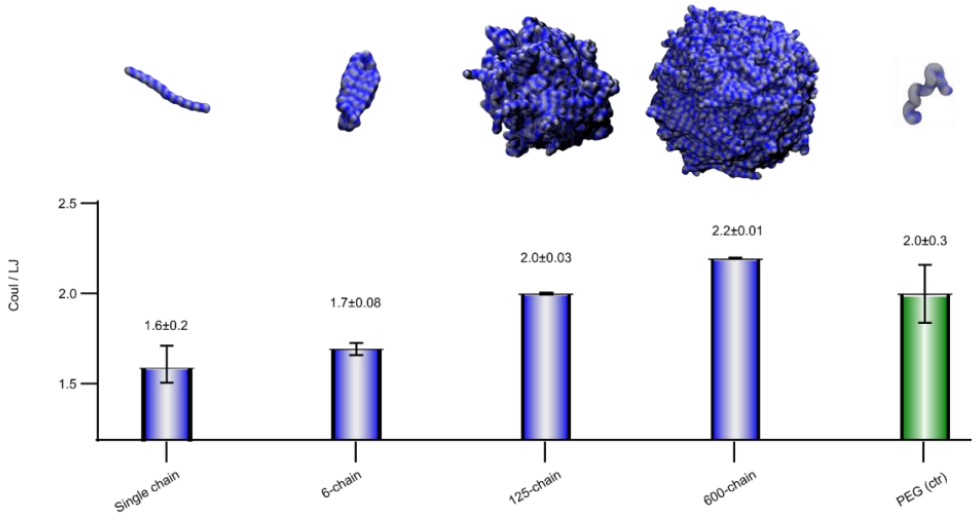

Figure B.3: Atomistic simulations demonstrating enhanced surface hydrophilicity as the size of the PPSU aggregate increases. Coulombic (Coul) and Lennard-Jones (LJ) interactions represent the polar and nonpolar interaction between PPSU and water, respectively. The Coul/LJ ratios are used to quantify surface hydrophilicity. A higher ratio stands for favored polar interactions, thus supporting an elevated hydrophilicity. PEG is included for comparison. The final simulation snapshots are shown correspondingly. The data are presented as mean values $\pm$ standard error from 100 ns to 200 ns (n = 1000).

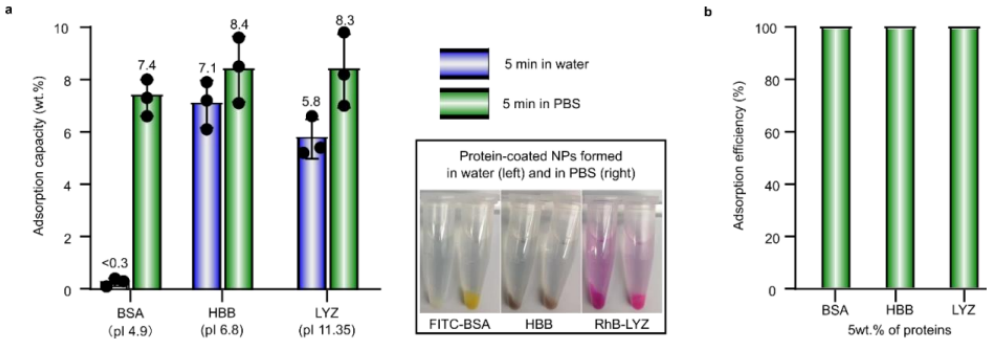

Figure B.4: Incubation of PPSU NPs with proteins in PBS leading to proteincoated NPs in 5 min. (a) While the adsorption of negatively charged proteins in water by PPSU NPs is inhibited by electrostatic repulsion, PPSU NPs can irreversibly adsorb nonspecific proteins in PBS. Bovine serum albumin (BSA), hemoglobin (HBB), and lysozyme (LYZ) were used without dye labelling. pI = distinct isoelectric point. The inset shows photos for protein-coated NPs after removing the excess proteins (BSA and LYZ were labelled with FITC and RhB, respectively). Data were obtained from 3 parallel experiments (n = 3), and they are presented as mean values $\pm$ standard error. (b) When incubated with 5wt.% of proteins in PBS, PPSU NPs adsorbed nearly 100% of the proteins.

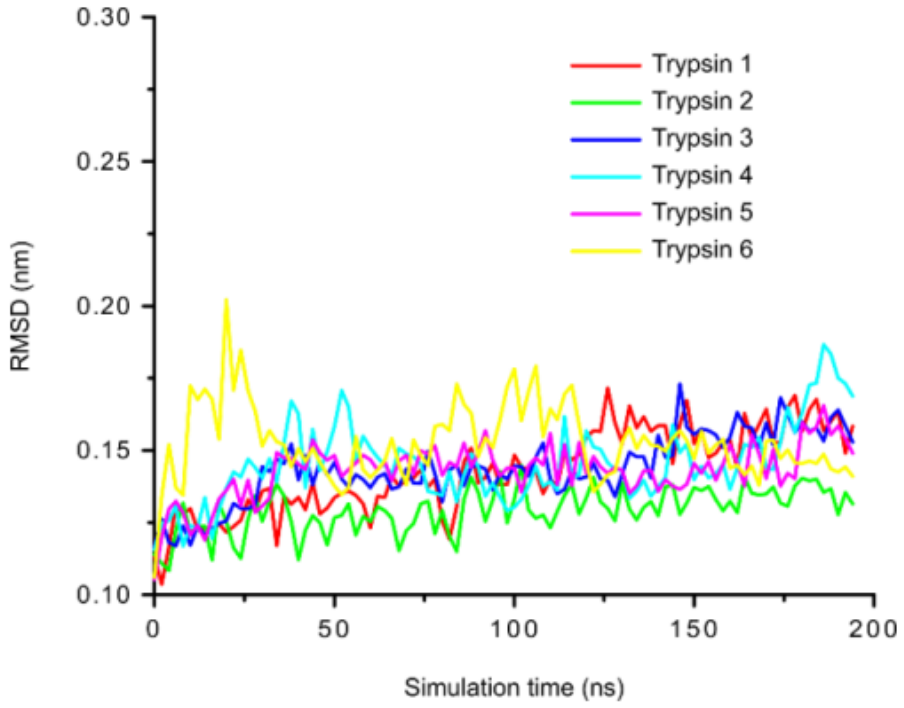

Figure B.5: The adsorbed trypsin molecules preserving their 3D structure after adsorption. The RMSD (root-mean-square deviation) of each trypsin molecule during the simulation. A small RMSD of around 1.5 Åsupports the retention of the trypsin structures.

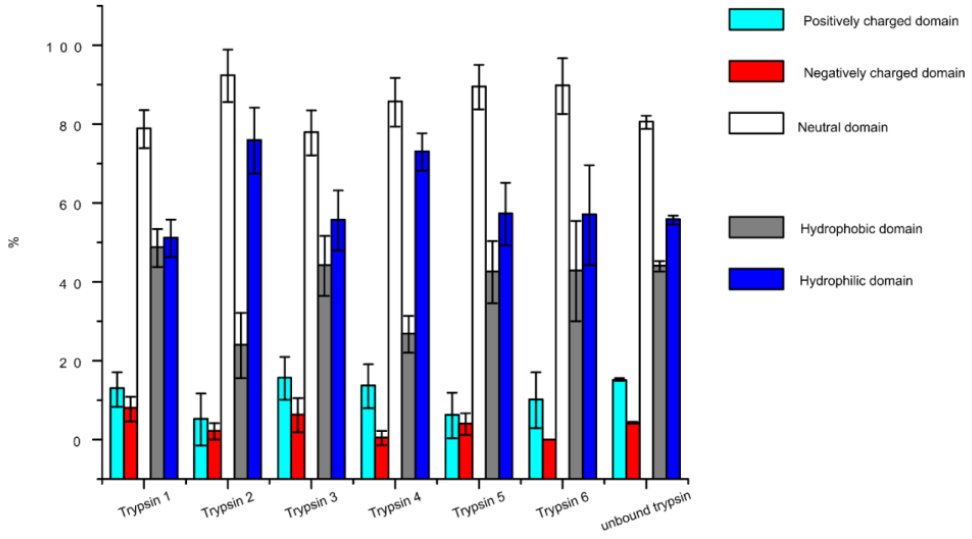

Figure B.6: Analysis of trypsin surface domain compositions in contact with PPSU NP. No remarkable difference was observed between the 6 adsorbed trypsin molecules and the unbound trypsin (control), indicating random and non-specific binding. The data are presented as mean values $\pm$ standard error from 52 ns to 196 ns (calculated every two nanoseconds; n = 73).

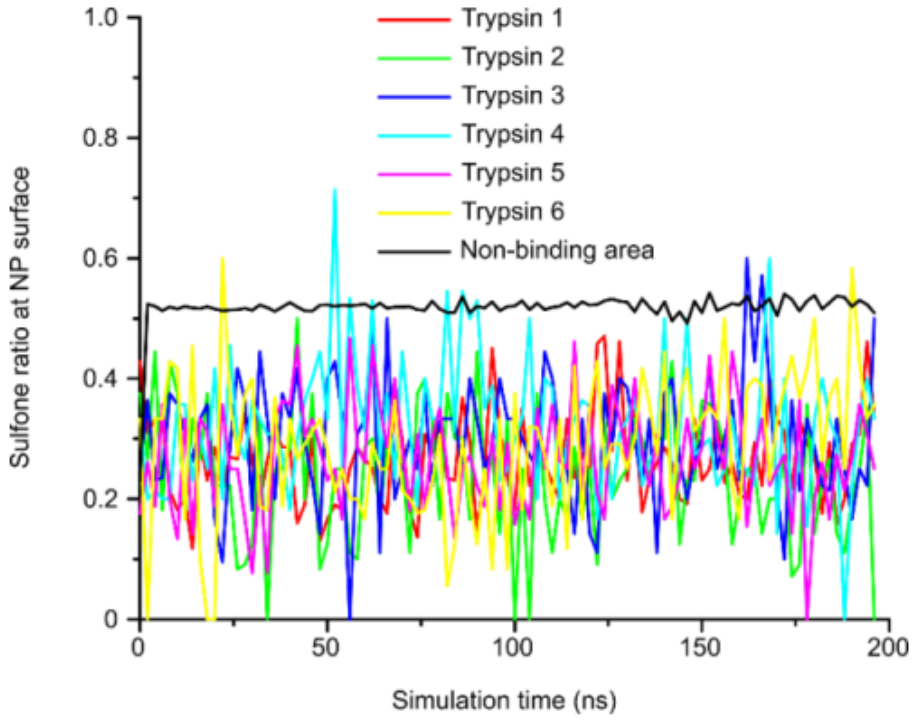

Figure B.7: Surface restructuring of the NP at the PPSU-trypsin interface upon trypsin adsorption. A decrease in the amount of polar sulfone groups at the trypsin-NP interface revealed enhanced surface hydrophobicity after trypsin adsorption.

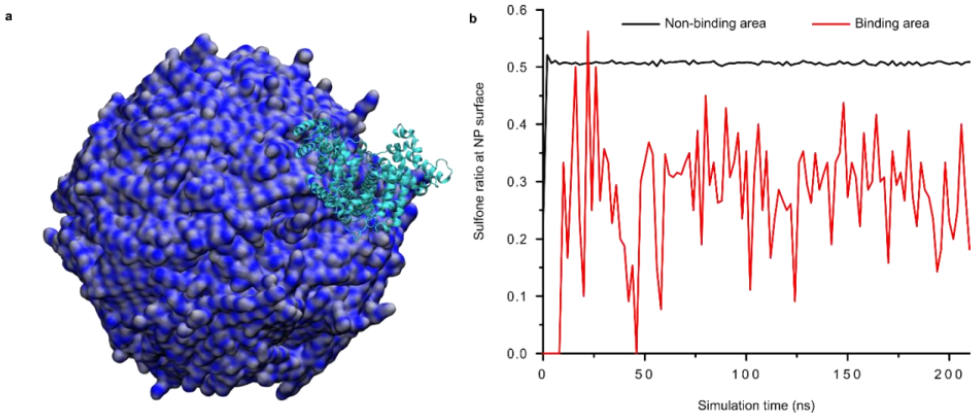

Figure B.8: Simulation results of BSA adsorption on to the 600-chain PPSU NP. (a) Atomistic simulation snapshot showing the adsorption of BSA (cyan) onto the surface of the 600-chain NP. (b) Quantitative calculation of the surface ratio of sulfone groups at the BSA-NP interface (within 2.5 Åof the BSA) revealing enhanced surface hydrophobicity after BSA adsorption.

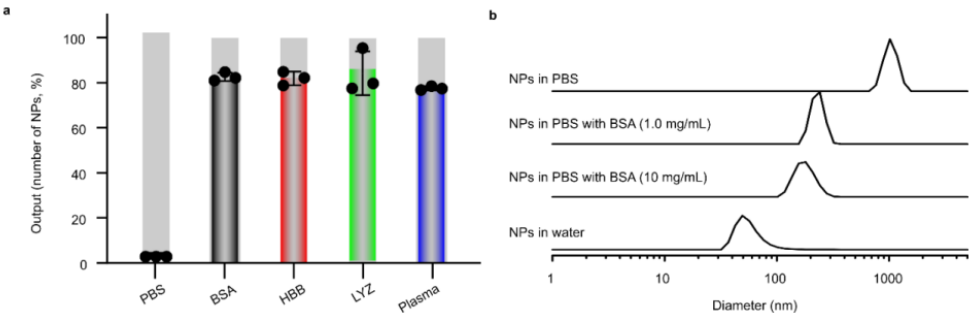

Figure B.9: Preparation of protein-coated NPs with improved colloidal stability in PBS. (a) PPSU NPs (5 mg/mL) were suspended in protein solution (10 mg/mL in PBS) or pooled human plasma for 5 min, followed by centrifugation and extensive washing to remove dynamically adsorbed proteins as well as residual proteins in solution. Output of protein-coated NPs (normalized to uncoated NPs in water) was measured by nanoparticle tracking analysis after extrusion (200 nm). Cluster formation of PPSU NPs in PBS without protein is included for comparison. Data were obtained from 3 parallel experiments (n = 3), and they are presented as mean values ± standard error. (b) DLS size distribution analysis of 1 mg/mL of PPSU NPs in PBS with different concentrations of BSA.

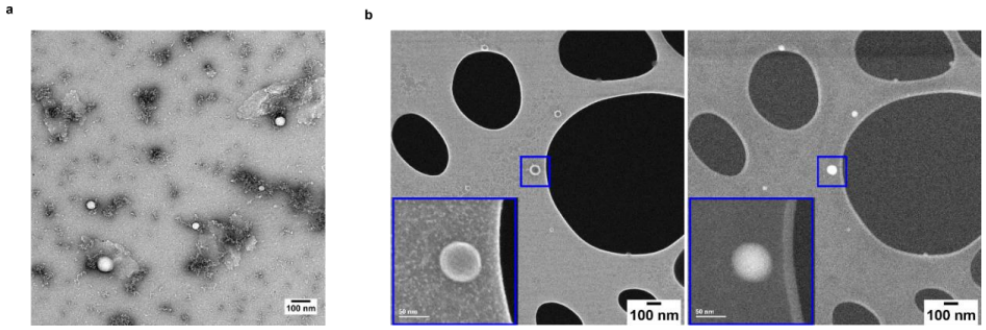

Figure B.10: Imaging BSA-coated NPs by TEM and cryo-STEM. (a) A representative TEM image showing BSA@NP in water with 10 mg/mL of BSA. (b) Simultaneously recorded cryo-STEM (left) and cryo-SEM (right) images showing BSA@NP and it surface in PBS. Scale bar in inset, 50 nm.

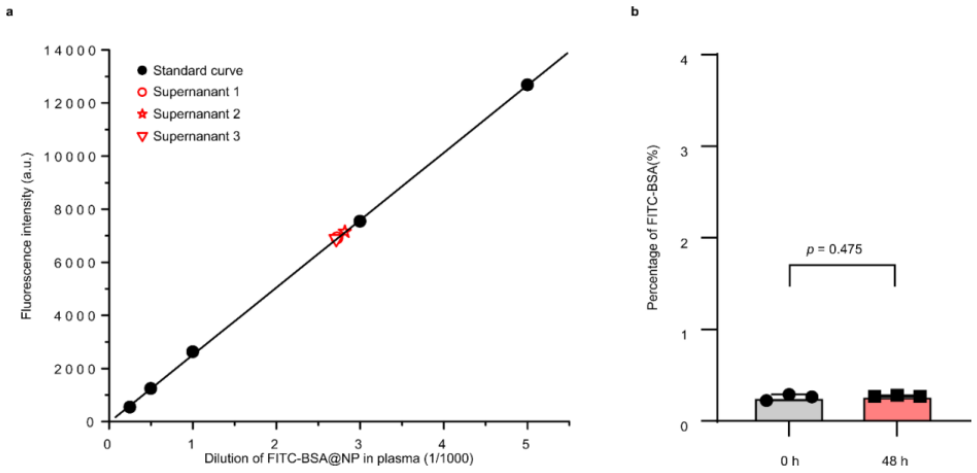

Figure B.11: Negligible displacement of FITC-BSA by other serum proteins in pooled human plasma even without considering the FITC-BSA@NP residual in the supernatants. (a) Fluorescence detection of FITC-BSA in the supernatants after incubating FITCBSA@NP in pooled human plasma at 37 °C for 48 h. (b) There were no significant differences for the 48-h incubation and 0-h incubation (washing) mixtures. Data are presented as mean values ± standard error. Statistical significance was determined by two-sample t-test for three parallel samples (n = 3).

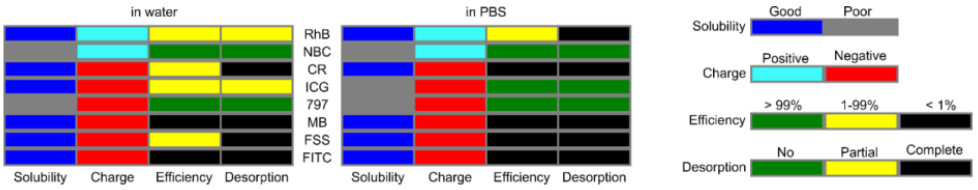

Figure B.12: Summary of dye adsorption (5-min incubation) by PPSU NPs in water and phosphate buffered saline (PBS). RhB = rhodamine B, NBC = Nile blue chloride, CR = cresol red, ICG = indocyanine green, 797 = NIR-797 isothiocyanate, MB = methyl blue, FSS = fluorescein sodium salt, FITC = fluorescein isothiocyanate. Desorption was assessed by three times of washing steps.

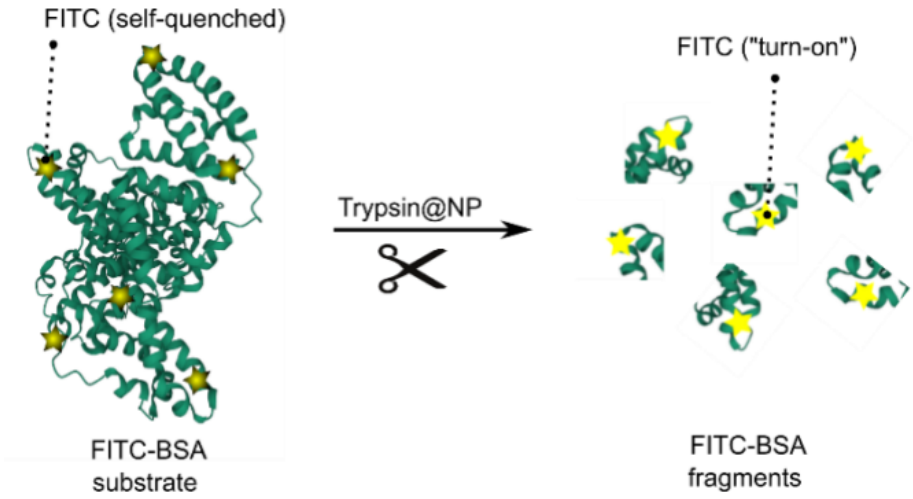

Figure B.13: Schematic illustration of the fluorescence-based kinetic assay for exploring the activity of irreversibly adsorbed trypsin (trypsin@NP). The fluorescence of FITC is self-quenched on BSA and will be recovered upon trypsin proteolysis.

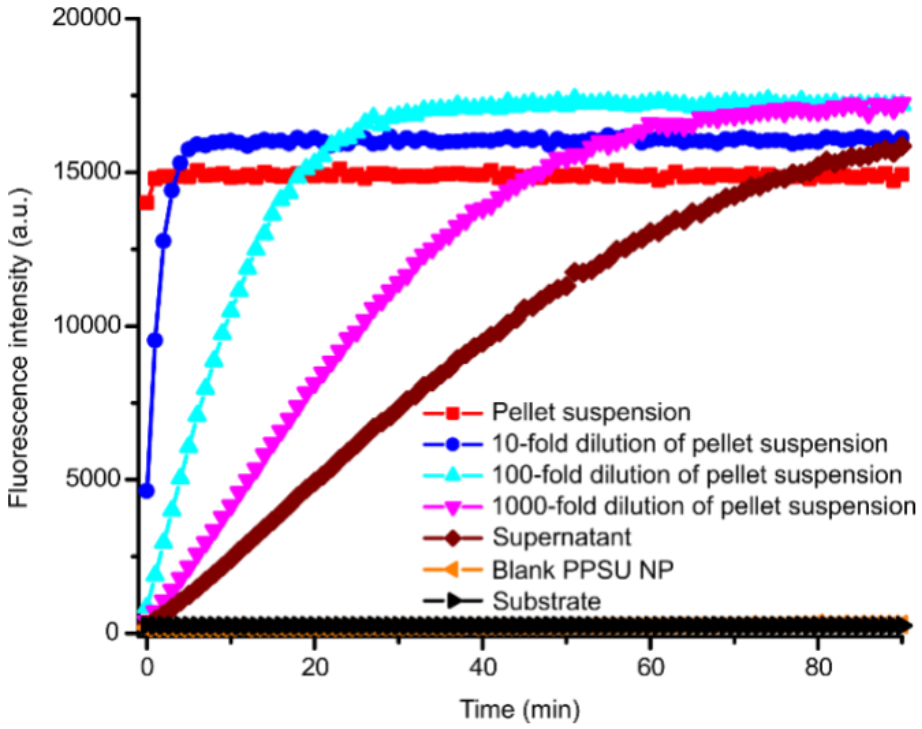

Figure B.14: 7-Amino-4-methylcoumarin (AMC) fluorometric assay demonstrating negligible trypsin desorption after the proteolysis of BSA. See supplemental methods (AMC fluorometric assay) for experimental details. Even the 1000-fold dilution of pellet (trypsin@NP) suspension showed a higher catalytic activity than that of the supernatant, suggesting that the ratio of desorbed/exchanged trypsin was less than 1/1000.

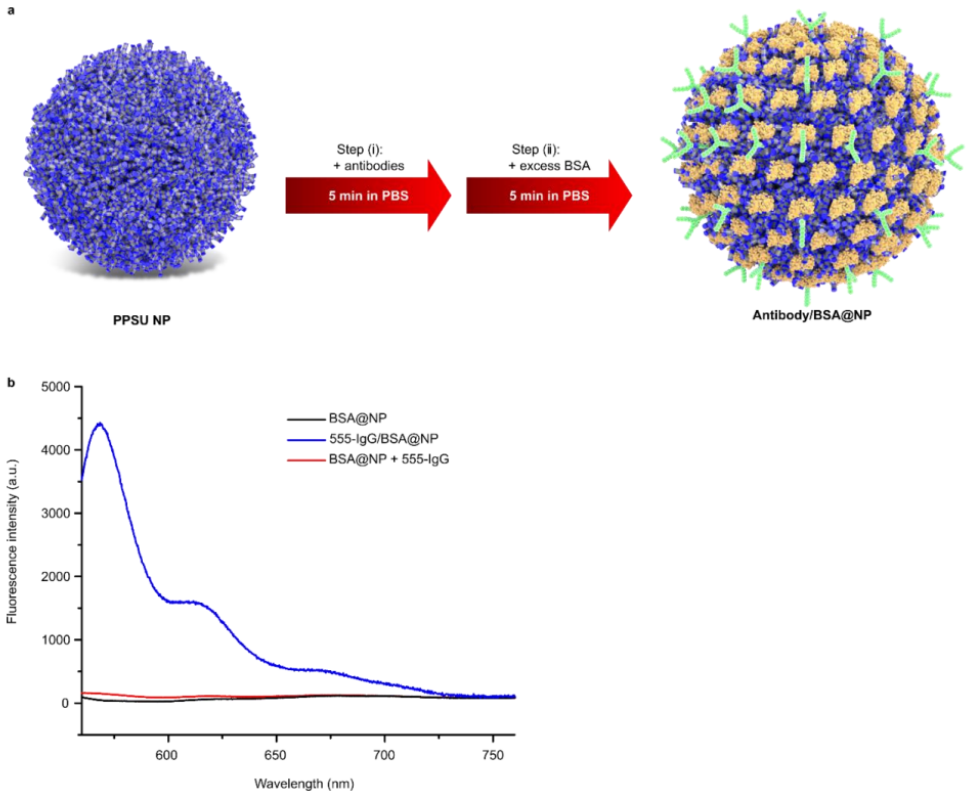

Figure B.15: Controlled formation of multi-component protein coatings at the surface of PPSU NP by two-step adsorption. (a) Schematic illustration of the rapid and facile process in targeting PPSU NPs using pre-adsorbed antibodies as targeting moieties. After the twostep mixing in PBS, unbound proteins were removed by thorough washing of the NPs with PBS. (b) Assessing the two-step adsorption protocol by incubating PPSU NPs with 555-IgG (Alexa Fluor 555-conjugated polyclonal donkey anti-rabbit antibody; BioLegend) and BSA in PBS. 555-IgG/BSA@NP was prepared by incubating PPSU NPs with 2 wt% of 555-IgG, followed by complete BSA (150 wt%) coating. Coating PPSU NPs with excess BSA (150 wt%) led to BSA@NP, which cannot adsorb 555-IgG (2 wt%), as confirmed by the fluorescence spectra (Ex =540 nm). Unbound proteins were removed by thorough washing with PBS before fluorescence measurements.

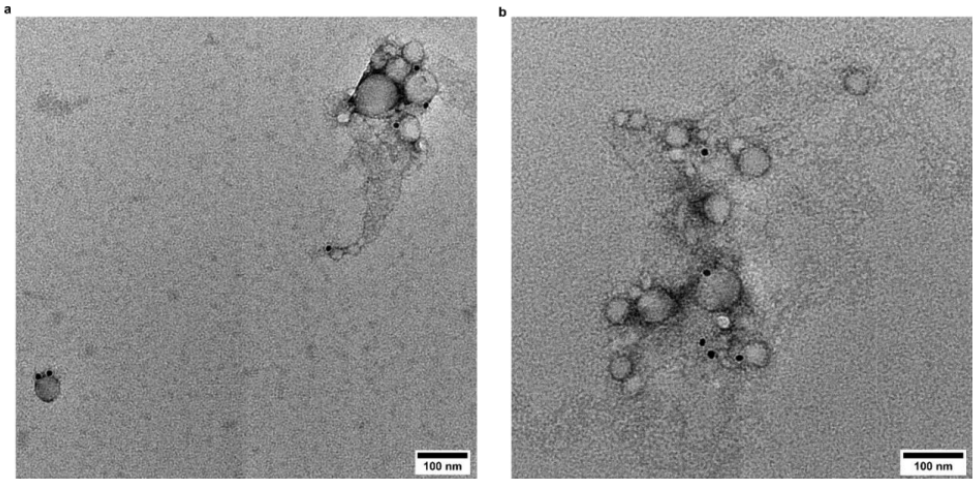

Figure B.16: Immunogold labelling. (a) Anti-CD4 antibodies and BSA co-adsorbed NPs stained with secondary gold-coupled antibodies. (b) BSA-adsorbed NPs stained with secondary gold-coupled antibodies. All the 10 nm colloidal gold was adsorbed at NP surfaces in (a), whereas unbound colloidal gold was observed in (b). Both the samples contained 1 wt.% of unbound BSA.

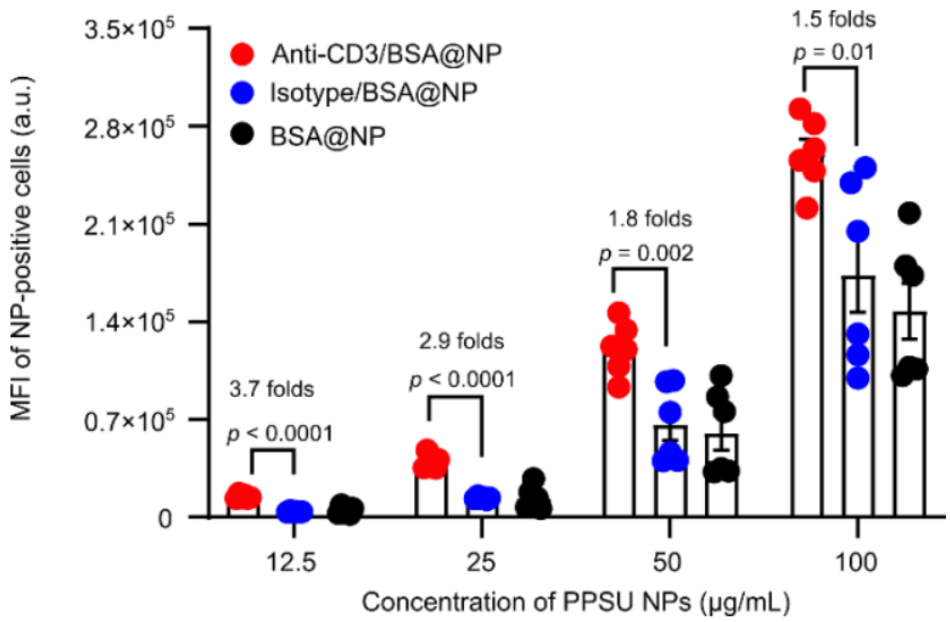

Figure B.17: Targeting PPSU NPs towards Jurkat T cells by the adsorption of anti-CD3 antibodies. Rhodamine B-encapsulated PPSU NPs were suspended in PBS with or without antibodies (anti-CD3 or Isotype control, 5 wt.% of PPSU) for 5 min, followed by coating with excess of BSA. Unbound proteins and any leaked rhodamine B were removed by washing with PBS. The rhodamine fluorescence was recorded by flow cytometry after 30 min of cell incubation with indicated concentrations of the NPs. Data were obtained from 6 parallel experiments (n = 6), and they are presented as mean values ± standard error. Significant P values are displayed on the graph. Statistical significance was determined by two-way ANOVA with Tukey's multiple comparisons test.

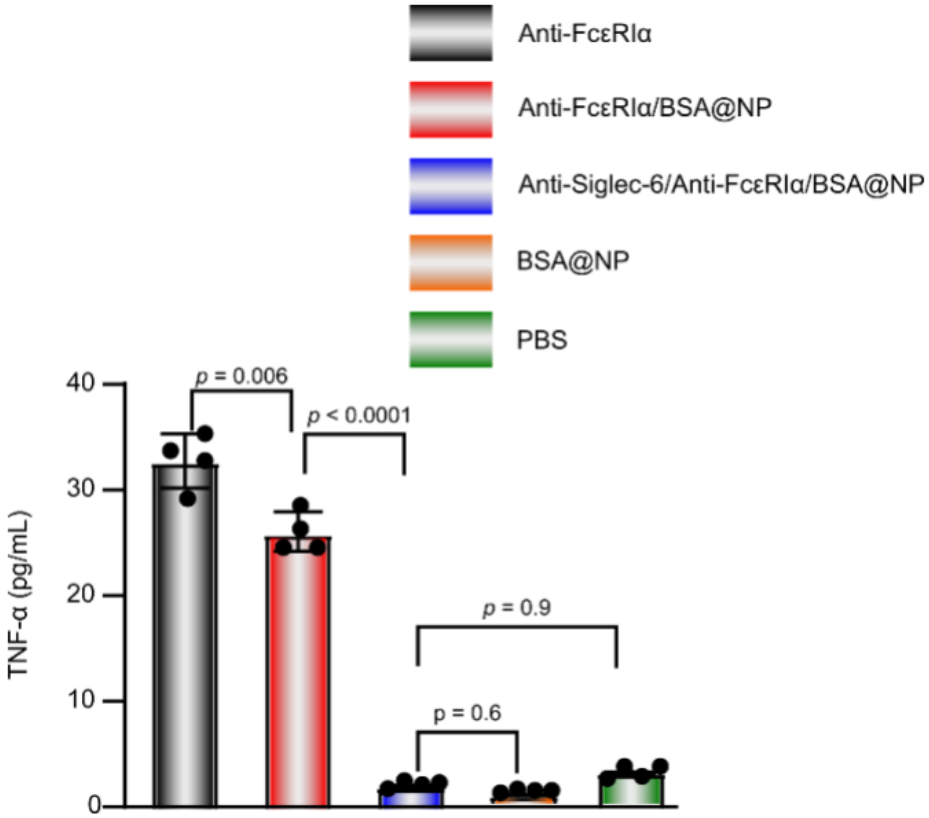

Figure B.18: TNF-α release measured after incubating human skin mast cells with test formulations for 3 h. Adsorbed anti-FcεRIα antibodies (red) were just as activating as unbound anti-FcεRIα antibodies (black). BSA@NP and PBS incubations were included as negative controls. Despite the presence of anti-FcεRIα antibodies, secretion was inhibited by co-localized engagement of both FcεRIα and Siglec-6 receptors (blue), allowing the dual antibody antiFcεRIα/anti-Siglec-6/BSA@NP to achieve similar levels of TNF-α expression as the BSA@NP and PBS controls. Results were from four parallel experiments (n = 4). Data are represented as mean values $\pm$ standard error. Statistical significance was determined via two-way ANOVA with Tukey-post hoc test.

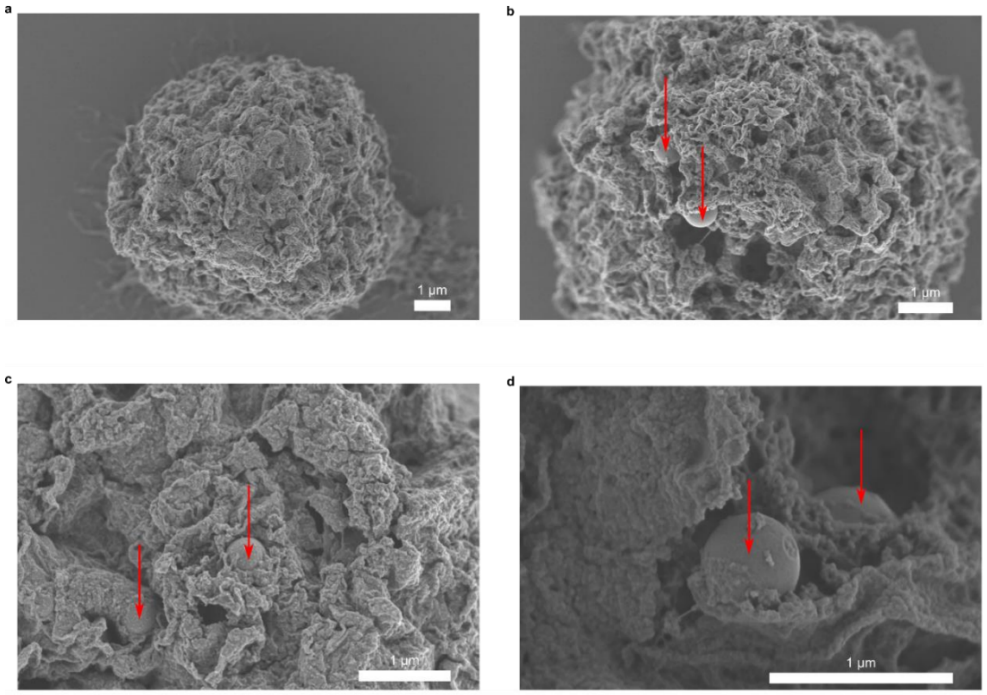

Figure B.19: Representative SEM images showing a mast cell treated with PBS (a) or the nanomedicine of anti-FcεRIα/anti-Siglec-6 co-adsorbed NPs (b-d). The NPs are indicated by the red arrows. Experimental samples were prepared for imaging three times.

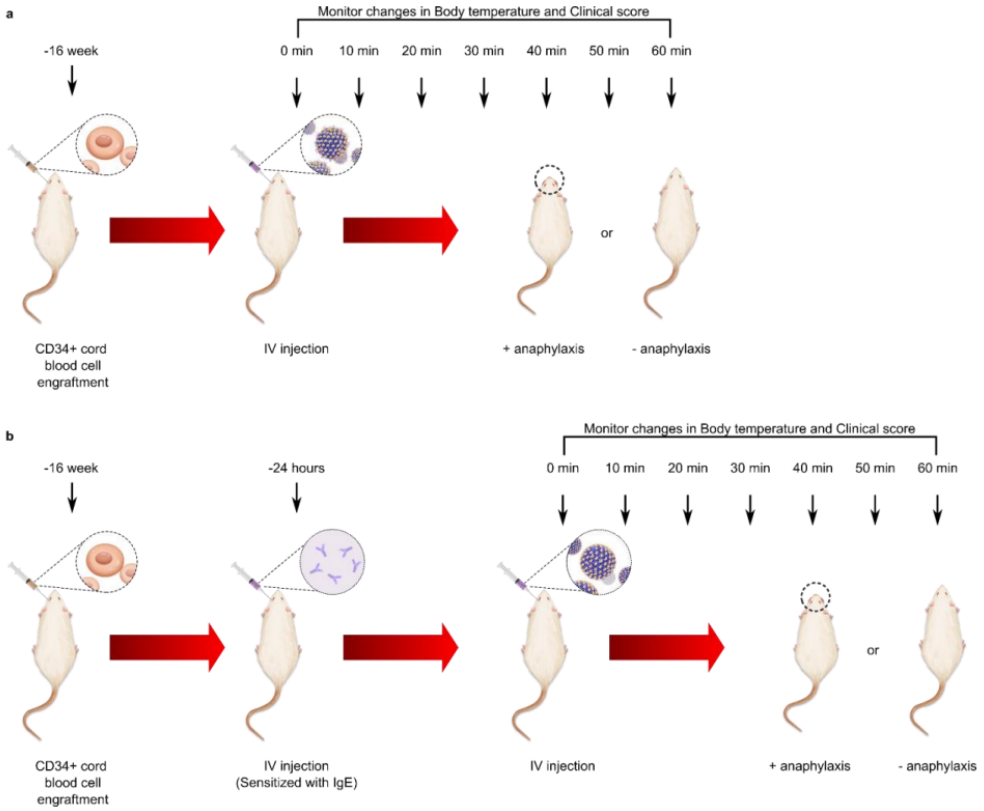

Figure B.20: Process of in vivo testing. (a) Design of humanized mast cell mouse engraftment and anaphylaxis protocol adapted from Dispenza et al[106]. (b) Design of humanized anaphylaxis model of IgE-mediated allergy[106,113,114,115]

B.2 Nonspecifically cross-linking hydrogel nanofibrils with proteins: from bioactive liquid droplets to thermally stabilized nanoenzymesy

B.2.1 Materials and Methods

Synthesis of PEG-PPSU

PEG-PPSU was synthesized from complete oxidation of the corresponding PEG-PPS. PEG-PPS was synthesized according to our previous studies (20-23). Shaking PEG-PPS in 30% hydrogen peroxide (1 g polymer per 100 mL of the hydrogen peroxide) led to a clear solution overnight. Lyophilization of the obtained solution resulted in white solids of PEG-PPSU without requirement for further purification.

Water and buffers

UltraPure^{TM} DNase/RNase-free distilled water (Invitrogen) was used in all the studies. TRP buffer was bought from Abcam (ab239210) and used for the digestions of AMC and FITC-BSA. Tris-HCl (pH 9.0) was used as the buffer for the enzymatic degradation of MP by OPH.

Hydrogel nanofibrils

Mixing 20 mg of PEG-PPSU with 1 mL of water led to the formation of hydrogel nanofibrils in water. The nanofibril suspension was dialyzed in PBS (to balance the pH), and then in water. The obtained PEG-PPSU hydrogel nanofibrils were stored at 4 °C at a concentration of 10 mg/mL in water.

Proteins

BSA (lyophilized powder) was bought from Fisher BioReagents (LOT# 156673) and used as received. HBB (lyophilized powder) was obtained from Sigma (H2500; LOT# SLCB6082) and used as received. LYZ (lyophilized powder) was bought from Sigma (L6876; LOT#SLBZ8428) and used as received. GFP (Aequorea Victoria GFP, His Tag, lyophilized powder) was obtained from

Invitrogen (LOT# LCL17JU0901) and used as received. Anti-Mouse IgG–Gold (10 nm) antibody was bought from Sigma (G7652) and used after the removal of glycerol by dialysis in water. TRP from porcine pancreas (lyophilized powder) was obtained from Sigma (T4799) and used as received. HRP (Type II, lyophilized powder) was bought from Sigma (P8250) and used as received. OPH was bought from Creative Enzymes (Cat# EXWM-3770) and used after the removal of glycerol and salts by using a desalting column (Zeba A57756).

Substrates

TMB was provided in the TMB Substrate Kit (Thermo Scientific^{TM} 34021). FITC-BSA (lyophilized powder) was bought from Sigma (A9771) and used as received. AMC was obtained from the Trypsin Activity Assay Kit (Abcam, ab282916). MP (analytical standard) was bought from Sigma (36187).

Study route

Unless otherwise stated, proteins and PEG-PPSU were first co-solubilized (protein/polymer = 1/50, w/w) in water, dehydrated, and subsequently resuspended in solvents or buffers. Typically, mixing 10 μL of proteins (1 mg/mL in water) with 50 μL of PEG-PPSU aqueous solution (10 mg/mL) or water, leading to the formation of liquid droplets or controls. The 60 μL of mixtures were divided, immediately followed by dehydration under high vacuum (3 μbar, 1 hour). The obtained solids were temporarily stored at -20 °C. For the stability studies, the solids or their suspensions were stored at 80 °C or 23 °C (room temperature) for a specified duration. After the removal of solvents (if applicable), fluorescence measurements (for GFP) and activity assessments (for TRP and OPH) were performed in the corresponding buffer (PBS for GFP, trypsin buffer for TRP, Tris-HCl for OPH) at 23 °C.

Cryo-TEM imaging

Lacey carbon grids (Electron Microscopy Sciences, LC400-CU-100) were treated for 20 s in a

Pelco easiGlow glow discharger (15 mA, 0.24 mbar). Each sample was prepared by applying 3 μL of aqueous suspension (4 mg/mL for PEG-PPSU and 3 mg/mL for PEG-PPS) on the pretreated grid. Following a blot of 3 s, the grid was then plunge-frozen (Gatan Cryoplunge 3 freezer). Images of samples entrapped in vitreous ice were acquired using a 200kV CryoTEM (Glacios^{TM}) quipped with an AMETEK Gatan K3 direct electron detector. In the in-situ ice sublimation experiments, images were continuously taken with an average camera exposure intensity of $51.0 \pm 0.6 e/\text{Å}$. Any further image processing, including adjusting color balance, conducted on the aligned frames was completed in ImageJ 1.53e software.

X-ray scattering

X-ray scattering was performed at the DuPont, Northwestern, Dow Collaborative Access Team beamline at Argonne National Laboratory's Advanced Photon Source with 10 keV (wavelength $\lambda = 1.24$ Å) collimated X-rays. The aqueous suspension of PEG-PPSU nanofibrils (9 mg/ml) was analyzed in the q range (0.001–0.500 Å^{-1}), with a sample-to-detector distance of 8.5 m and an exposure time of 5 s. The beamline was calibrated using silver behenate and gold-coated silicon grating with 7,200 lines per mm. The momentum transfer vector q is defined as $q = 4\pi \sin\theta/\lambda$, where 2θ is the scattering angle. Data reduction and buffer subtraction were performed using the IRENA 2.71 package within IGOR PRO 9 software (WaveMetrics). Model fitting was completed using SasView 5.0.5 software package where the flexible cylinder model was utilized to fit and analyze the data.

Transmittance measurement

The transmittance of PEG-PPSU (1.0 mg/mL in water) was tracked upon the addition of BSA by Perkin Elmer LAMBDA 1050.

Fluorescence measurement

Fluorescence spectra were recorded by an RF-6000 spectrofluorometer using LabSolutions RF

software. Time-dependent fluorescence intensities were tracked by the RF-6000 or using a SpectraMax M3 microplate reader (Molecular Devices).

TEM imaging of liquid droplets

90 μL of Anti-Mouse IgG–Gold ($\sim$0.1 mg/mL in water) were mixed with 10 μL of nanofibrils (10 mg/mL in water), leading to the formation of liquid droplets for TEM imaging. 1.5% uranyl formate (UF) was prepared in water. The pH was adjusted to 4.5 by addition of 10 M KOH. Forrmvar carbon film grids (Electron Microscopy Sciences, FCF400-CU) were treated for 20 s in a Pelco easiGlow glow discharger (15 mA, 0.24 mbar). A pretreated grid was suspended upside down in 20 μL of solution of liquid droplets for 30 s, followed by the removal of excess solution by blotting with Whatman filter paper. For TEM with staining, the sample-loaded grid was further suspended upside down in 30 μL of 1.5% UF for 15 s. This staining procedure was repeated once more, followed by the removal of excess UF solution by blotting with Whatman filter paper. The grids were then dried under vacuum for 24 hours. TEM Images were acquired at 30 k on a JOEL 1400 TEM operating at 120 kV.

TEM imaging of GFP/PEG-PPSU nanoparticles formed in toluene

The grids (Electron Microscopy Sciences, CFGA75-CU, Carbon Support Film Single Hole) were treated for 20 s in a Pelco easiGlow glow discharger (15 mA, 0.24 mbar). A pretreated grid was suspended upside down in 20 μL of toluene consisting of 1 mg/mL of GFP/PEG-PPSU for 30 s, followed by the removal of excess solution by blotting with Whatman filter paper. The grids were then dried under vacuum for 24 hours. TEM Images were acquired at 30 k on a JOEL 1400 TEM operating at 120 kV.

SEM imaging

To image the intact PEG-PPSU loaded with GFP, we employed high-pressure freezing to avoid chemical fixation, dehydration, or drying of the samples. For the preparation of samples, 100 μg

of PEG-PPSU was mixed with or without 2 μg of GFP in 12 μL of water. High-pressure freezing was conducted using the BioCryo Leica EM HPM100, following the manufacturer's recommendations. Subsequently, the samples were transferred into a nitrogen chamber and then processed using the BioCryo Leica EM VCT100 and ACE600 for freeze-drying. After overnight drying, the samples were mounted on carbon tape attached to an aluminum stud and coated with a 10 nm thickness of SPF Osmium using an Osmium Coater. The morphology was observed using a Hitachi SU-8030 in SEM analysis.

TMB substrate assay

The Thermo Scientific TMB Substrate Kit (34021) was used. 10 μL of HRP solution (1 mg/mL in water) were mixed with 50 μL of PEG-PPSU suspension (10 mg/mL in water) or water. After dividing each mixture (60 μL) into four equal parts, water was removed under a high vacuum. 200 μL of the provided TMB substrate solution were added into each sample, followed by incubation at room temperature until the desired color develops.

AMC Assay

The TRP activity assay Kit (Abcam, ab239210) was used. The fluorescence intensity (Ex/Em = 380/460 nm) in kinetic mode was tracked for 90 min at room temperature using the fluorescence microtiter plate reader (100 μL of TRP buffer/well) or the RF-6000 spectrofluorometer (1 mL of TRP buffer/ cuvette). The provided substrate was 5000-fold diluted in each reaction, with 0.2 μg/mL of TRP and varying concentrations of PEG-PPSU.

Digestions of FITC-BSA

The fluorescence intensity (Ex/Em = 485/525 nm) in kinetic mode was tracked for 90 min at room temperature using the fluorescence microtiter plate reader. In each well, there were 100 μL of TRP buffer, 5 μg of FITC-BSA, 2 μg of TRP, and varying amounts of PEG-PPSU.

Degradations of MP

Before the experiments, 5 μL of MP solution (100 mg/mL) were placed and dried in each glass insert (300 μL fill volume). In each test, 0.2 μg of OPH with or without 10 μg of PEG-PPSU were dissolved in 10 μL of Tris-HCl. The solution was then added into the MP-containing glass insert. The absorbance was measured after 5 min by a NanoDrop absorbance spectrophotometer (Thermo Fisher ND 2000).

Solubilization of DiO by PEG-PPSU nanofibrils

DiO powders (Invitrogen; LOT 2527973) were shaken with water, PEG45/water (1 mg/mL; PEG45 from Sigma 202509), or PEG45-PPSU20 nanofibrils/water (1 mg/mL) for 24 hours at room temperature. After centrifugation, the suspensions were transferred into three glass vials for taking photos under UV light (365 nm). Fluorescence spectra were recorded by RF-6000 without diluting the suspensions.

Exploring phase separation through all-atom MD Simulations

Gromacs 2021.5 and CHARMM 36m forcefield were combined to perform the all-atom MD simulations. Visualization of the simulation trajectories is achieved by VMD. A Python package MDAnalysis was used for post-analysis. The phase separation of PEG-PPSU was studied with all-atom MD simulations. In a $20 \times 20 \times 20\ \mathrm{nm}^3$ box, 50 PEG-PPSU (same as the experiments) chains were dissolved in CHARMM TIP3P water. The system was energy minimized for 10000 steps with a force tolerance of 1000 $\mathrm{kJmol}^{-1}\mathrm{nm}^{-1}$. Subsequently, the system was equilibrated under the NVT ensemble (constant number of particles, constant volume, and constant temperature) and the NPT ensemble (constant number of particles, constant pressure, and constant temperature). The NVT equilibration used the V-rescale thermostat to fix the temperature and ran for 1 ns with a timestep of 1 fs. The NPT equilibration used the V-rescale thermostat to fix the temperature and the Berendsen barostat to fix the pressure. The NPT equilibration ran for 750 ps with a timestep of 1.5 fs. After equilibration, 2 consecutive production runs were performed at 353 K and 298

K, respectively. The production run at 353 K was utilized to eliminate the effect of initial configurations. For the production run, the Nose-hoover thermostat was used to keep the temperature constant with a coupling time of 0.5 ps. The solvent and PEG-PPSU were coupled separately. The Parrinello-Rahman barostat was used to fix pressure, with a reference pressure of 1 bar, a pressure coupling time of 5 ps, and a compressibility of $4.5 \times 10^{-5}\mathrm{bar}^{-1}$. Fast smooth Particle-Mesh Ewald (SPME) was utilized to calculate the Coulombic interaction with a cutoff for the short-range interaction at 1.2 nm. The cut-off method with a cutoff of 1.2 nm and the potential-switch modifier were adopted to calculate the Van der Waals interaction. The Verlet scheme was used for neighbor searching with a cutoff of 1.2 nm. The neighbor list was updated every 20 steps. Periodic boundary condition in all directions was used for the simulation. The water structure was constrained with the SETTLE algorithm. The timestep is 2 fs and the simulation ran for 80 ns for the run at 353 K and for 200 ns for the run at 298 K. In total 4 parallel runs were performed to obtain average data. The other 4 parallel simulations were performed on $\mathrm{PEG}_{44} - \mathrm{PPS}_{20}$ with the same parameters mentioned above. The radial distribution functions of each component in both polymers were analyzed.

All-atom MD Simulating the adsorption of PEG-PPSU at protein surfaces

Gromacs 2021.5 and CHARMM 36m forcefield were combined to perform the all-atom MD simulations. Visualization of the simulation trajectories is achieved by VMD. A Python package MDAnalysis was used for post-analysis. All-atom simulations were performed on systems of PEG-PPSU in complex with GFP, OPH, and TRP, respectively. Due to the different sizes and shapes of the proteins, the number of PEG-PPSU chains in the box varies for each system to ensure complete coverage of the polymer on proteins. The protein PDB IDs, number of PEG-PPSU chains, and simulation box sizes are listed in Table S1. The protein with its crystal water was dissolved in toluene. No extra ions but counter ions were added. The system was energy minimized for 10000

steps with a force tolerance of 100 $\mathrm{kJmol^{-1}nm^{-1}}$. The NVT equilibration ran for 500 ps with a timestep of 1 fs and the NPT equilibration ran for 1 ns with a timestep of 1 fs. A production run at 400 K was performed for 40 ns with a timestep of 2 fs and with a position restraint placed on the protein and its crystal water to remove effects from the initial configuration and accelerate the diffusion of polymers. Subsequently, a production run at 298 K was performed for 200 ns with a timestep of 2 fs. Other simulation settings were the same as those in the previous section. Parallel simulations were performed of the same PEG-PPSU/protein complexes in water. The protein surface coverage in each system was calculated with the gmx sasa command embedded in Gromacs. The $-\mathrm{SO_2}-$ groups on PPSU that are within 2.5 Åof the water solvent molecules or protein molecules are considered as surface groups. The compositions of the TRP binding domains were analyzed with our recently developed program Protein Surface Printer (19).

Well-tempered Metadynamics MD simulations

To explore the dissolution of PEG-PPSU in ultra-diluted aqueous solution, we carried out Well-tempered Metadynamics simulations using GROMACS 2023.0 with the patched Plumed 2.9.0. One PEG-PPSU polymer chain was dissolved in a water box of around 10 nm in all dimensions. The CHARMM 36m potential was employed, as in our previous works. The recommended CHARMM TIP3P water model was utilized with the water structures constrained via the SETTLE algorithm.

The energy of the system was first equilibrated using the steepest descent algorithm. It was further equilibrated for a duration of 0.1 ns using the isothermal-isobaric ensemble (constant number of particles, pressure, and temperature, NPT). The periodic boundary conditions were employed in all three dimensions. The neighbor searching was done up to 12 Åusing the Verlet particle-based method and updated every 20-time steps. The Lennard-Jones 12-6 interactions were switched off from 10 to 12 Åwith the potential-switch method. The short-range electrostatic interactions were

truncated at a distance of 12 Åwith the Smooth Particle Mesh Ewald (PME) algorithm applied for the long-range interactions. In the production simulation, the temperature was coupled using the Nosé-Hover algorithm (reference temperature 298 K, characteristic time 0.5 ps). The isotropic Parrinello-Rahman barostat was used with the reference pressure of 1 bar, the characteristic time was 4 ps, and the compressibility of $4.5 \times 10^{-5}\mathrm{bar}^{-1}$. An integration time step of 2 fs was employed with the hydrogen-involved covalent bonds constrained.

In the well-tempered metadynamics simulations, the number of PPSU sulfur-sulfur contacts was employed as the collective variable to examine the folding behavior of PEG-PPSU. The PPSU sulfur atoms were counted as contacts when they were less than 6.6 Å, the upper distance of the first shell of the sulfur-sulfur radial distribution function. The Gaussian bias potential was deposited every 1 ps with an initial height of 2 kJ/mol and a bias factor of 20. The Gaussian width (sigma) is 2. We also examined different sets of parameters for the well-tempered metadynamics, which provided a consistent state for the most stable structure. The temperature of the system was 298.15 K. The well-tempered metadynamics run for a duration of 2 μs. The calculated free energy surface (FES) is provided in Fig. S3, along with the characteristic structures with the global minimum energy.

Coarse-grained MD Simulating the adsorption of PEG-PPSU nanofibrils at protein surfaces

LAMMPS Nov 23 was used for the coarse-grained MD simulations. In the simulation, only Lennard-Jones (LJ) potentials were considered. Weeks-Chandler-Andersen (WCA) potential was used for all pairwise potentials except PPSU-protein potentials. The WCA potential is the shifted regular Lennard-Jones potential that only includes hard potentials.

$$U_{WCA}\left(r_{ij}\right) = \begin{cases} 4\varepsilon\left[\left(\dfrac{\sigma_{ij}}{r_{ij}}\right)^{12} - \left(\dfrac{\sigma_{ij}}{r_{ij}}\right)^{6}\right] + \varepsilon & r_{ij} < 2^{1/6}\sigma_{ij} \\ 0 & r_{ij} > 2^{1/6}\sigma_{ij} \end{cases} \tag{B.1}$$

Where r is the distance between particle i and j; ε is the LJ energy; and σ is the 0 potential distance between i and j. Regular Lennard-Jones potential is used for PPSU-protein interactions to model the binding. The potential ratio of PPSU-hydrophobic patches and PPSU-hydrophilic patches was mapped from the average energy of AAMD simulations.

The nanofibril was modeled as a rod with a rigid body center axis and free PEG and PPSU sidechains. Beads in each sidechain were connected with FENE bonds. The rod has a diameter of 4.5 nm and a length of 15 nm. The protein was modeled as 32 beads distributed evenly on a spherical surface with random hydrophobic and hydrophilic patches. The protein has a diameter of 3 nm. The ratio of hydrophobic to hydrophilic in the protein surface was 3/7 to mimic a random water-soluble protein. In a $52.5 \times 52.5 \times 82.5\mathrm{nm}^3$ box, 125 nanofibrils and 8 proteins were mixed. Overlapped molecules were removed. The system was first energy minimized, followed by a production run. The production run was performed under the NVE ensemble (constant number of particles, constant volume, and constant energy) with Langevin dynamics. The unit time τ was set as 5×10^{-12} s. The simulation is run for $10^6\tau$. The radial distribution functions of PPSU and PEG around proteins were calculated. The number of binding nanofibrils and binding PPSU units were counted.

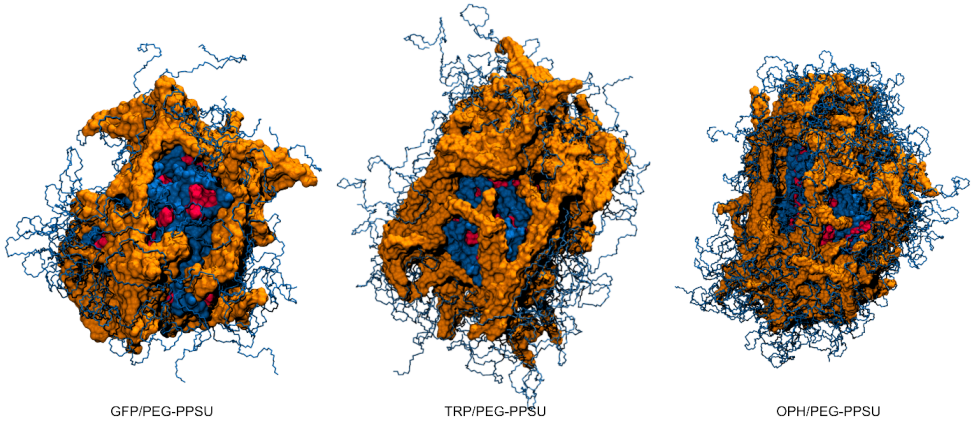

Figure B.21: The explicit solvent all-atom MD simulations performed on the mixture of PEG-PPSU (PEG, blue; PPSU, orange) with proteins (hydrophobic patches, red; hydrophilic patches, blue) in water led to the formation of a polymeric framework around each protein.

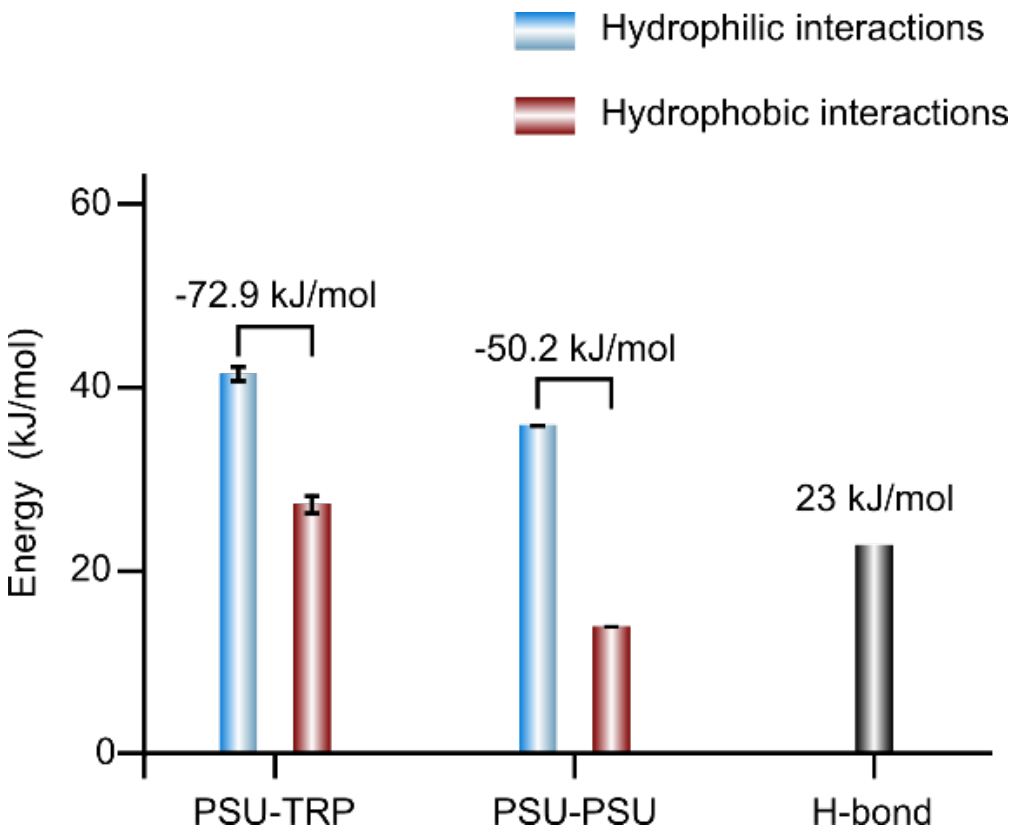

Figure B.22: Energy between propylene sulfone (the repeating unit, PSU) and TRP in water. The energy among PSU units was also calculated. The energy of a typical H-bond is included for comparison. The data are presented as mean values (n = 649).

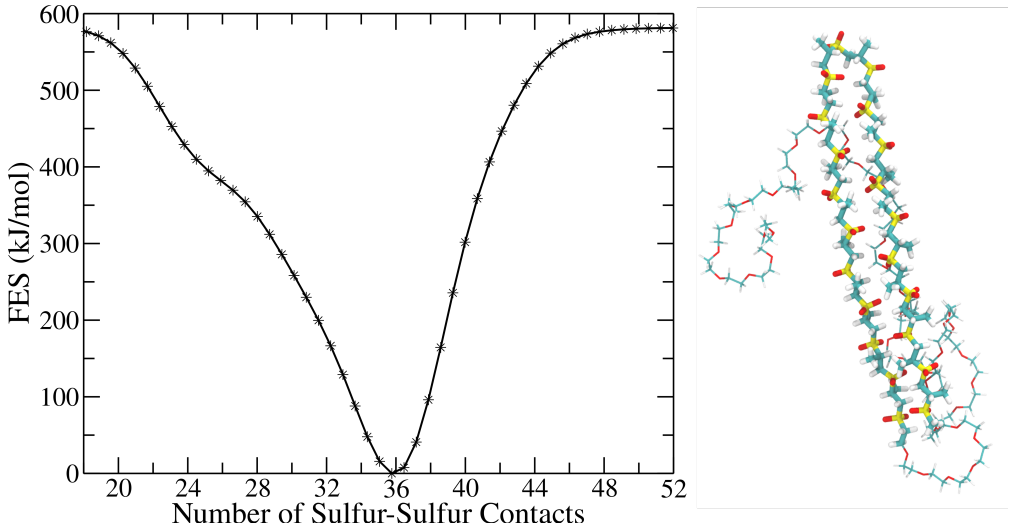

Figure B.23: Free energy surface (FES) as a function of the number of PPSU sulfur-sulfur contacts obtained from well-tempered metadynamics simulations. Structures with 36 sulfur-sulfur contacts are energetically most favored with one characteristic structure provided on the right. PPSU/PEG are in thick/thin lines, respectively. Sulfur atoms are colored in yellow, with oxygen/carbon/hydrogen atoms in red/cyan/white, respectively.

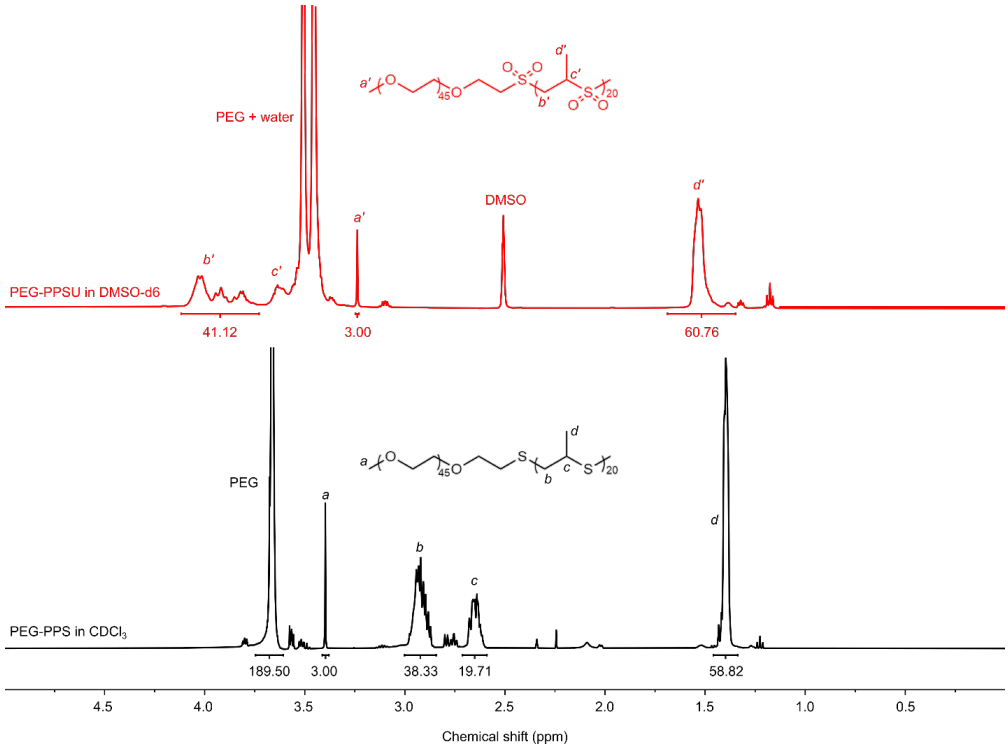

Figure B.24: $^{1}\mathrm{H}$ NMR spectra (500 MHz) for PEG-PPSU (red) in DMSO-d_6 and PEG-PPS (black) in CDCl_3. The chemical structures and integrated area of each characteristic peak are shown.

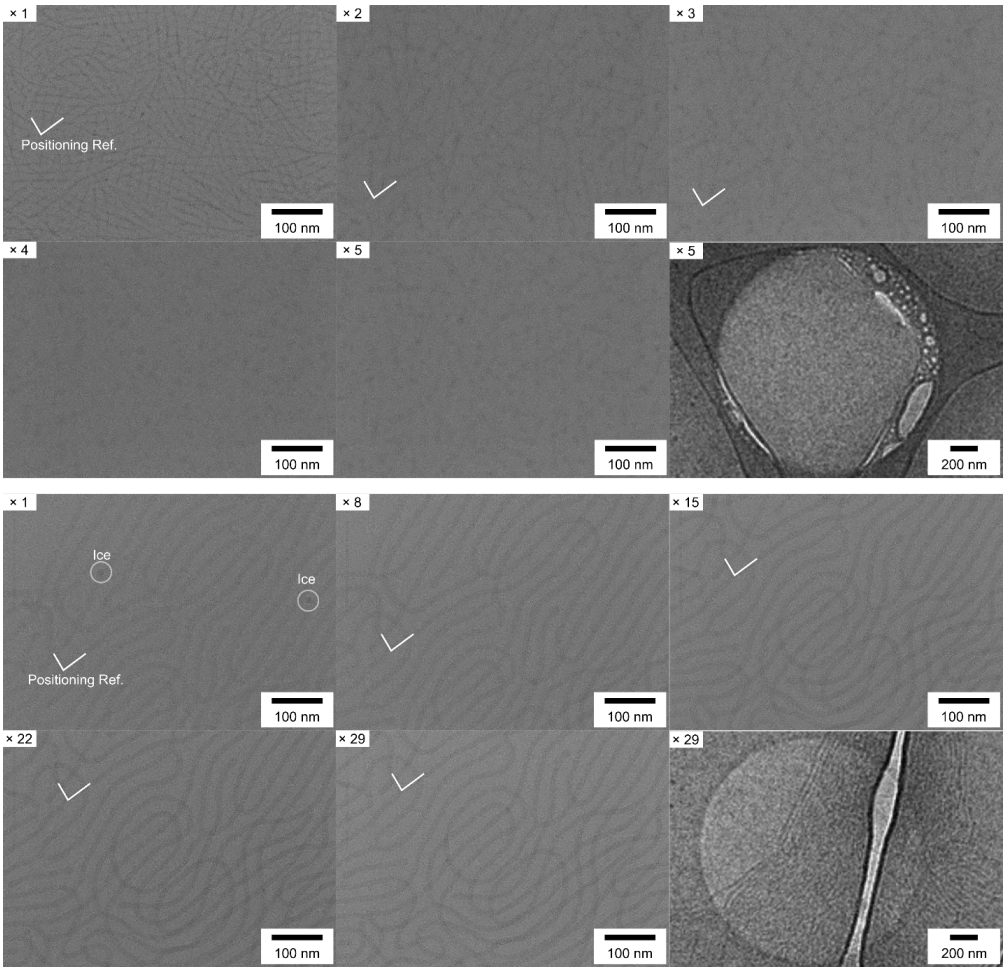

Figure B.25: Cryo-TEM images obtained through multiple consecutive imaging for PEG_{45}-$PPSU_{20}$ hydrogel nanofibrils (top) and PEG_{45}-PPS_{20} filomicelles (down, control). The beam-induced drift and imaging times are shown in the images. The last image for each structure shows the formation of a thin ice layer within the circular area irradiated by the electron beam. Upon the sublimation of ice, the PEG-PPSU hydrogel nanofibrils disappear or degrade, whereas the PEG-PPS filomicelles become clearer.

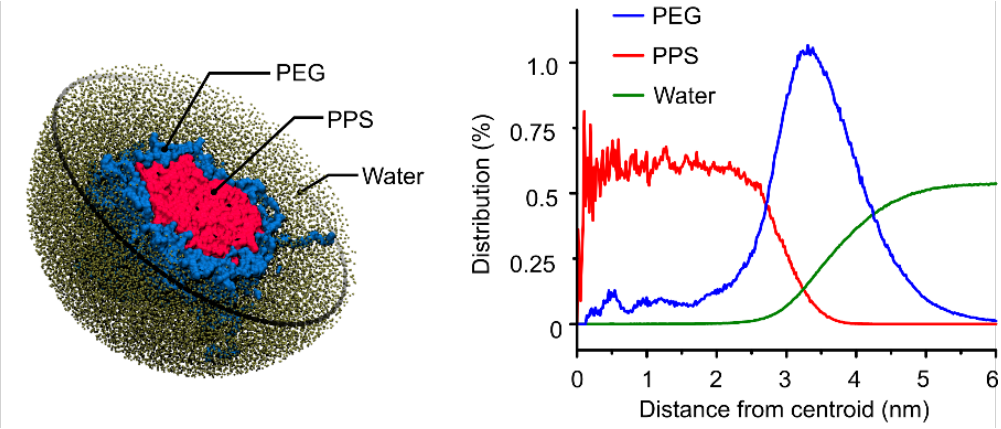

Figure B.26: Atomistic simulation on PEG-PPS assembly in water yields a phase separated core-shell structure. The hydrophobic PPS chains are completely shielded by the PEG corona. No water exists in the hydrophobic PPS core.

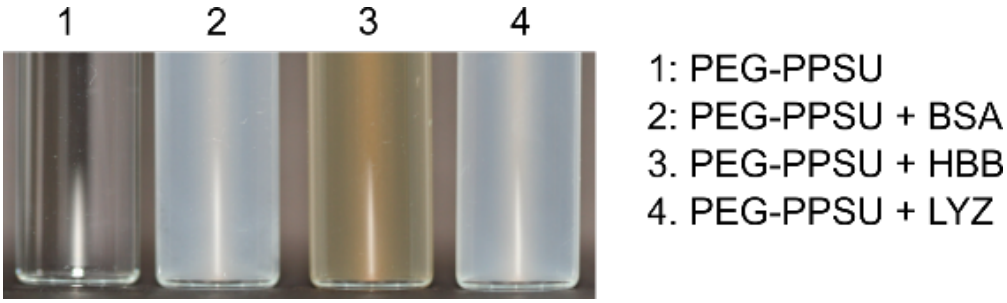

Figure B.27: The addition of proteins (BSA, HBB, or LYZ) causes a clear solution of PEG-PPSU (5 mg/mL in water) to become cloudy.

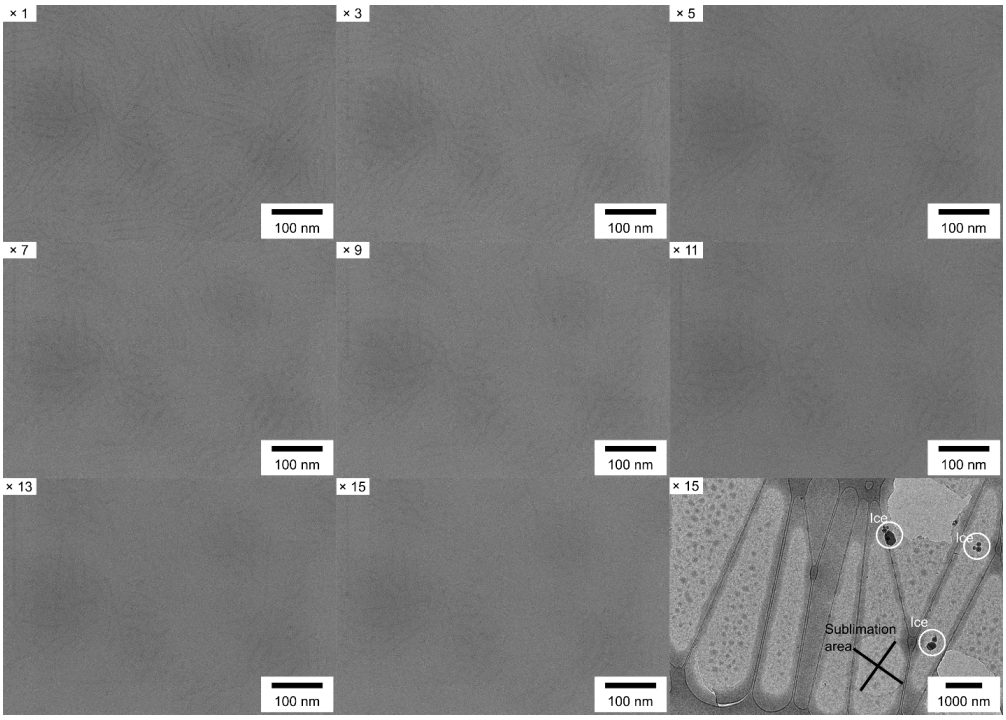

Figure B.28: Using an approach of in situ ice sublimation to confirm the formation of liquid nanodroplets by cryo-TEM. The liquid nanodroplets were formed by mixing PEG-PPSU hydrogel nanofibrils with 1 wt.% of BSA in PBS. The imaging times are shown in the images. Unbound nanofibrils disappear before the cross-linked nanofibrils as the imaging times increase. The last image shows the formation of liquid nanodroplets (disappeared under the beam) at low magnification.

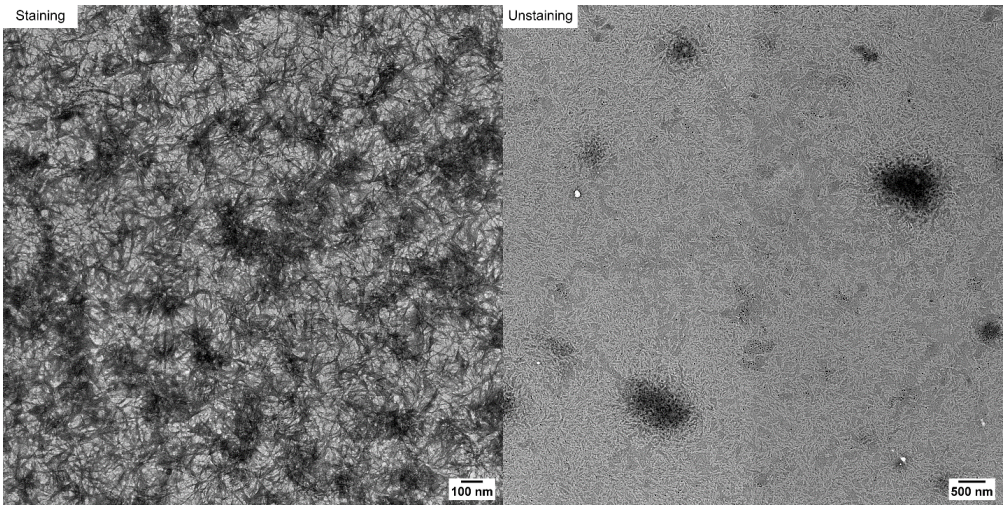

Figure B.29: Using 10 nm colloidal gold-IgG (indicated by the red arrows) to locate the liquid droplets. TEM images were obtained for the aqueous suspension with and without staining the hydrogel nanofibrils by UF.

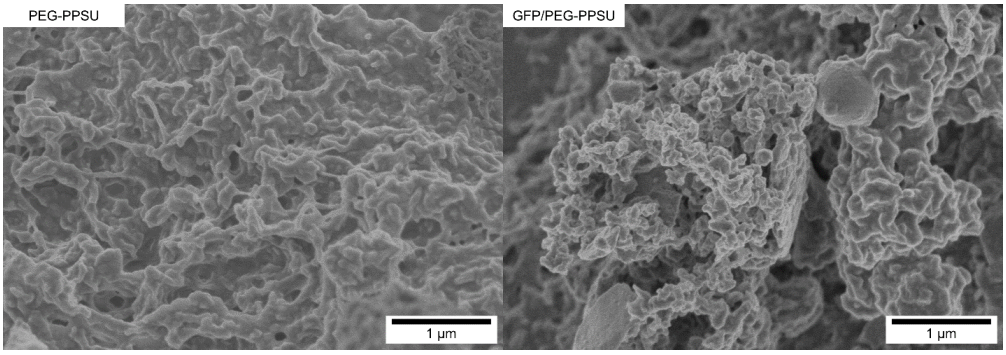

Figure B.30: Removal of water from PEG-PPSU aqueous solutions (with/without GFP) leads to porous structures seen by SEM.

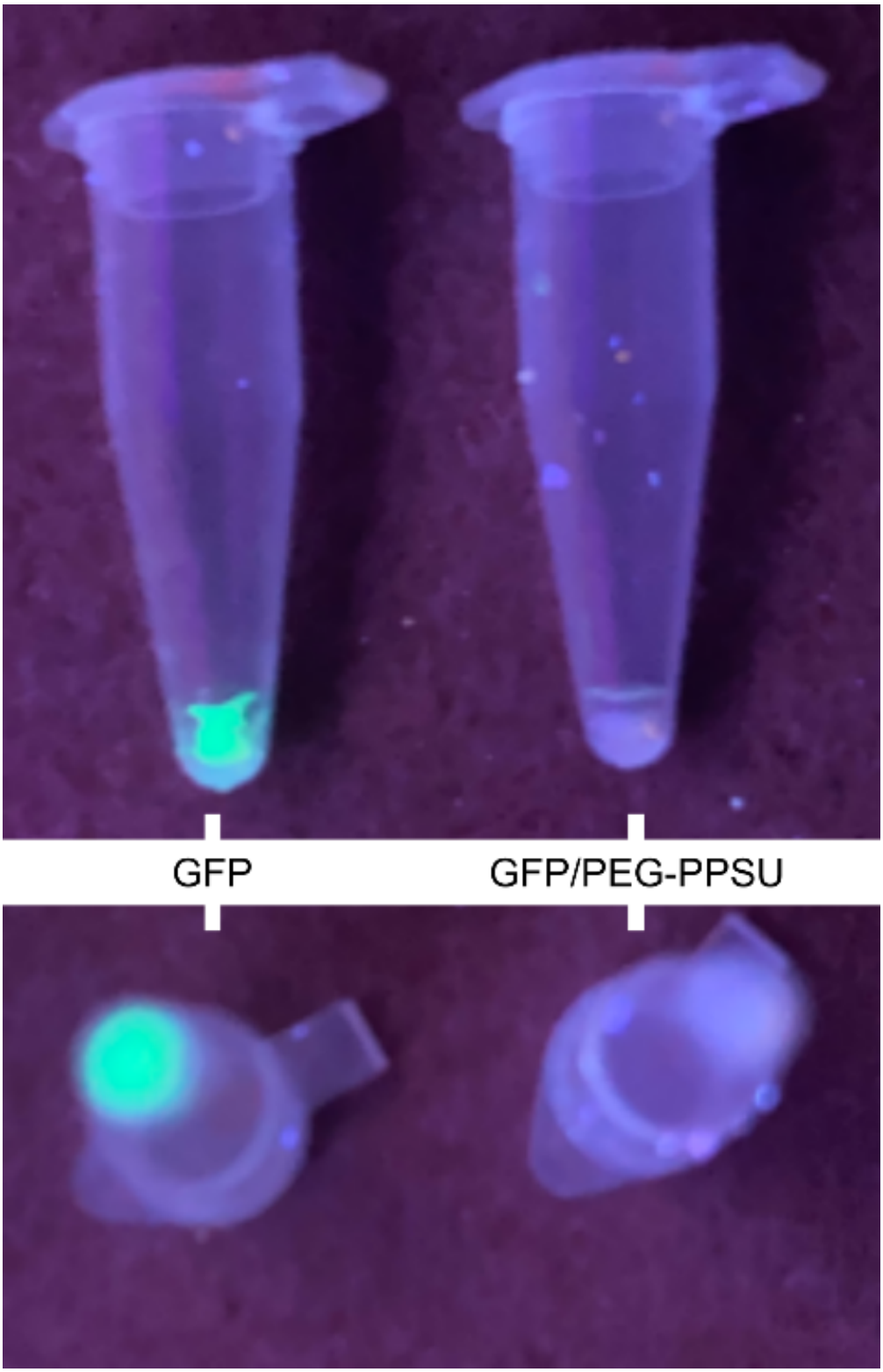

Figure B.31: Digital photos of dehydrated GFP and GFP/PEG-PPSU under 365 nm UV light.

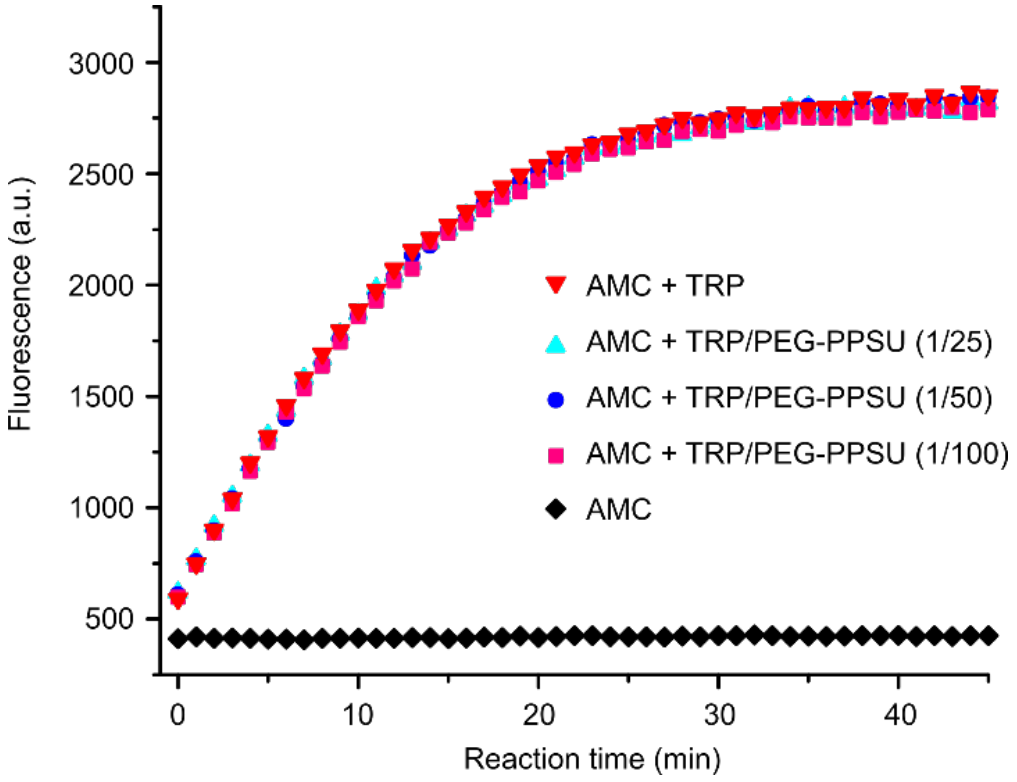

Figure B.32: Using AMC as the small-molecule substrate to quantify the preserved activity of reswelled TRP in the presence of different amounts of PEG-PPSU.

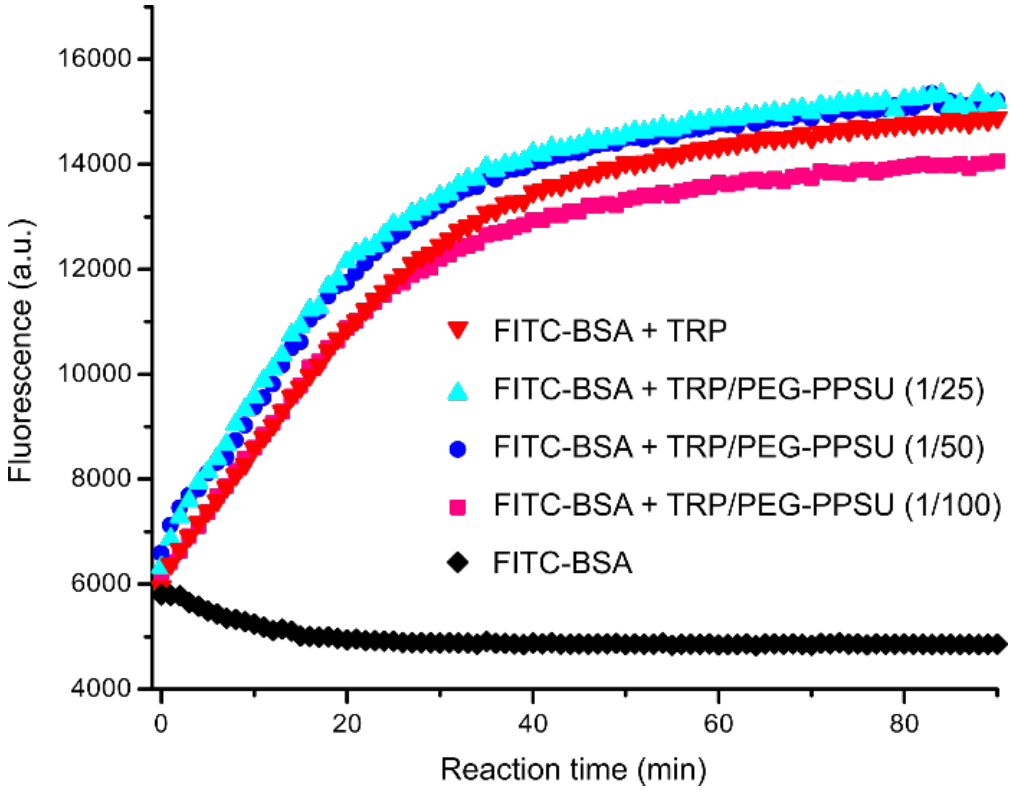

Figure B.33: Using FITC-BSA as the protein substrate to quantify the preserved activity of reswelled TRP in the presence of different amounts of PEG-PPSU.

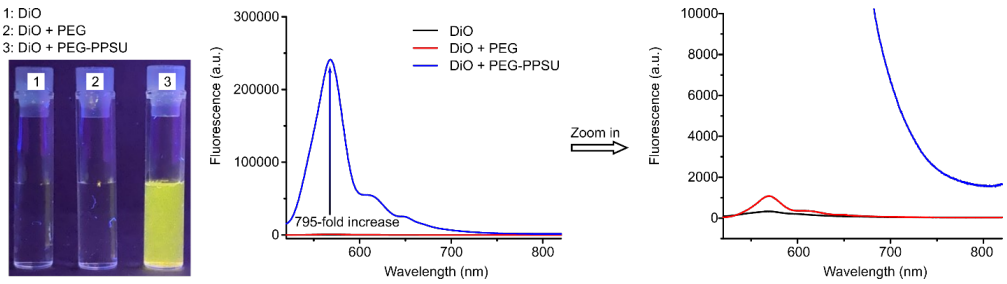

Figure B.34: Using PEG-PPSU nanofibrils as surfactant to promote the solubility of DiO (Invitrogen; LOT 2527973) in water.

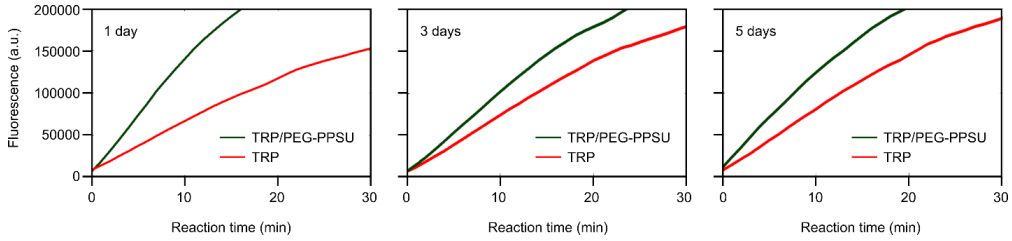

Figure B.35: Improved thermal stability for solid TRP is achieved in the presence of PEG-PPSU. Activities were measured by the AMC assay after storing the TRP or TRP/PEG-PPSU solids at 80 °C for different days.

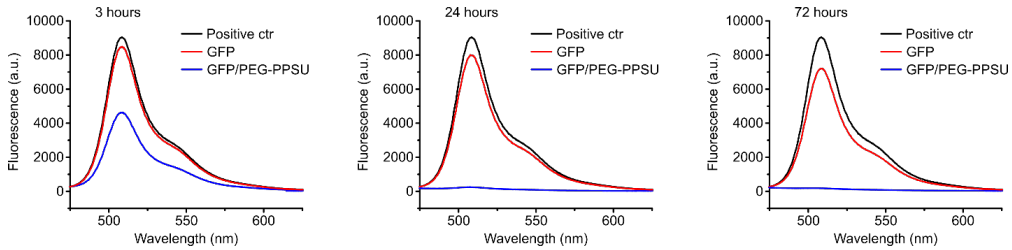

Figure B.36: The presence of PEG-PPSU decreases the thermal stability of GFP at solid state. Samples were stored at 80 °C for different hours before measuring the fluorescence in PBS. The positive ctr was GFP lyophilized powders without any treatment.

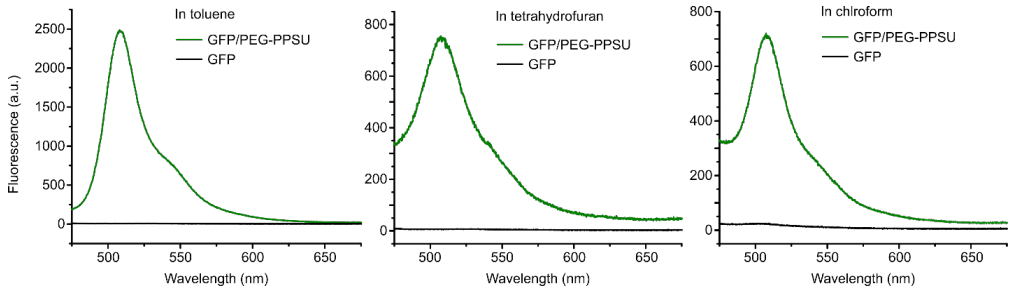

Figure B.37: Fluorescence spectra (E_x = 390 nm) of GFP or GFP/PEG-PPSU in different organic solvents.

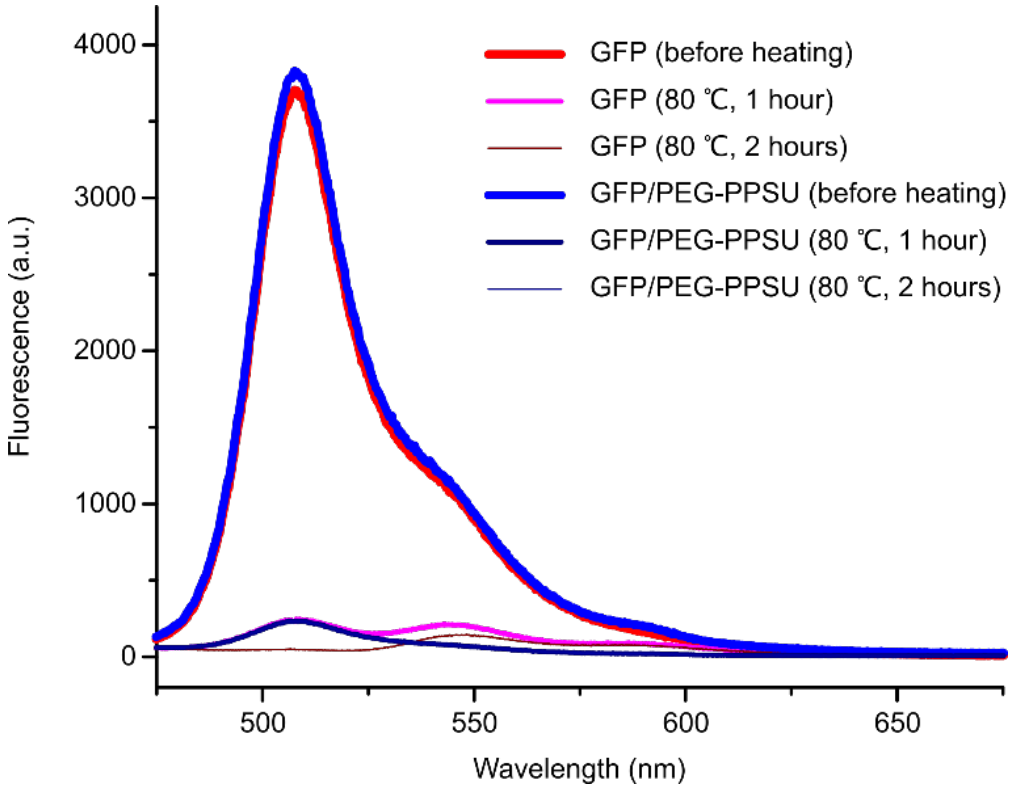

Figure B.38: Storing GFP in aqueous solution at 80 °C led to fluorescence quenching, regardless of the addition of PEG-PPSU.

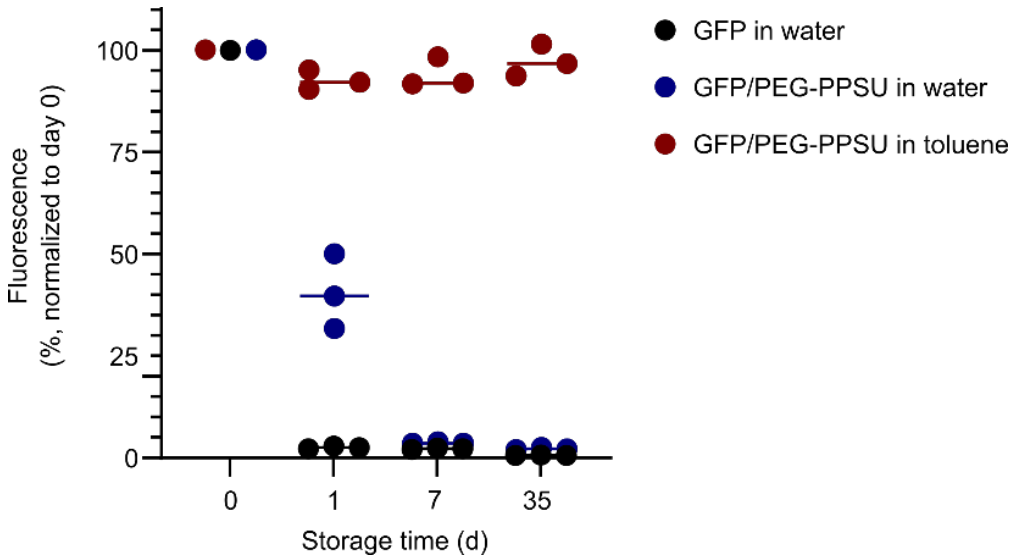

Figure B.39: The presence of PEG-PPSU enables room temperature storage of GFP in toluene without significantly decreasing the fluorescence over 35 days.

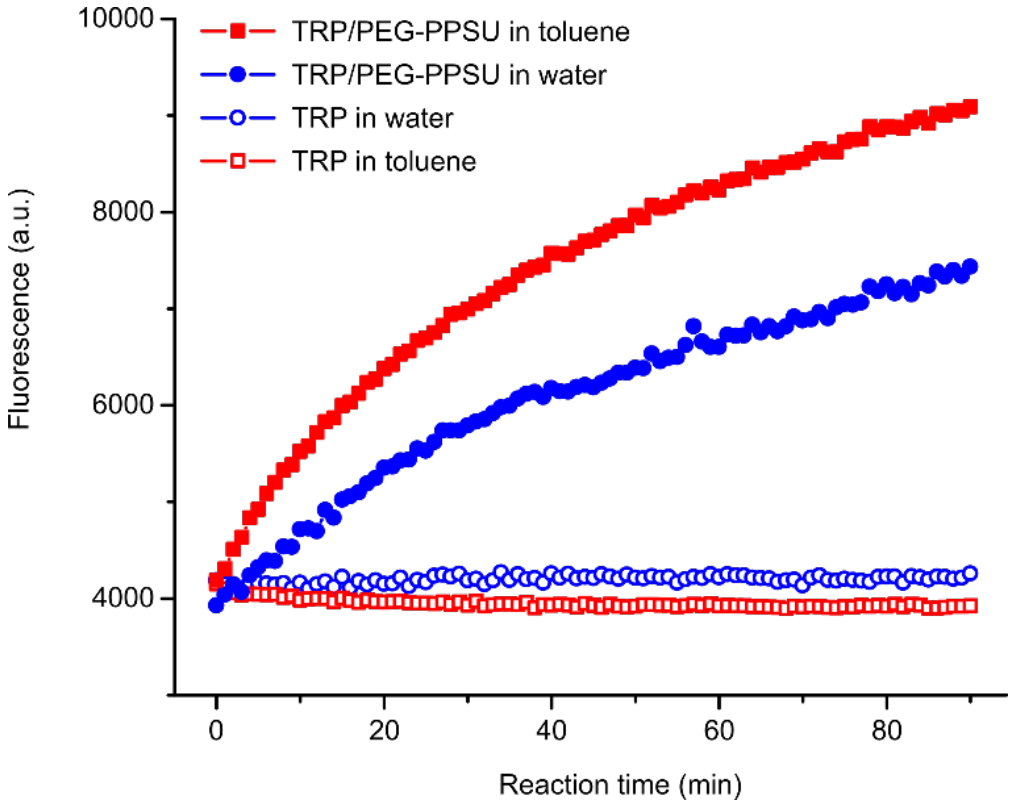

Figure B.40: PEG-PPSU preserves TRP activity at room temperature. The digestion reactions of FITC-BSA were performed in TRP buffer after storing the enzymes in solutions for 24 hours at room temperature.

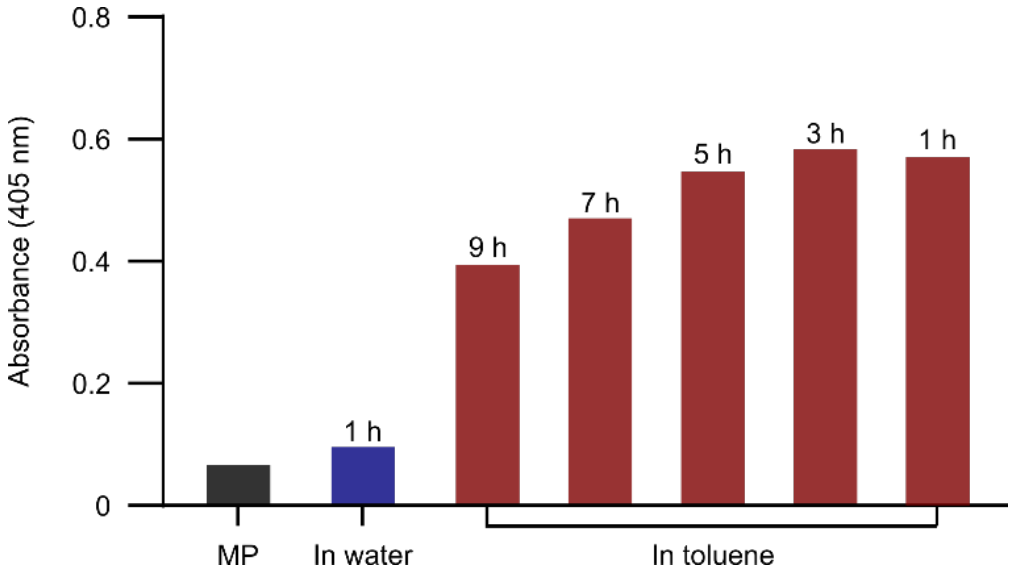

Figure B.41: Enzymatic activity of OPH/PEG-PPSU as a function of storage hours at 80 °C in toluene. Degradation reactions of pesticide MP were carried out in Tris-HCl to assess the activity. OPH/PEG-PPSU has a negligible activity after the 1-hour storage at 80 °C in aqueous solution.

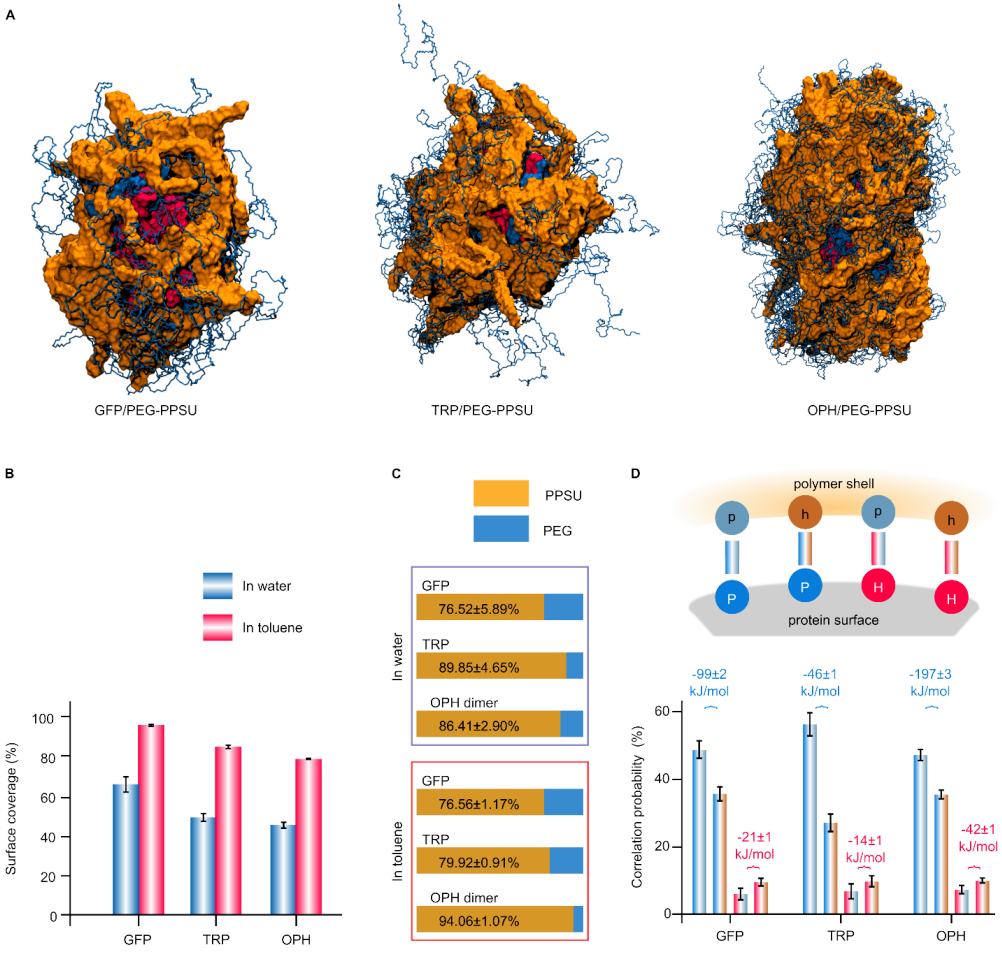

Figure B.42: (A) The explicit solvent all-atom MD simulations performed on the mixture of PEG-PPSU (PEG, blue; PPSU, orange) with proteins (hydrophobic patches, red; hydrophilic patches, blue) in toluene led to the formation of a polymeric framework around each protein. (B) Increased surface coverage was found in toluene than in water for all the three proteins. (C) Component analysis of the polymeric shell around each protein shows that PPSU is adsorbed preferentially than PEG at the protein surfaces. (D) Correlation probability (in percent) between the hydrophilic patch (P, blue)-hydrophobic patch (H, red) at protein surface and the hydrophilic sulfone (p, light blue)-hydrophobic propylene (h, orange) on PPSU nearest neighbors in toluene. Energy analysis of the hydrophobic interactions (red) and hydrophilic interactions (blue) between protein and polymer shows that the adsorption in toluene is dominated by the hydrophilic interactions. The uncertainties refer to the standard deviations.

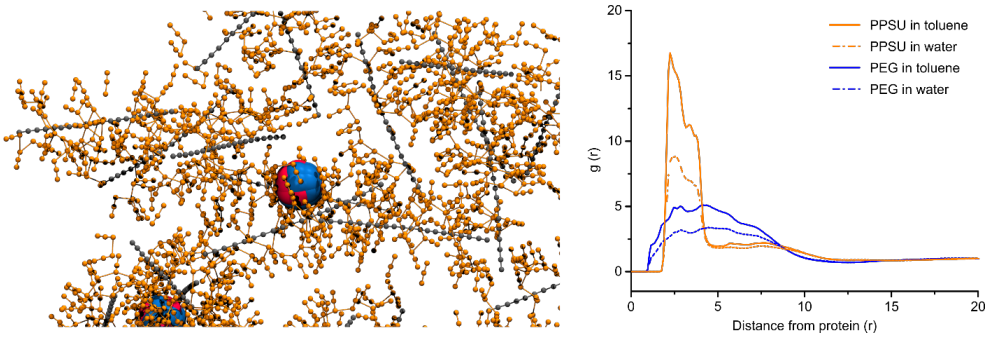

Figure B.43: CG models used in the MD simulations. The hydrophilic surfaces and hydrophobics surface are colored in blue and red, respectively. The protein anchors (propylene sulfone) on nanofibrils are colored in orange. Radial density profiles of PEG and PPSU around the center of mass of the model protein shows an enhanced confinement effect in toluene than in water.

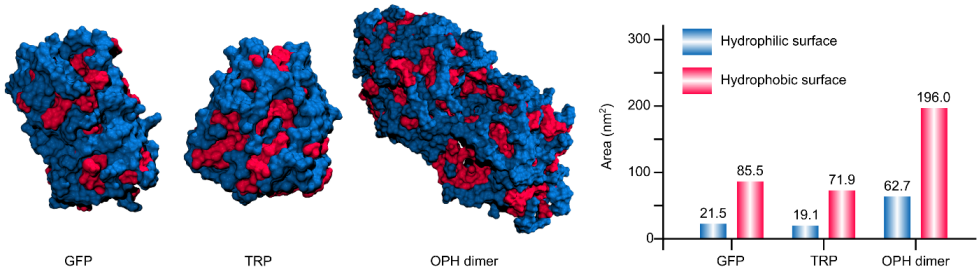

Figure B.44: Surface analysis of the three folded water-soluble proteins based on hydrophilicity/hydrophobicity (blue/red) shows characteristic patch size distributions. The surfaces of water-soluble proteins are dominated by hydrophilic patches, as demonstrated by calculating the hydrophilic/hydrophobic surface for each protein.

Protein	PDB ID	Number of PEG-PPSU chains	Box Size
GFP	1GFL	30	$16 \times 16 \times 16\text{nm}^3$
TRP	1S0Q	50	$15 \times 18 \times 15\text{nm}^3$
OPH	3F4D	100	$23 \times 17 \times 18\text{nm}^3$

Table B.1: PEG-PPSU/protein complex simulation system configuration

B.3 Hierarchical PPSU Hydrogels for Multi-Component Vaccines

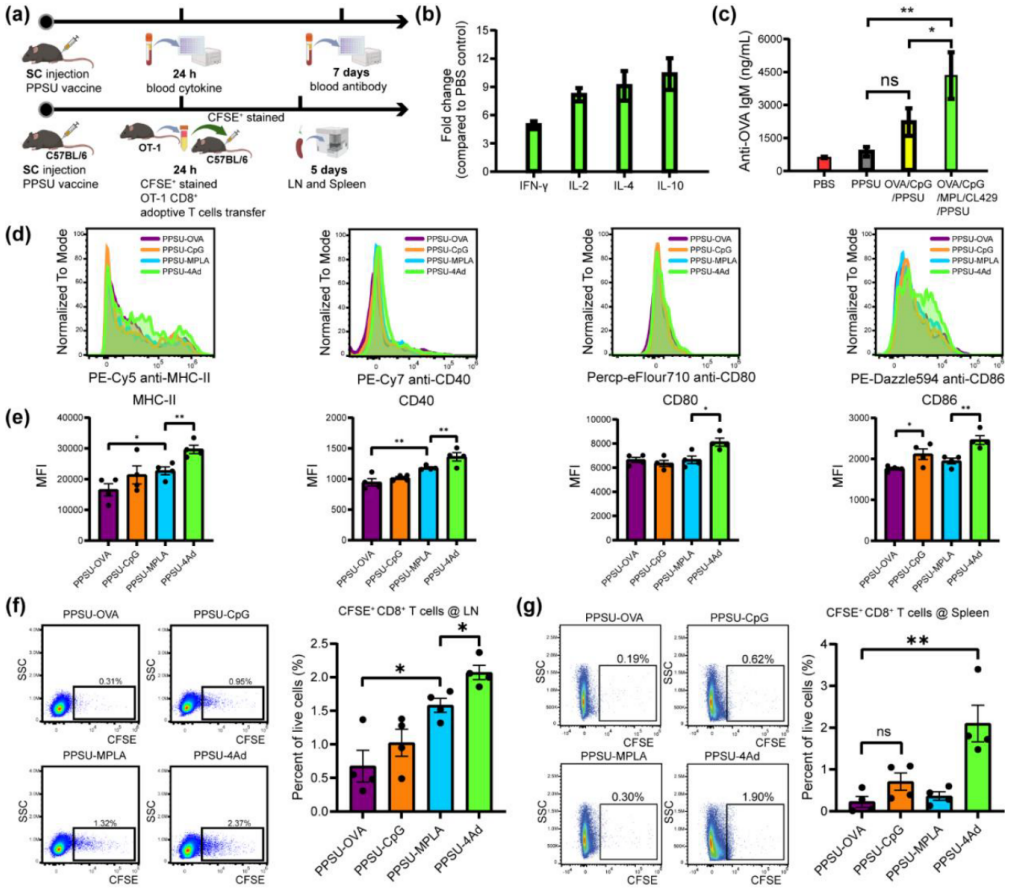

Figure B.45: Validation of multi-adjuvant/antigen-loaded PPSU hydrogels as a subunit vaccine. (a) Schematic schedule of *in vivo* blood analysis and adoptive T cell transfer. (created with BioRender.com). (b) Cytokine fold changes 24 h after subcutaneous injection of the multiantigen/ adjuvant (LPS excluded) loaded PPSU relative to PBS control in mice. $n = 3$ mice per group (mean $\pm$ s.d). (c) Blood anti-OVA IgM antibody levels 7 days post subcutaneous administration of the multi-antigen/adjuvant (LPS excluded) loaded PPSU relative to single adjuvant, blank PPSU and PBS controls. $n = 3$ mice per group (mean $\pm$ s.d). (d) Flow cytometry histogram and (e) mean fluorescence intensity (MFI) of activation markers (MHC-II, CD40, CD80, and CD86) on dendritic cells in the lymph node after 4 days following the adoptive transfer of carboxyfluorescein succinimidyl ester (CFSE) stained $CD8^+$ T cell from OT-1 mice to C57BL/6 mice. $n = 4$ mice per group (mean $\pm$ s.d). (f) Gating strategies and percentage of live $CFSE^+CD8^+$ T cells at lymph node and (g) spleen after 4 days post adoptive T cell transfer. $n = 4$ mice per group (mean $\pm$ s.d). $* : p < 0.05$, $** : p < 0.01$, and ns: not significant by unpaired *t*-test.